



UNIVERSITY OF LIÈGE
FACULTY OF MEDICINE

Aging and Alzheimer's Disease

Multimodal Investigation of Image-derived Biomarkers

Soodeh Moallemian

Aging and Memory Lab, GIGA-CRC In Vivo Imaging
University of Liège
Belgium



Supervisors:
Prof. Christine Bastin
Prof. Christophe Phillips

A thesis submitted in partial fulfilment of the requirements for the degree of Doctor of Philosophy
in Biomedical and Pharmaceutical Sciences

Academic year 2022-2023



UNIVERSITY OF LIÈGE
FACULTY OF MEDICINE

Aging and Alzheimer's Disease

Multimodal Investigation of Image-derived Biomarkers

Soodeh Moallemian

Aging and Memory Lab, GIGA-CRC In Vivo Imaging
University of Liège
Belgium



Supervisors:
Prof. Christine Bastin
Prof. Christophe Phillips

A thesis submitted in partial fulfilment of the requirements for the degree of Doctor of Philosophy
in Biomedical and Pharmaceutical Sciences

Academic year 2022-2023

To all my beloved ones, especially my parents who may never peruse these pages yet played an integral role in guiding me through every chapter of my academic odyssey.

Acknowledgements

As with any piece of research that results in the production of a thesis, the cover should bear not only the name of the researcher but also the names of all those unsung heroes who, to varying degrees, provided assistance, encouragement, and guidance.

First and foremost, I extend my heartfelt appreciation to my supervisors, Dr. Bastin and Dr. Phillips, for their invaluable mentorship and expert guidance. Their insightful feedback, constructive criticism, and dedication to pushing me beyond my limits have been truly transformative. I am grateful for their patience and the time they invested in nurturing my growth as a researcher. Christine, you have been an exceptional mentor, guiding me through every step of these four years and teaching me how to stand on my own. I appreciate all your help and insights, not only in my academic journey but also for listening to my negative thoughts and transforming them into positive ones. Christophe, you have consistently pushed me forward, imparted strength, and illuminated the fact that the right path isn't always the easiest one. I thank you for all the courage you have given me throughout these years.

I also extend my gratitude to my esteemed jury members, Dr. Ferath and Dr. Dupont, for agreeing to challenge me in the evaluation of my work. I appreciate your time and your kind suggestions and comments. I would like to thank my thesis committee members, Dr. Maquet, Dr. Schmit, and Dr. Sacre, for their discussions, questions, and guidance, which greatly aided me in completing my project. I also want to thank Dr. Collette, Dr. Maquet, Dr. Salmon, and Dr. Vandewalle for their moral support and their genuine concerns about the situation in Iran and all Iranians.

My dear friends and colleagues, including Nawel, Ilenia, Zoltan, Renaut, Solene, Larry, Sepehr, Nasrin, Siamak, Marine, Mael, Justinas, Pouyan, Gregory, Mael, Puneet, Siya, Arianna, Annick, Brigit, Benjamin, Maryam, and Ahmadreza, your camaraderie has been a constant source of motivation. Your moral support has always meant a lot to me. I

believe that without friends, living here and facing difficulties would have been overwhelming.

Florence and Islay, you were not just my colleagues but my best friends, whom I could trust and open up to. I appreciate all your support. I will cherish the memories we created during these years in my heart. We evolved alongside each other, and I hope our friendship lasts forever.

Elise and Stella, you taught me how to be brave and strong even in the hardest times. I could not ask for better friends. A big yay to all the amazing BIG office girls!

Nikita, you were never just a colleague to me. Your mentorship provided me with countless valuable experiences. I appreciate the time you spent teaching me, and I even learned to appreciate your unique attitude.

Roya, you are well aware that you are not just my best friend. Our friendship has been exactly what I needed, and I cannot thank you enough for being there for me during both the good and bad times. At some point, I suddenly opened my eyes and realized you had become an integral part of my family.

Mina and Alireza, your moral support, especially over the last two years, has reaffirmed my belief that there are still good people in this world. I feel incredibly fortunate to be a part of your lives, and you are and always will be our best friends. I don't know how to thank you enough for all your kindness.

My deepest appreciation goes to my beloved parents Soosan, and Farzin. You have nurtured me in your loving arms, helped me, and taught me to be the best version of myself. Your unwavering belief in my abilities has been a driving force behind my academic pursuits. I am forever grateful for the values you instilled in me and the sacrifices you made to ensure my success. I am so lucky to have you as my parents.

To my dearest grandmother, Mahin, who has always been an idol to me, teaching me how to pursue my dreams even if they seem hard to reach.

To my lovely sisters, Sara and Rojin, for their unending love and encouragement. Your belief in my abilities has been a driving force behind my academic pursuits. And to my two cherished nephews, Arian, and Ario, you bring boundless joy to my life. Even from a distance, you are the sweet cherry that completes my pie and the radiant sun that pierces through my cloudy skies. Your presence adds an extra layer of happiness to my life that I am truly grateful for.

I must thank my in-laws, Farzaneh, and Karim, for raising Ali into such a great man who has made my life more colorful. Thank you for all your moral support during the last years.

To my dear husband, Ali, your support, patience, and understanding have been my anchor throughout this journey. Your belief in me, even when I doubted myself, has been a constant reminder of the power of a loving partnership. Your sacrifices and encouragement have empowered me to pursue my dreams wholeheartedly. I cannot thank you enough for all the lights you brought to my life, especially during the last 4 years. Ali, you are truly my better half.

Abstract

Aging is an inevitable process in life and the primary risk factor for most neurodegenerative diseases including Alzheimer's disease (AD), the most common form of dementia. As life expectancy continues to increase, AD prevalence is expected to rise. AD-related pathological processes unfold decades before the emergence of clinical signs of cognitive decline and involve brain changes such as atrophy, accumulation of amyloid-beta plaques and tau neurofibrillary tangles (NFT), synaptic and neuronal loss, demyelination, and iron accumulation that would eventually lead to cognitive impairment.

Here, to assess brain myelin and iron content *in vivo*, quantitative MRI (qMRI) maps like magnetization transfer saturation (MTsat), Effective transverse relaxation rate ($R2^*$), and proton density (PD) were used. And synaptic density was measured using the total volume distribution map (V_t) of [F^{18}] UCB-H PET images.

In this thesis, we examined the simultaneous occurrence of these brain changes in aging and AD, identifying significant differences in the hippocampus and amygdala. Demyelination emerged as a key distinguishing factor between AD and healthy groups. The effects of age on various brain characteristics were re-evaluated in a multivariate model, with proton density being the most age-related factor in healthy aging.

Finally, we attempted to examine the association of cognitive performance and the rate of cognitive decline with qMRI maps and GM and WM volume. The univariate regression analyses at baseline revealed correlations between different cognitive scores and brain tissue properties within the cerebellum, hippocampus, middle temporal, and medial orbitofrontal cortex. Moreover, the multivariate analysis shows that cognitive performance was related to combined tissue properties in the middle frontal gyrus, insula, and cerebellum. There were only a few

results for the rate of cognitive decline, with univariate correlations within the left fusiform between longitudinal relaxation rate (R1) maps in GM and attention and memory decline.

To conclude, our findings shed light on the complex relationships between changes in aging and AD brains. Furthermore, we emphasize the importance of multivariate analysis for detecting subtle microstructural changes associated with aging that may motivate interventions to mitigate cognitive decline in older adults.

Table of Contents

Acknowledgements	I
Abstract	V
Table of Contents	VII
List of Figures	XI
List of Tables	XIII
Glossary	XV
Abbreviations	XVII
Scientific Contribution	XIX
1 Introduction	21
1.1 Aging and Alzheimer’s Disease	23
1.2 AD Individual Risk Factors.....	25
1.3 AD Biomarkers.....	25
1.3.1 Amyloid-beta and Tau	26
1.3.2 Synaptic Density	27
1.3.3 Brain Atrophy.....	28
1.3.4 Myelin and Iron Contents	29
1.3.5 Cognitive functioning.....	31
1.4 Biomarkers’ Interaction in AD	32
1.5 Objectives and Thesis Outline	38
2 Statistical methodology	41
2.1 General Linear Model (GLM)	43
2.2 Multivariate General Linear Model (mGLM)	44
2.3 Statistical Testing in mGLM	44
2.4 Canonical Component Analysis (CCA).....	45
3 Study I	47
Preface	49

3.1	Introduction	51
3.2	Methods.....	54
3.2.1	Participants.....	54
3.2.2	Data Acquisition.....	55
3.2.3	Image data Processing	57
3.2.4	Statistical Analyses	59
3.3	Results.....	62
3.3.1	Univariate Analyses	62
3.3.2	Magnetization Transfer Saturation (MTsat)	62
3.3.3	Effective Transverse Relaxation Rate (R2*)	62
3.3.4	Voxel-based Morphometry.....	62
3.3.5	Total [F^{18}]UCB-H Volume Distribution	63
3.3.6	Correlation Analyses	63
3.4	Multivariate Analysis	63
3.4.1	Canonical vectors.....	67
3.5	Discussion	70
3.5.1	Myelination.....	70
3.5.2	Iron level	71
3.5.3	GM volume	72
3.5.4	Synaptic density.....	72
3.5.5	Simultaneous brain alterations.....	74
3.5.6	Limitations and conclusion	74
4	Study II	79
	Preface	81
4.1	Introduction	82
4.2	Method	83
4.2.1	Participants and data preprocessing	83

4.2.2	Univariate GLM analyses	84
4.2.3	Multivariate GLM (mGLM).....	84
4.3	Results.....	90
4.3.1	uGLM vs mGLM: Voxel level analyses	91
4.3.2	ROI analyses.....	95
4.4	Discussion	96
4.4.1	Limitations and conclusion	101
5	Study III	103
	Preface.....	105
5.1	Introduction.....	106
5.2	Methods.....	109
5.2.1	Participants.....	109
5.2.2	Imaging Data.....	110
5.2.3	Quantitative MRI	110
5.2.4	Cognitive Assessments	112
5.2.5	Statistical Analysis.....	114
5.3	Results.....	115
5.3.1	Baseline scores	115
5.3.2	Cognitive decline at 2-year follow-up.....	121
5.4	Discussion	123
6	Discussion and conclusion	131
6.1	General Discussion.....	133
6.2	Limitations and future perspectives	138
6.3	Conclusion	140
7	Appendices	143
7.1	Appendix-A: Statistical modeling.....	145
7.2	Appendix-B: Supplementary results - Chapter 2	150

7.3	Appendix-C: Supplementary results - Chapter 3	157
7.4	Appendix-D: UCB-H PET Automated Pipeline Validation ..	160
	References.....	161

List of Figures

Figure 1-1. Correlation between [F^{18}]UCB-H distribution volumes and awareness of memory functioning.....	28
Figure 1-2. Example quantitative maps from a healthy participant (male, 76 years old), derived from MPM qMRI protocol	31
Figure 1-3. Revised model of dynamic biomarkers of the AD pathological cascade	36
Figure 3-1. Example maps from two participants	59
Figure 3-2. Statistical parametric maps of the univariate analysis for the difference between AD and HC groups	64
Figure 3-3. Statistical parametric map of the multivariate analysis for the difference between AD and HC groups	67
Figure 3-4. Raw voxel distribution of Z-transformed maps within each mGLM significant cluster	73
Figure 4-1. Statistical parametric maps of uGLMs in GM.....	87
Figure 4-2. Statistical parametric maps of uGLMs in WM.....	88
Figure 4-3. Statistical parametric maps of mGLMs in GM and WM.....	89
Figure 4-4. The union of all uGLM statistical parametric masks in GM ..	90
Figure 4-5. mGLM vs multiple uGLMs in GM	91
Figure 4-6. Canonical vectors for different modalities from the mGLM model.....	94
Figure 4-7. Median voxel values in Putamen	95
Figure 4-8. Median voxel values in Hippocampus.....	97
Figure 5-1. Statistical parametric maps (SPM) for the regression analysis	117
Figure 5-2. Statistical parametric maps for univariate analysis, using memory as the covariate of interest.	118
Figure 5-3. Statistical parametric maps for the univariate regression analyses, using PACC5 as the covariate of interest	120
Figure 5-4. Statistical parametric maps (SPM) for the multivariate regression analyses within gray and white matter	121
Figure 5-5. Canonical values for the peak voxels within the significant clusters in the GM	123
Figure 5-6. Peak voxel canonical vector within the WM for memory...	124

Figure 7-1. Statistical parametric maps for the uGLMs at a corrected threshold of $p < .05$ FWER in the GM.....	157
Figure 7-2. Statistical parametric maps for the uGLMs at a corrected threshold of $p < .05$ FWER in the WM.....	158

List of Tables

Table 3-1. Demographics, clinical characteristics, and neuropsychological scores of AD and HC groups	55
Table 3-2. Significant differences between AD participants and healthy controls for MTsat and Vt maps	65
Table 3-3. Pearson’s correlations between different maps in AD group	66
Table 3-4. Significant differences between AD and HC groups in the mGLM model	68
Table 3-5. ROI based voxel-level group comparison in MTsat, R2*, GM volume, Vt maps	69
Table 4-1. Summary statistics for significant voxels in uGLMs and mGLM	92
Table 4-2. Summary statistics for significant voxels in uGLMs and mGLM	93
Table 4-3. Pearson Partial Correlations with age	98
Table 5-1. Demographics of the participants	110
Table 5-2. Univariate regression results at the baseline	116
Table 5-3. Multivariate regression results at the baseline	122
Table 7-1. Pearson’s correlations between different maps in AD group with age and gender	150
Table 7-2. Pearson’s correlations between different maps in the HC group with age and gender	152
Table 7-3. Pearson’s correlations between different maps in HC group	154
Table 7-4. Fisher z-transformation test for correlation coefficients between the HC and AD group	155
Table 7-5. Canonical vector sizes for different modalities from the mGLM model	159

Glossary

Term	Definition
Dementia	Dementia is an umbrella term, describing the progressive deterioration of cognitive abilities, such as memory, thinking, and reasoning, that significantly impairs an individual's daily functioning and quality of life (Duong et al., 2017)
longitudinal relaxation time (T1)	T1 refers to the time it takes for the longitudinal magnetization of a tissue to return to about 63% of its equilibrium state after being perturbed by an external radiofrequency (RF) pulse.
Transverse relaxation time(T2)	T2 reflects the length of time it takes for the transverse magnetization to decrease by about 37%
T2*	The T2 constant is only theoretical; in practice, the physical decay is more rapid, and affected by local perturbations present in the static field B ₀ . The actual transverse relaxation time is noted T2* and satisfies the condition T2* < T2.
Effective transverse relaxation rate (R2*)	R2* corresponds to the inverse effective transverse relaxation time ($1/T2^*$). R2* is an indicator of iron content in the brain (Cercignani et al., 2021; Lorio et al., 2014). T2* is measured in seconds (in the ms range), and thus R2* is measured in Hertz.
Longitudinal relaxation rate (R1)	R1 corresponds to the inverse longitudinal relaxation time ($1/T1$). T1 is measured in seconds (in the ms range), and thus R1 is measured in Hertz. T1 and therefore R1 is affected by multiple properties in the brain tissue such as myelin, iron, and water content (Gelman et al., 2001; Lutti et al., 2014).
Magnetization Transfer Saturation (MTsat)	MTsat is minimally affected by T1 relaxation and less sensitive to B1 inhomogeneities (Lema et al., 2017). It is obtained with a linear transformation of the inverse MT FLASH signal, combining PDw and T1w acquisitions, and represents the percentage saturation ensued from one off-resonance pulse during the repetition time. Considering the fact that

MTsat reflects mainly the macromolecular content of tissue it is widely accepted that myelin has a large contribution to measured MTsat in brain (Bjarnason et al., 2005; Henkelman et al., 2001; Stanisz et al., 1999). MTsat is usually reported in percent units (p.u.).

Proton density (PD) PD is the most basic MRI measure, representing the apparent concentration of water protons (mobile hydrogen atoms) in each voxel (Cercignani et al., 2021). Effective proton density (PD) are estimated from the signal amplitude maps by adjusting for global and local receive sensitivity differences (Weiskopf et al., 2013). PD is usually reported in percent units (p.u.).

Metal homeostasis It refers to the ability of individual cells to maintain a healthy level of metal within the cell.

Free radicals It can be defined as any molecular species capable of independent existence that contains an unpaired electron in as atomic orbital.

Orientation dispersion index (ODI) On the other hand, the ODI reflects the discrete feature of neurites by assessing their orientation coherence, such as the complexity of dendritic structures in the gray matter and the distribution of fiber orientations in the white matter (Zhang et al., 2012).

Neurite density index (NDI) The NDI is used to assess the volume fraction within the neurite range, measuring the packing density of axons or dendrites. A significant decrease in NDI indicates a decrease in neurite density and reflects underlying neurite loss (Zhong et al., 2023).

Abbreviations

AD	Alzheimer's disease
ANOVA	Analysis of variance
BPS	Behavioral Pattern Separation
DSST	Digit-Symbol Substitution test (DSST)
FCSRT	Free and Cued Selective Reminding Test (FCSRT)
fMRI	Functional MRI
FWE	Family-wise Error
FWER	Family-wise Error Rate
GM	Gray matter
GLM	General Linear Model
MANOVA	Multivariate analysis of variance
MRI	Magnetic resonance imaging
MMSE	Mini-Mental State Examination
mGLM	Multivariate GLM
mSPM	Multivariate SPM
MSPM	Multivariate General Linear Model Toolbox in SPM
MT	Magnetization transfer
MTsat	Magnetization transfer saturation
NFT	Neurofibrillary tangle
PACC5	Pre Clinical Alzheimer Cognitive Composite
PD	Effective Proton density
PET	Positron emission tomography
qMRI	Quantitative magnetic resonance imaging
R1	longitudinal relaxation rate
R2*	Effective transverse relaxation rate
ROI	Region of interest
SPM	Statistical Parametric Map
SV2	Synaptic vesicle glycoprotein
SV2-A	Synaptic vesicle glycoprotein isoform 2A
T1	longitudinal relaxation time
T2	transverse relaxation time
VBM	Voxel-based morphometry
VBQ	Voxel-based quantification
WM	White matter

Scientific Contribution

Conference Presentations

2022

1. **Moallemian, S.**, Salmon, E., Bahri, MA., Belyi, N., Delhaye, E., Balteau, E., Degueldre, C., Phillips, C., & Bastin, C., **“Multimodal imaging of microstructural cerebral changes and loss of synaptic density in Alzheimer’s disease.”** 2022. Brain and Brain PET. Glasgow. Scotland.
2. **Moallemian, S.**, Salmon, E., Bahri, MA., Belyi, N., Delhaye, E., Balteau, E., Degueldre, C., Phillips, C., & Bastin, C., **“Investigating demyelination, iron accumulation, and synaptic loss in Alzheimer’s disease using multimodal imaging techniques.”** 2022. Quantitative MRI. Montreal. Canada.
3. **Moallemian, S.**, Salmon, E., Bahri, MA., Belyi, N., Delhaye, E., Balteau, E., Degueldre, C., Phillips, C., & Bastin, C., **“Multimodal imaging of microstructural cerebral changes and loss of synaptic density in Alzheimer’s disease.”** 2022. GIGA-day. Liege. Belgium.

2023

1. **Moallemian, S.**, Callaghan, M. F., Bastin, C., Phillips, C., **“Multivariate SPM analysis of quantitative MRIs:Widespread age-related differences revisited.”** 2023. OHBM. Montreal. Canada.
2. **Moallemian, S.**, Callaghan, M. F., Bastin, C., Phillips, C., **“Multivariate SPM analysis of quantitative MRIs:Widespread age-related differences revisited.”** 2023. GIGA-day. Liege. Belgium.
3. **Moallemian, S.**, Dauby, S., Meyer, F., Bastin, C., Phillips, C., Salmon, E., Maquet, P., Bonhomme, V., Dammicco, S., Degueldre, C., Laleux, S., Belyi, N., Bahri, MA., **“PET Pro: An Automated pipeline to estimate the image-derived input function for UCB-H PET”.** 2023. INCF. Virtual.
4. **Moallemian, S.**, Chylinski, D., Van Egroo, M., Narbutas, J., Salmon, E., Maquet, P., Collette, F., Vandewalle, G., Phillips, C., Bastin, C.* **Moallemian, S., Chylinski, D., Van Egroo, M., Narbutas, J., Salmon, E., Maquet, P., Collette, F., Vandewalle, G., Phillips, C., Bastin, C., “Relationships between Cognition and Brain Tissue Properties: A Longitudinal Study on Healthy Older Adults.”** 2023. Quantitative MRI. Montreal. Canada.


Publications

1. **Moallemian, S.**, Salmon, E., Bahri, M.A., Belyi, N., Delhaye, E., Balteau, E., Degueldre, C., Phillips, C., Bastin, C., 2023. **Multimodal imaging of microstructural cerebral alterations and loss of synaptic density in Alzheimer’s disease.** *Neurobiology of Aging* 132, 24–35. <https://doi.org/10.1016/j.neurobiolaging.2023.08.001>.
2. **Moallemian, S.**, Bastin, C., Callaghan, M. F., Phillips, C., **“Multivariate Age-related analysis of variance in quantitative MRI maps: Widespread age-**

related differences revisited". medRxiv 2023.10.19.23297253.

<https://doi.org/10.1101/2023.10.19.23297253>

- 3. Moallemian, S., Collette, F., Vandewalle, G., Salmon, E., Maquet, P., Phillips, C., Bastin, C., "Relationships between cognition and Brain structure Tissue Properties: A Longitudinal Study on Healthy Older Adults."** Under preparation.

Chapter **1** 

Introduction

1.1 Aging and Alzheimer's Disease

The effect of aging on the brain and cognition are widespread and have multiple etiologies which impact both working capacity and quality of life (Reitz and Mayeux, 2014). There is, however, large interindividual variability in the decline of cognitive function, ranging from (almost) no changes to the pathological deterioration found in dementia, e.g. Alzheimer's disease (AD) (Christensen et al., 1999). Alzheimer's disease affects around 10% of people aged 65 and above (Azam et al., 2021; Hou et al., 2019). Similarly, brain alterations vary considerably from one individual to another.

Autopsy studies confirm the presence of Amyloid plaques, neurofibrillary tangles, Lewy bodies, inclusions of TAR DNA-binding protein 43 (TDP-43), synaptic dystrophy, the loss of neurons and the loss of brain volume in most of the brains of aged people who had not been diagnosed with a neurological disease (Elobeid et al., 2016; Wyss-Coray, 2016). Therefore, brain aging might be a measure to scale the progression of neurodegeneration (Wyss-Coray, 2016). Although age is characterized as a primary risk factor for most neurodegenerative diseases, the exact mechanisms through which aging is associated with neurodegeneration are yet to be identified (Azam et al., 2021; Callaghan et al., 2014).

Among the neurodegenerative diseases, AD which leads to cognitive impairments (Dean et al., 2017; Gonneaud and Chételat, 2018; Tan et al., 2014) is the most prevalent form of dementia accounting for approximately 60-80% of cases (Wimo et al., 2015). Age is the first risk factor for AD, followed by family history, the second strongest risk factor for Alzheimer disease (AD). Today, AD is characterized by the accumulation of amyloid plaques and neurofibrillary tangles in the brain, leading to the progressive loss of neurons and cognitive decline (Braak and Braak, 1991; Jack et al., 2018). It is recognized that AD pathological processes unfold decades before the emergence of clinical signs of cognitive decline (Dean et al., 2017; Gonneaud and Chételat, 2018; Tan et al., 2014).

Despite the prevalence of AD, the search for an effective drug or cure for the disease continues as none of the current drugs have the desired effect (Tatulian, 2022). Consequently, the most promising approach is to study this disease in its earliest stages to assess different risk factors (Perl, 2010) and promote prevention.

BOX-1. Clinical stages of AD

The clinical classification of AD is mainly based on the severity of cognitive decline and histopathological alterations (Perl, 2010). Four stages are usually described (McKhann et al., 2011):

Mild cognitive impairment (MCI) due to AD: This phase marks the initial pathological changes affecting the entorhinal cortex and later the hippocampus. Individuals in this stage experience slight memory loss, particularly for recent memories, while their daily functioning remains relatively unaffected.

Mild Alzheimer's Disease: This phase marks the onset of cognitive symptoms with functional impact, as pathological changes extend to the cerebral cortex. Symptoms include difficulty recalling new information, forgetting appointments, reduced problem-solving abilities, impaired judgment, and executive function. Personality changes, mood swings, and diminished spontaneity are observed, along with states of confusion and disorientation.

Moderate Alzheimer's Disease: During this phase, symptom severity escalates as pathological damage extends to regions governing language, reasoning, and sensory processing in the cerebral cortex. In addition to heightened symptoms from earlier phases, behavioral issues and social withdrawal emerge. These are succeeded by language disorders and compromised visuo-spatial skills. Notably, individuals in this stage struggle with recognizing their loved ones.

Severe Alzheimer's Disease: In this phase, individuals lose their ability to perform daily activities independently. Pathological damage is thought to encompass all areas of the cortex. Cognitive abilities decline to their lowest point, accompanied by the emergence of systemic symptoms. These include challenges in executing learned motor tasks (dyspraxia), impaired sense of smell (olfactory dysfunction), disrupted sleep patterns, extrapyramidal motor signs like dystonia, akathisia, and symptoms akin to Parkinson's disease.

Note that another integral staging system is that of (Braak and Braak, 1991) which divides AD progression into 6 stages based on the topographical staging of NFTs.

1.2 AD Individual Risk Factors

Genetic mutations have been shown to cause familial AD, which account for less than 5% of AD (Tanzi, 2012). On the other hand, several common gene polymorphisms have been associated with the sporadic form of AD and are currently intensively studied (Bettens et al., 2013). The strongest genetic risk factor for sporadic AD is the polymorphism of Apolipoprotein E (ApoE). Among the 3 polymorphic alleles (e2, e3 and e4), e4 is associated with an increased risk of developing AD whereas e2 is linked to a decreased AD risk, relative to e3 homozygous individuals (Liu et al., 2013). However, not all ApoE e4 carriers develop AD and they are thus referred to being asymptomatic individuals at risk of AD (Dubois et al., 2014).

More generally, non-genetic risk factors of AD have been identified: Cerebrovascular disease, hypertension, type 2 diabetes, increased body weight, dyslipidemia, metabolic syndrome, smoking, traumatic brain injury (Reitz and Mayeux, 2014). Many of these factors are gathered on the term “Allostatic load”, i.e. a strain put on a physiological system.

1.3 AD Biomarkers

A biomarker is an impartial quantification of a biological or pathological process that can be used to evaluate disease risk or prognosis, guide clinical diagnosis, or monitor therapeutic interventions. In AD, the pathological processes include a progressive accumulation of amyloid plaques and tau neurofibrillary tangles (NFT), in addition to synaptic and neuronal loss (Gulisano et al., 2018; Jack et al., 2013; Spillantini and Goedert, 2013; Tan et al., 2014; Xiaomin et al., 2021).

1.3.1 Amyloid-beta and Tau

Amyloid-beta peptide spontaneous oligomerization is detrimental to synaptic function and its detection in the brain is associated with dementia (Mc Donald et al., 2010). Amyloid-beta deposition is believed to result from an imbalance between its production and clearance (Mawuenyega et al., 2010; Weller et al., 2009).

BOX-2. Amyloid-beta aggregation and Tau accumulation

The engagement of amyloid-beta in the pathological expression of AD has been known for over a century (Bilgel et al., 2018; Sprinz et al., 2018). This involves the aggregation of fibrillar amyloid-beta (A β) causing the creation of A β plaques in the brain (Braak et al., 1999; Goedert et al., 1989). The current hypothesis is that plaque accumulation induces multiple downstream alterations that lead to neurodegeneration and cognitive decline (Young et al., 2020). Our understanding of the downstream alterations has changed over the years and now includes not only inflammation but synaptic alterations, functional changes and alterations in tau protein (Goedert et al., 1989; Krause and Müller, 2010).

In AD, tau protein deposition seems to follow the staging pattern revealed by Braak and Braak, suggesting tau spreads from the entorhinal cortex (Braak I/II) to the inferolateral temporal and medial parietal lobes (Braak III/IV) and finally the neocortex (Braak V/VI) (Braak and Braak, 1991; Schöll et al., 2016).

Tau NFT seems to collocate much more with synaptic and neuronal loss than amyloid neurotic plaques. Likewise, once AD cognitive symptoms are detected, tau NFT burden follows more closely cognitive decline than amyloid plaques (Musiek and Holtzman, 2015). However, amyloid plaques might be required for tau NFT to expand from subcortical to cortical areas (Jeremic et al., 2021).

Tau is a protein essential to stabilize microtubules (Pîrșcoveanu et al., 2017). During the course of AD, hyperphosphorylated tau detaches from the microtubules, and accumulated in the somatodendritic compartment which is toxic for neurons (Xiaomin et al., 2021).

Thanks to brain positron emission tomography (PET), assessment of amyloid-beta and tau protein aggregation is not limited to histological studies. In PET, a radio ligand is injected with binding potential to a specific compound; for instance, [F^{18}]flutemetamol, [F^{18}]florbetapir, and [F^{18}]florbetaben, are three tracers with binding to Amyloid plaques (Chiao et al., 2019; Jack et al., 2017).

Amyloid-beta deposits topography follows an irreversible and hierarchical trajectory from the basal brain to the outer cortex, while deposits of neurofibrillary tangles spread in the brain in an irreversible hierarchical fashion (Braak and Braak, 1991). Deposits of neurofibrillary tangles correlate more closely with cognitive decline and neuronal loss than Amyloid-beta deposits (Adam et al., 2007). However, synaptic damage and loss are earlier events than amyloid plaques and NFTs in AD progress and show the largest correlation with cognitive deficits in AD patients (Xiaomin et al., 2021).

1.3.2 Synaptic Density

Synapses play a vital role in cognitive function, and the loss of synapses is a significant and consistent pathology in AD (Scheff et al., 2014; Selkoe, 2002). The decline in cognitive abilities in AD is strongly linked to the reduction of synapses in the association cortex and limbic system (Scheff et al., 2014). In the initial clinical stages of AD, patients with mild cognitive impairment (MCI) display a decrease in synapses and synaptic proteins (Scheff et al., 2014).

Synaptic vesicle glycoprotein 2 (SV2) is an essential vesicle membrane protein; one of its isoforms, SV2-A, is ubiquitously expressed in virtually all synapses (Bajjalieh et al., 1994; Chen et al., 2018). Hence, SV2-A protein is a highly useful indicator of synaptic density in AD and other neuropsychiatric disorders. Several high-affinity SV2-A ligands that penetrate the brain rapidly such as UCB-A, UCB-H, and UCB-J (Bretin et al., 2013; Estrada et al., 2016; Mercier et al., 2017, 2014; Warnock et al., 2014) are available that can bind to SV2-A proteins in-vivo in dynamic PET acquisitions.

Synaptic loss as assessed by total volume distribution of UCB-H reveals a significant reduction in the right anterior hippocampus in AD patients compared to healthy controls (Bastin et al., 2020). **Figure 1-1** shows the results from correlation analyses of UCB-H quantification using Logan Graphic analyses and awareness of memory functioning. Moreover, a decrease in the uptake of UCB-J in AD patients is reported in the medial temporal regions (M.-K. Chen et al., 2021).

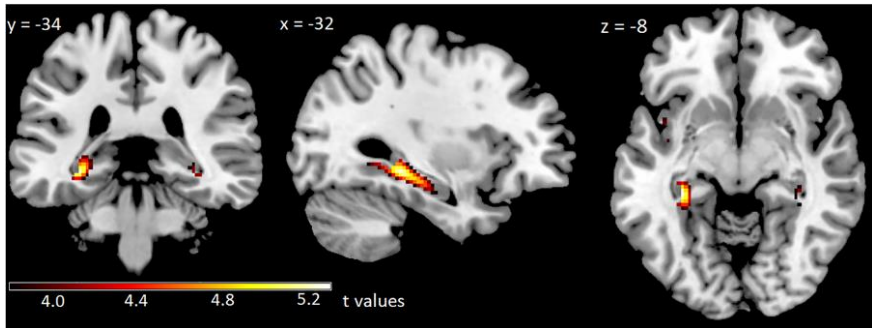


Figure 1-1. Correlation between $[F^{18}]UCB-H$ distribution volumes and awareness of memory functioning. The hippocampus shows smaller synaptic density that correlates with poorer awareness of memory functioning in AD patients at $p < 0.05$ after correction for family wise error rate (Bastin et al., 2020).

1.3.3 Brain Atrophy

Another core biomarker for AD is brain atrophy (Bobinski et al., 1999), which is caused by neuronal loss and synapse degeneration (Tzioras et al., 2023). In the case of AD, most of atrophy studies focus on hippocampal formation, known to be the first affected region (McKhann et al., 2011). Hippocampal atrophy is used to track disease progression in clinical trials (McKhann et al., 2011). It has been validated that in about 40% of cognitively normal older individuals, neurodegeneration (hippocampal atrophy) precedes positive amyloid imaging (Jeremic et al., 2021; Villemagne et al., 2011). Atrophy in the hippocampus and entorhinal cortex is associated with a decline in memory function, progression of memory impairment (Mungas et al., 2005) and an increased risk of converting from MCI to AD. Today, increased rates of brain atrophy on longitudinal MRI are frequently used as a biomarker of

disease progression in AD and other dementias (O'Brien et al., 2020; Pini et al., 2016).

1.3.4 Myelin and Iron Contents

In the quest for early biomarkers, it has been suggested that changes in brain microstructure are among the first manifestations of AD (Bartzokis, 2011).

Metal ions have a significant role in the brain, since they are required to regulate the neuronal activity in the synapses and many other biological functions (Llanos-González et al., 2020). There is increasing evidence suggesting that metal balance impairments, either excess or deficiency of metal ions (e.g. zinc, iron, and copper), are involved in a series of processes that can result in neurodegeneration and cell death (Dhakal and Macreadie, 2020). When metal elements' homeostasis is disrupted, several protein misfolding events may appear inside the cell (Cristóvão et al., 2016). Increased metal ions (specifically for zinc, iron, and copper) levels are detected in amyloid-beta aggregates (Calabrò et al., 2021). Moreover, an increase in free iron is toxic, inducing oxidative stress and inflammation, cell dysfunction, and, ultimately, cell death (Bartzokis, 2011; Bulk et al., 2018; Calabrò et al., 2021). Oligodendrocytes have the highest iron content of all brain cell types (Erb et al., 1996) and as much as 70% of brain iron is associated with myelin (de los Monteros et al., 2000).

The myelin sheaths in the central nervous system are produced by oligodendrocytes. The effect of age on myelin is complex, because even though some myelin sheaths are degenerating, myelination of axons from the prefrontal and other association areas (temporal and parietal lobes) continues until the end of the fifth decade (Bartzokis, 2004a; Corrigan et al., 2021; Peters, 2002). The age-related loss/dysfunction of myelin would result in a further increase in the production of damaging free radicals. An increase in neuronal free radical production has also been postulated to contribute to AD NFT-related neuropathology (Gamblin et al., 2000).

BOX-3. Quantitative MRI (qMRI)

Conventional MRI is based on the acquisition of contrast images. These images are affected by many different contrast mechanisms, such as the MR pulse sequence, the MR scanner settings, B₀- and B₁-field inhomogeneities, as well as the different tissue properties. The MR scanner settings are chosen to highlight or saturate tissue properties, resulting in e.g., T₁-weighted, or T₂-weighted images.

Conversely, **quantitative MRI (qMRI)** is aimed at the direct measurement of physical tissue properties, such as the T₁-, T₂-, and T₂*-relaxation times or the proton density (PD), largely eliminating hardware effects (Gracien et al., 2020). These properties are, in theory, independent of acquisition method and system imperfections.

A comprehensive quantitative **multi-parametric mapping (MPM)** approach was devised to obtain quantitative images (Helms et al., 2010, 2009; Weiskopf et al., 2011). In this sequence, three series of multi-echo images, weighted towards magnetization transfer (MT), T₁, and proton density (PD) are collected. These images can be used to provide high-resolution maps of the **magnetization transfer saturation (MTsat)** that is proportional to myelin content in the brain, **effective proton density (PD*)**, **longitudinal relaxation rate** ($R_1 = 1/T_1$), and **effective transverse relaxation rate** ($R_2^* = 1/T_2^*$), proportional to the iron level in the brain (Weiskopf et al., 2015, 2014, 2013).

It is hypothesized that myelin breakdown and increases in iron levels are very early events in the pathophysiology of Alzheimer's disease. In support of this "myelin and iron" hypothesis, histological studies showed that myelin breakdown in early AD occurs mainly in frontal and temporoparietal areas (Bartzokis, 2011; Bulk et al., 2018; Kalpouzos et al., 2017; Zecca et al., 2004). Increased iron content was also found in frontal and temporal areas of AD patients (Bulk et al., 2018; House et al., 2008). Moreover ex vivo studies showed that altered iron accumulation is positively correlated with the number of amyloid-beta plaques in these areas (Bulk et al., 2018; Van Duijn et al., 2017). Elevated iron content has also been observed in the hippocampus of AD patients (Zeineh et al., 2015). Additionally, higher levels of ferritin (i.e., the principal iron storage protein of the body) in the cerebrospinal fluid

(CSF) are associated with the poorer cognitive performance of cognitively normal, MCI and AD participants, and predicted MCI conversion to AD (Ayton et al., 2015; Peng et al., 2021).

Thanks to the developments in brain neuroimaging techniques, we can investigate brain micro- and macro-structure characteristics *in vivo* using quantitative MRI (qMRI) techniques (see BOX-3), that provide (semi-)quantitative measures proportional to myelin, iron, and proton density in the brain. Example quantitative maps are illustrated in **Figure 1-2**.

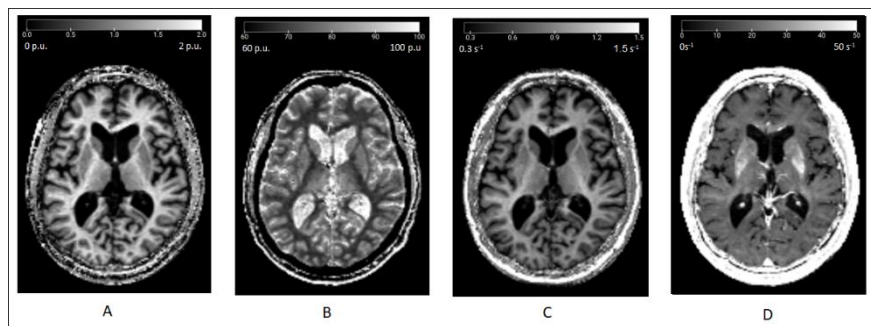


Figure 1-2. Example quantitative maps from a healthy participant (male, 76 years old), derived from MPM qMRI protocol. (A) Magnetization transfer saturation (MTsat); (B) Proton density (PD); (C) longitudinal relaxation rate (R1); and (D) effective transverse rate (R2*).

1.3.5 Cognitive functioning

Alterations in macro- and micro-structure of the brain go along with cognitive changes. Although cognitive impairment is not a hallmark of AD, it is categorized as a typical feature for AD (Sperling et al., 2011a) and the clinical classification of AD is mainly based on the severity of cognitive decline and histopathological alterations (Perl, 2010). Neuropathological alterations in the cerebral cortex and limbic system would lead to deficits in memory, language, and visuospatial skills (Corey-Bloom, 2002).

The most significant cognitive changes observed in the process of normal aging encompass a decline in performance on cognitive tasks

requiring rapid information processing or transformation, crucial for decision-making. Such tasks include measures of processing speed, working memory, and executive cognitive function (Murman, 2015). Age-related cognitive changes are associated with structural and functional alterations in the brain, such as modifications in neuronal structure without neuronal death, synaptic loss, and dysfunction of neuronal networks. In case of pathological aging, emerging evidence suggests presence of subtle cognitive decline in the preclinical stages of AD (Baker et al., 2017).

Current clinical trials are targeting preclinical stages of AD, where brain microstructural changes start many years prior to the diagnosis of AD dementia (Sperling et al., 2014, 2011b). To investigate the earliest cognitive changes associated with underlying AD pathology, cognitive composites are defined. For instance, the preclinical Alzheimer's cognitive composite (PACC5) focuses on measures of episodic memory, semantic memory, executive function, and global cognition (Papp et al., 2017).

The first clinical stage of AD, is labeled as mild cognitive impairment (MCI) due to AD (Albert et al., 2011; Perl, 2010), read BOX-1 for more details on different stages of AD. In MCI stage, the individuals experience slight memory loss, particularly for recent memories, while their daily functioning remains relatively unaffected (Albert et al., 2011; Soria Lopez et al., 2019). In AD dementia stage, the progression of neuropathology accelerates the rate of neuronal dysfunction, neuronal loss, and cognitive deterioration in time, often leading individuals to experience significant cognitive impairments that hinder their daily functional abilities such as language and visuospatial presentation, and executive function (McKhann et al., 2011; Murman, 2015).

1.4 Biomarkers' Interaction in AD

So far, we have presented different changes in the brain and cognition that might occur during AD. Recent research suggests a systematic sequence of pathogenic events on a global biomarker level, but little is known about the associations and dependencies of distinct

lesion patterns on a regional level (Dyrba et al., 2018). For instance, the level of atrophy, as assessed by imaging techniques, correlates with neuronal loss (Bobinski et al., 1999), Braak (I to VI) NFT stage (Jack et al., 2002; Whitwell et al., 2008; Zarow et al., 2005), but does not strongly correlate with amyloid-beta load measured by immunohistology (Josephs et al., 2008).

Several studies have investigated the relationship between pathologic patterns using multimodal imaging markers (Buckner et al., 2005; Grothe et al., 2016; Villain et al., 2010). These studies either assessed the statistical associations between biomarkers such as brain atrophy and metabolism or the correlation between two modalities in a univariate manner. For instance, (Whitwell et al., 2018) showed that the correlation between tau NFT and metabolism is larger than the correlation of tau NFT with gray matter volume all over the brain. Another study demonstrated that tau NFT seems to collocate much more with synaptic and neuronal loss than amyloid plaques (Musiek and Holtzman, 2015). Likewise, once AD cognitive symptoms are detected, tau NFT burden follows cognitive decline more closely than amyloid plaques (Musiek and Holtzman, 2015).

Synaptic loss have the strongest correlation with cognitive decline in patients with MCI and with AD (DeKosky and Scheff, 1990; Scheff et al., 2006; Terry et al., 1991). However, amyloid plaques might be required for tau NFT to expand from subcortical to cortical areas. Therefore, the relationships between AD hallmarks are more complex than first apprehended and could arise (partly) from relatively independent phenomena converging to AD.

From another perspective, iron accumulation in the brain is highly related to deficits in oligodendrocytes which are core cells for production of myelin content. Demyelination results in limited impulse propagation and severe neurological dysfunction (Wang et al., 2018) as the main role of myelin is to protect the axon, insulation, and to accelerate the saltatory conduction of nerve impulses. In the process of myelin recovery, the naked axons can be damaged and free toxic iron elements can be released which results in neuronal loss.

In a large cross-sectional study, (Jack et al., 2014) showed that the population frequency of amyloid-beta and NFT negative (normal biomarkers) was 100% at age 50 and decreased to 17% by age 89. The frequency of amyloid and NFT positive (AD with neurodegeneration) increased to 42% by age 89, while the frequency of amyloid negative, NFT positive (classified as “suspected non-Alzheimer pathology”, i.e., SNAP) increased to 24% by age 89. Consequently, AD pathology with neurodegeneration and SNAP with neurodegeneration became increasingly more common with age, affecting up to 66% of people by age 89, despite normal performance on cognitive testing. The high frequency of neurodegeneration without amyloid-beta positivity suggests that other biomarkers may play a more prominent role than amyloid-beta accumulation (Jack et al., 2014).

In the past decade, advancements in brain imaging techniques have indeed facilitated the investigation of myelination and iron accumulation in the brain *in vivo*. Studies using these new MRI methods reported results that align with *ex vivo* histological studies that have demonstrated the degeneration of myelin sheaths during healthy aging (Peters, 2002). For example, myelin water fraction as measured by multi-parametric maps (MPM) magnetization transfer saturation (MTsat) signal was found to decrease with aging in the corpus callosum as well as in frontal and parietal white matter (Callaghan et al., 2014). Additionally, in line with *ex vivo* evidence of increased iron content in basal ganglia in normal aging (Bulk et al., 2018), a positive correlation between iron deposit as measured by MPM R2* signal in the basal ganglia and age was found (Callaghan et al., 2014; Draganski et al., 2011). A more recent study, using the MPM protocol, showed age-related white matter volume, myelin, and iron loss in sensorimotor and subcortical areas paralleled by free water increase (Taubert et al., 2020).

Accordingly, the identification of the early events in the AD pathophysiological cascade with *in vivo* noninvasive methods is critical to increase our understanding of the disease and inform the search for a treatment.

There are several models about the progression of neuropathological markers of AD. According to the amyloid cascade hypothesis, amyloid plaques are the initial cause of AD, triggering tau NFT, synaptic and neuronal loss (Castello and Soriano, 2014; Jack et al., 2013). Initially, Jack et al. proposed a hypothetical model for the major biomarkers of AD, describing the temporal evolution of the biomarkers with respect clinical severity (Jack et al., 2010). Subsequently, they updated their model showing the temporal evolution in time instead of the clinical disease stage (Jack et al., 2013). In this model, as illustrated in the lower panel of **Figure 1-3** amyloid-beta accumulation, tau protein aggregation, neurodegeneration, atrophy, and memory deficits are accounted for staging the disease (Jack et al., 2013).

Other hypothetical models have been proposed for AD spread pattern. Intra-regional evolution models hypothesize the sequential pathological process as described in (Jack et al., 2013) within a single region and independent of other regions of the brain (Castello and Soriano, 2014; Drachman, 2014; Hardy and Allsop, 1991). Alternatively, the “neuron-to-neuron” hypothesis assumes a prion-like propagation of pathogenic proteins along structural connections in the brain (Hallbeck, 2013). Another model for progression of AD is based on the metabolic demands of the brain regions; for instance, regions that are active in the default mode network are particularly vulnerable to amyloid deposition, neuronal dysfunction, and, neuronal death (Buckner et al., 2005).

Dysfunctional oligodendrocytes and elevated iron levels are interconnected, and this interaction has a notable impact on myelin repair. Furthermore, increased levels of free iron can be toxic, resulting in oxidative stress, inflammation, cellular dysfunction, and ultimately, cell death (Bartzokis, 2011; Bulk et al., 2018; Calabrò et al., 2020). Therefore, it is also hypothesized that myelin breakdown and elevated iron levels are early events in the pathophysiology of Alzheimer's disease. (Bartzokis, 2004a) proposed a developmental model for cognitive decline and Alzheimer's disease (AD) that centers around myelin breakdown, which is linked to the unique vulnerability of late-developing oligodendrocytes. According to this model, myelin breakdown is a fundamental aspect of the earliest changes seen in both

brain aging and AD. Another perspective for the progression of AD, is spatial colocalization of brain iron deposits with amyloid plaques (van Bergen et al., 2016).

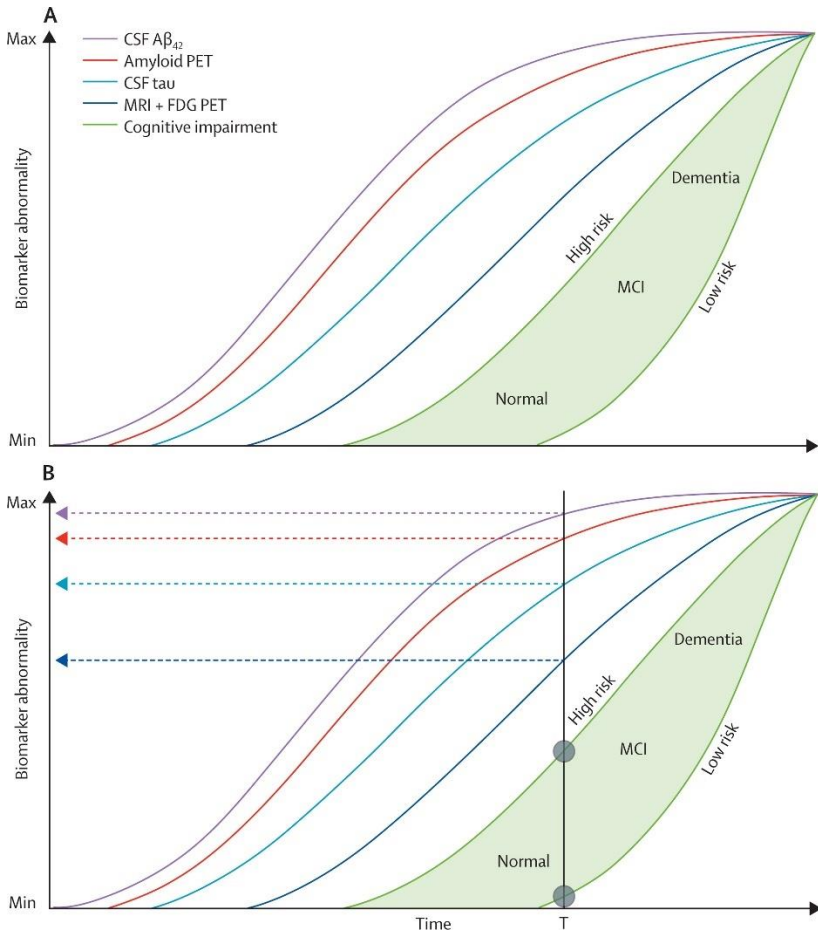


Figure 1-3. Revised model of dynamic biomarkers of the AD pathological cascade. (A and B) Neurodegeneration is measured by FDG PET and structural MRI (dark blue). All curves converge at the top right-hand corner of the plot, the point of maximum abnormality. Cognitive impairment is highlighted by green as a zone with low-risk and high-risk borders. (B) Operational use of the model. The vertical black line denotes a given time (T). Projection of the intersection of time T with the biomarker curves to the left vertical axis (horizontal dashed arrows) gives values of each biomarker at time T, with the lead biomarker (CSF A β_{42})

being most abnormal at any given time in the progression of the disease. People who are at high risk of cognitive impairment due to Alzheimer's disease pathophysiology are shown with a cognitive impairment curve that is shifted to the left. By contrast, the cognitive impairment curve is shifted to the right in people with a protective genetic profile, high cognitive reserve, and the absence of comorbid pathological changes in the brain, showing that two patients with the same biomarker profile (at time T) can have different cognitive outcomes (denoted by grey circles at the intersection of time T). $A\beta$ =amyloid-beta. FDG=fluorodeoxyglucose. MCI=mild cognitive impairment. (Jack et al., 2013)

All these findings indicate the possibility of co-localization of neuropathology in the brain. Despite numerous studies exploring the chronobiological progression of AD, very few studies specifically investigated the simultaneous presence of brain tissue characteristics within a single framework.

Correlation maps offer an easily interpretable way to observe how one disease process relates to another, both locally and distantly. However, univariate analysis methods present some limitations, such as the considerable number of multiple comparisons necessary to directly assess such correlations and the high computational cost (Avants et al., 2014). Multivariate methods can be implemented to overcome such limitations in high dimensional datasets. (Sintini et al., 2018) studied the linear relationship between 6 pairs of AD biomarkers (NFT, atrophy, metabolism, and diffusion tensor imaging). Their findings suggest a positive correlation between decreased metabolism (glucose consumption) and loss of gray matter volume (Sintini et al., 2018). A more recent study provided evidence for age-related spatial overlap between volume and tissue property (demyelination, and free water content as assessed by MPM quantitative maps) differences that affect predominantly motor and executive networks atrophy, in a large cohort of 966 individuals (Taubert et al., 2020).

To the extent of our knowledge, no one has studied co-occurrence of demyelination, iron accumulation, atrophy, and synaptic density in the context of Alzheimer's disease. This thesis aims to address the gap by examining the co-occurrence of image derived biomarkers for AD. Our objective is to incorporate these diverse biomarkers into a

comprehensive model, allowing us to explore their interaction in both gray matter and white matter.

1.5 Objectives and Thesis Outline

The objectives of this project revolve around addressing several questions related to co-occurrence of macro- and microstructural brain characteristics in the gray matter and white matter of the aging brain.

The primary objective of this thesis is to examine the microstructural alteration occurring in the brains of both healthy individuals and those diagnosed with AD, highlighting the differences in myelin and iron levels between these two groups. Additionally, we will investigate simultaneous demyelination, iron accumulation, synaptic degeneration, and atrophy through multivariate General Linear Model (GLM) analysis. Furthermore, we will look into the association of memory function and various brain image-derived biomarkers in healthy older adults. This investigation aims to determine whether the coexistence of multiple micro- and macro-pathologies within the brain could potentially serve as an indicator of forthcoming memory impairments.

The project was divided into three core studies, each centered around brain characteristics, aging, and cognition. To accomplish these objectives, we took advantage of three datasets: the UCB-H (Bastin et al., 2020) and COFITAGE (Chylinski et al., 2022; Narbutas et al., 2019; Van Egroo et al., 2019) datasets from previously defined projects at the GIGA CRC-ivi, Liège University, along with the Aging dataset (Callaghan et al., 2014) from the Wellcome Centre for Human Neuroimaging (WCHN), University College London (UK).

In the first study, we used the UCB-H dataset, which consists of 43 healthy and AD participants (37.2 % male, mean age = 72.6) and included MPM MRI images and [F^{18}] UCB-H PET data. In this study, first, we investigated the differences between (semi)quantitative maps indexing myelin and iron between healthy controls and AD patients. We also compared GM volume between the groups. Finally, we assessed all these characteristics in a multivariate model to test which combination of characteristics is triggering the difference between healthy brains and

AD brains in GM. This was the first study to assess myelination and iron accumulation, using MPM quantitative maps, synaptic density, and atrophy in one model.

In the second study, we explored the impact of age on the simultaneous occurrence of microstructural tissue property changes in healthy adults in a collaborative study with the WCHN. We compared our findings from the multivariate model with previously published results from multiple univariate GLM analyses (Callaghan et al., 2014). The dataset for this study consisted of MPM MRI data from 138 healthy adults (35.5 % male, mean age = 46.6). Our findings provide insights on the advantages of multivariate models for studying multiple simultaneous tissue properties in comparison to multiple univariate models.

For the third study, data was obtained from the COFITAGE dataset, a rich dataset with various modalities and longitudinal cognitive assessments from 101 healthy subjects (31.7 % male, mean age = 59.4). Having longitudinal cognitive test battery scores provided the opportunity to study the decline in cognition in healthy older adults. We examined the association between global memory, attention, and executive function as assessed by various cognitive scores, along with PACC5 and different tissue property maps, indexing myelin, iron, free water content, and GM and WM volume, in healthy older adults. Our findings provide insights about the primary regions in the brain correlating with cognition and its decline in normal aging.


In the discussion, we will provide a summary of our key findings. Specifically, we will discuss the differences observed in the brain microstructural properties between healthy adults and AD patients using quantitative neuroimaging techniques. Additionally, we will delve into our findings regarding a combination of quantitative maps of brain properties that could empower us in indicating the initially affected brain regions in AD.

Furthermore, we will extend our discussion to the possibility of identifying specific regions within the brain where the co-occurrence of

micro-structural alterations is more likely to manifest concerning individuals' age.

Moreover, we will explore the intricate relationship between cognitive performance and its decline concerning micro-structural characteristics within the brains of healthy older adults.

We will conclude our discussion by unveiling the limitations and future perspectives to complete this research.

Chapter **2** 

Statistical Methodology

Statistical modeling serves as a cornerstone in diverse analytical frameworks, providing a robust foundation for an array of applications. In this chapter, we bring a brief introduction to the importance of multivariate General Linear Model (mGLM) when investigating phenomena that are interconnected.

2.1 General Linear Model (GLM)

General Linear Model (GLM) is used in almost every statistical analysis. It is the foundation of the t-test, F-test, Analysis of Variance (ANOVA), Analysis of Covariance (ANCOVA), regression analysis, and many others e.g., multivariate methods including factor analysis, cluster analysis, multidimensional scaling, discriminant function analysis, canonical correlation.

When using a GLM, we hypothesize that the dependent variable can be explained by a weighted linear combination of a group of independent variables (covariates), in presence of errors that have normal distribution (Equation 2-1). In image processing, GLM is often used to examine the association between the signal within each voxel and specific covariates. In other words, a GLM would use some predictors to predict an observed phenomenon (Christensen, 2020)(Christensen, 2020). GLM can also be used to perform group comparisons. This can be done by including a categorical factor variable in our model, which allows for testing the difference between groups (e.g., patients vs. controls) while controlling for other factors.

$$Y=XB+E$$

Equation 2-1

In the context of quantitative MRI, GLM serves as a powerful analytical framework for investigating variations in tissue properties in the brain. However, as we explained in the introduction chapter, brain tissue properties are interconnected. Multivariate General Linear Model (mGLM) becomes particularly important in this context. mGLM allows researchers to investigate concurrent changes in multiple tissue property maps, considering their interdependencies. This capability is crucial for a comprehensive understanding of how various tissue characteristics evolve simultaneously, providing insights that might be overlooked in univariate analyses. The interconnected nature of

different tissue properties underscores the significance of adopting multivariate approaches, enhancing the richness and accuracy of interpretations in qMRI studies.

Throughout this thesis, the univariate GLM analyses were performed in SPM12 (www.fil.ion.ucl.ac.uk/spm).

2.2 Multivariate General Linear Model (mGLM)

The extension of GLM, known as the Multivariate General Linear Model (mGLM), accommodates scenarios where observations span multiple modalities. Expressed as Equation 2-1, this model incorporates matrices for observations ($Y_{n \times m}$), design ($X_{n \times k}$), model parameters ($B_{k \times m}$), and errors ($E_{n \times m}$). Where n can be taken as the number of subjects, m as the number of dependent variables (here, the number of different tissue property maps), and k as the number of predictors.

2.3 Statistical Testing in mGLM

The derivation of test statistics involves the computation of sums-of-squares and cross products (SSCP) matrices for both hypothesis ($SSCP_H$) and error ($SSCP_E$). Standard test statistics, including Pillai's trace, Wilk's lambda, Hotelling-Lawley trace, and Roy's largest root, offer diverse perspectives on the significance of observed effects (Hotelling, 1951; Lawley, 1938; Pillai, 1955; Roy, 1945; Wilks, 1932). The selection of an appropriate test statistic hinges on characteristics inherent in the data, acknowledging considerations such as population eigenvalues and the distribution of dependent variables. Approximations to F-statistics and corresponding degrees of freedom enable the calculation of p-values, contributing to the interpretability of results.

In our studies, we used the MSPM toolbox (Gyger et al., 2021), a newly developed toolkit for performing the multivariate GLM analysis and testing.

2.4 Canonical Component Analysis (CCA)

Generally, when using multivariate models, the calculation of a sufficiently large multivariate test statistic naturally leads to the question of the degree to which any of the dependent variables are contributing to the rejection of the null hypothesis. Although it is always possible to simply follow up any significant multivariate tests with multiple univariate tests, it is not favorable as doing multiple tests would increase the chance of false positives (Gyger et al., 2021; McFarquhar et al., 2016). Linear discriminant analysis (LDA), also called canonical component analysis (CCA) is a more relevant approach for calculation of the multivariate test statistics (Huberty and Olejnik, 2006).

For further details on the modeling and statistical testing in mGLM please refer to Appendix-A in Chapter 7.

Chapter 3

Multimodal imaging of microstructural cerebral alterations and loss of synaptic density in Alzheimer's disease

This chapter is based on our article published in the *Neurobiology of Aging* journal:

*Moallemian, S., Salmon, E., Bahri, M.A., Belyi, N., Delhaye, E., Balteau, E., Degueldre, C., Phillips, C., Bastin, C., 2023. **Multimodal imaging of microstructural cerebral alterations and loss of synaptic density in Alzheimer's disease.** *Neurobiology of Aging* 132, 24–35. <https://doi.org/10.1016/j.neurobiolaging.2023.08.001>*

Preface

In this chapter, we address the growing prevalence of neurodegenerative diseases, particularly Alzheimer's disease (AD), against the backdrop of increasing life expectancy. AD, constituting 60 to 80 percent of cases, presents a significant global health challenge (Calabrò et al., 2020). Despite a declining incidence, the aging population is expected to elevate AD prevalence. The pathological processes underlying AD, characterized by amyloid-beta plaques, tau neurofibrillary tangles, synaptic, and neuronal loss, unfold decades before clinical manifestations. Our study explores the early events in AD pathophysiology using noninvasive *in vivo* methods.

We investigate myelin and iron hypothesis, suggesting that myelin breakdown and increased iron levels are among the initial events in AD (Bartzokis, 2011). Histological studies indicate myelin breakdown in frontal and temporoparietal areas, correlating with altered iron accumulation and amyloid-beta plaques (Bulk et al., 2018; Van Duijn et al., 2017). Elevated iron levels, particularly in the hippocampus, are associated with cognitive decline (Zeineh et al., 2015). Leveraging novel neuroimaging tools, specifically Multi-Parameter Mapping (MPM), we aim to assess brain microstructure and investigate the link between myelin water fraction, iron content, and AD-related pathological changes.

Our primary objective is to employ quantitative MRI to detect *in vivo* microstructural differences in individuals with AD, characterized by significant amyloid burden, compared to healthy older individuals. While previous studies have explored iron content in AD, our study uniquely combines quantitative MPM maps to assess *in vivo* myelin and iron concurrently. We also aim to explore the co-occurrence of demyelination, iron accumulation, gray matter atrophy, and synaptic loss- as assessed by SV2-A-PET imaging.

By integrating findings from various imaging modalities, we seek to uncover potential relationships between myelin breakdown, iron accumulation, and synaptic density reduction in AD. Our cross-sectional study sets the stage for understanding the interplay of pathological

markers in the brain, laying the groundwork for future investigations into the chronobiology of these pathological changes.

3.1 Introduction

Concomitantly with an increase in average life expectancy, a major epidemiologic trend of the current century is the rise of neurodegenerative diseases worldwide, among which Alzheimer's disease (AD) is the most common type, with 60 to 80 percent of the cases (Calabrò et al., 2020). Despite an incipient decrease in incidence, AD prevalence is expected to rise because this neurodegenerative disease increases exponentially with age (Azam et al., 2021; Tan et al., 2014). It is recognized that AD pathological processes unfold decades before the emergence of clinical signs of cognitive decline (Dean et al., 2017; Gonneaud and Chételat, 2018; Tan et al., 2014). These pathological processes include a progressive accumulation of amyloid-beta plaques and tau neurofibrillary tangles (NFT), in addition to synaptic and neuronal loss (Gulisano et al., 2018; Jack et al., 2013; Spillantini and Goedert, 2013; Tan et al., 2014; Yin et al., 2021). According to the amyloid cascade hypothesis (Jack et al., 2013), amyloid plaques are the initial cause of AD, triggering tau NFT, synaptic and neuronal loss. Synaptic loss appears as the best correlate of cognitive decline in patients with Mild Cognitive Impairment (MCI) and with AD (DeKosky and Scheff, 1990; Scheff et al., 2006; Terry et al., 1991). Interestingly, in about 40% of cognitively normal older individuals, neurodegeneration (hippocampal atrophy) precedes detection of amyloid plaques (Jeremic et al., 2021; Villemagne et al., 2011). Accordingly, the identification of the early events in the AD pathophysiological cascade with *in vivo* noninvasive methods is critical to increase our understanding of the disease and inform the search for a treatment.

In the quest for early biomarkers, it has been suggested that changes in brain microstructure are among the first manifestations of AD (Bartzokis, 2011). Increased iron levels are associated with dysfunction of oligodendrocytes, notably impacting myelin repair. Moreover, an increase in free iron is toxic, inducing oxidative stress and inflammation, cell dysfunction, and, ultimately, cell death (Bartzokis, 2011; Bulk et al., 2018; Calabrò et al., 2021). So, it is hypothesized that myelin breakdown

and increases in iron levels are very early events in the physiopathology of Alzheimer's disease. In support of this "myelin and iron" hypothesis, histological studies showed that myelin breakdown in early AD occurs mainly in frontal and temporoparietal areas (Bartzokis, 2011; Bulk et al., 2018; Kalpouzos et al., 2017; Zecca et al., 2004). Increased iron content was also found in frontal and temporal areas of AD patients (Bulk et al., 2018; House et al., 2008). Moreover *ex vivo* studies showed that altered iron accumulation is positively correlated with the number of amyloid-beta plaques in these areas (Bulk et al., 2018; Duijn, 2017). Elevated iron content has also been observed in the hippocampus of AD patients (Zeineh et al., 2015). Additionally, higher levels of ferritin (i.e., the principal iron storage protein of the body) in the cerebrospinal fluid (CSF) are associated with the poorer cognitive performance of cognitively normal, MCI and AD participants, and predicted MCI conversion to AD (Aytton et al., 2015; Peng et al., 2021).

Novel neuroimaging tools can be used to assess brain microstructure. Indeed, specific MRI parameters have differential sensitivity for structural aspects of tissue such as fiber coherence, macromolecules, myelin, iron, and water content. Recently developed quantitative MRI techniques offer, through their sensitivity to microstructural tissue properties, a unique opportunity for establishing *in vivo* the link to findings of postmortem histological assessment of brain tissue. Notably, Multi-Parameter Mapping (MPM) has been used to create quantitative brain maps that lead to a highly specific inference of tissue properties such as myelin water fraction (i.e., myelination) and iron content in the gray matter (Draganski et al., 2011). Consistently with *ex vivo* histological studies indicating degeneration of myelin sheaths with healthy aging (Peters, 2002), myelin water fraction as measured by MPM magnetization transfer saturation maps (MTsat) was found to decrease with aging in the corpus callosum as well as in frontal and parietal white matter (Callaghan et al., 2014). Additionally, in line with *ex vivo* evidence of increased iron content in basal ganglia in normal aging (Bulk et al., 2018), MPM imaging detected *in vivo* a positive correlation between iron deposit in the basal ganglia and age (Callaghan et al., 2014; Draganski et al., 2011). Increased iron content was related to lower

blood oxygen level dependent (BOLD) signal in older adults (Kalpouzos et al., 2017). A more recent aging study on a large-scale cohort confirmed the age-related atrophy and demyelination, and reported an overlap between interregional volume and tissue property differences in aging that affected predominantly motor and executive networks (Taubert et al., 2020).

In this context, our main objective was to use quantitative MRI to detect *in vivo* microstructural differences (myelin water fraction and iron content) between individuals with AD characterized by significant amyloid burden in the brain and healthy older individuals (amyloid-negative and/or cognitively healthy). In AD, investigation of brain microstructure with quantitative MRI using MPM protocol has only recently started. One study (Acosta-Cabronero et al., 2016) used quantitative susceptibility mapping in MRI to show that AD patients have increased iron content in the putamen, caudate nucleus, and amygdala. The same authors (Acosta-Cabronero et al., 2013) indicated that in healthy older adults, iron accumulation can be found in frontal lobes, affecting brain regions related to motor functions. Steiger and colleagues observed a decrease in gray matter volume and myelin, and an increase of iron in widespread brain regions including the basal ganglia in older adults using quantitative MRI technique (Steiger et al., 2016). Another work directly evaluated, in healthy older participants, the concurrent relation between CSF markers of amyloid-beta and tau AD pathology, and MRI relaxometry-based measures of myelin content in the brain (Dean et al., 2017). They found that lower CSF amyloid-beta and higher tau levels were related to regional decreases in the brain MRI myelin measures, particularly in brain regions known to be preferentially affected in AD, including white matter in the frontal, temporal, corpus callosum, and cingulum regions.

To our knowledge, no study has used quantitative MPM to assess *in vivo* myelin and iron in AD concomitantly. Moreover, little is known about *in vivo* co-occurrence of cerebral microstructural changes and synaptic loss. The latter can be assessed with PET imaging using radiotracers binding to synaptic vesicle protein 2A (SV2-A). With SV2-A-PET imaging, AD-related decreased synaptic density was found in several

cortical areas and the thalamus, with the most significant effect size in the hippocampus (Bastin et al., 2020; Chen et al., 2018).

In the current study, co-occurrence of microstructural alterations with reduced regional cerebral uptake of [F^{18}]UCB-H indexing synaptic density was assessed with a multivariate model applied to the different imaging modalities (MPM and SV2-A PET). If myelin decrease and iron burden are early events preceding synaptic loss and neuronal death (Bartzokis, 2011), one should observe a co-occurrence in microstructural abnormalities and decreased synaptic density in the case of AD, likely in the hippocampus whose alteration drives symptoms in the patients (Bastin et al., 2020). Of note, in the current cross-sectional study, we cannot assess the chronobiology of pathological changes across the different modalities. Nevertheless, we hypothesize that, if pathological processes are triggering one another as suggested by (Bartzokis, 2011), one should observe co-localization of pathological markers in the brain.

3.2 Methods

3.2.1 Participants

The data come from a published study that focused on *in vivo* imaging of synaptic loss (Bastin et al., 2020). Two groups of older participants were included in the study. The first group consisted of 24 amyloid-positive patients from the AD continuum ($A\beta$ -positive group), which encompasses individuals diagnosed with mild cognitive impairment (MCI) as well as those diagnosed with probable AD. These patients were recruited from the Memory Clinic at Liege University Hospital. They were diagnosed based on current NIA-AA criteria (Albert et al., 2011; Jack et al., 2018; McKhann et al., 2011). As part of the initial diagnostic process, [F^{18}]FDG-PET was used as a biomarker of neurodegeneration in all patients. Also, global cognition was assessed with the Mini-mental state examination (MMSE). $A\beta$ positivity was determined based on [F^{18}]Flutemetamol-PET by qualitative visual inspection and by cortical standardized uptake value ratios (SUVR) above a quantitative threshold determined in a database of healthy older adults (Bastin et al., 2020). In $A\beta$ -positive group, 5 patients were

diagnosed with MCI (MMSE between 26 and 30) and 19 with probable AD, with MMSE scores between 14 and 26 (mild stage, MMSE > 20, n = 15; moderate stage, MMSE < 20, n = 4). The second group comprised 19 cognitively healthy controls (HC) (with MMSE between 28 and 30). In the HC group, amyloid-negativity was confirmed in eight participants. For participants who did not undergo an amyloid PET, because they refused an additional PET exam, they were considered healthy controls if they showed no or only minimal hippocampal atrophy on MRI, as assessed by visual inspection by a neurologist (Dubois et al., 2007). Both groups were matched for age, sex, and education. **Table 3-1** shows a summary of the participants.

Table 3-1. Demographics, clinical characteristics, and neuropsychological scores of AD and HC groups. Abbreviations: sd, standard deviation; MMSE, mini mental state examination; DMS48, visual recognition memory, Tstat, T-student statistics, df, degrees of freedom, F, female, M, male.

mean ± sd	AD(n = 24)	HC(n=19)	T(df)=Tstat, p-value
Age	73.08 ± 8.07	71.95 ± 4.58	T(41)=0.55, p=.59
Gender (F/M)	0.54 ± 0.51 (13/11)	0.53 ± 0.51 (11/8)	Chi ² =0.21, p=0.65
Education(years)	13.37 ± 3.35	13.1 ± 3.56	T(41)=0.25, p=.80
MMSE	23.71 ± 3.95	29.16 ± 1.12	T(41)=5.82, p<.001
Memory (DMS48) % Correct	81.50 ± 15.74	98.53 ± 1.87	T(41)=4.68, P<.001

3.2.2 Data Acquisition

Our data consists of dynamic PET and MRI.

SV2-A PET

Dynamic PET acquisitions were carried out using a Siemens/ CTI (Knoxville, TN) ECAT HR+ PET scanner. An intravenous bolus of [¹⁸F]UCB-H[37] of 157.06 ± 8.96 MBq was administered. For a total of 100 minutes, the dynamic PET was conducted with time frames of 6*10s, 8*30s, 5*120s, and 17*300s. All PET images were reconstructed using filtered back projection (Hann filter, 4.9 mm FWHM), including

corrections for measured attenuation, dead time, random events, and scatter using standard software (ECAT 7.1, Siemens/CTI, Knoxville, TN). The transaxial resolution in water, under these acquisition and reconstruction conditions, is 6.5–7 mm (voxel size 2.57 x 2.57 x 2.43 mm³). A mean unchanged plasma fraction was calculated for each group and used for modeling based on blood samples collected in 7 controls and 6 patients. Further information on PET acquisition and processing can be found in (Bastin et al., 2020).

Multi-parametric Mapping MRI

MRI data has been acquired on a 3T whole-body MRI-scanner (Magnetom Prisma, Siemens Medical Solution, Erlangen, Germany) using a standard 32-channel head receiving coil. The whole-brain MRI acquisitions included a multiparameter mapping protocol (MPM) (Weiskopf et al., 2013). This protocol allows the estimation of (semi)quantitative maps for various parameters, including magnetization transfer saturation (MTsat), proportional to myelin; proton density (PD), proportional to water content; transverse relaxation ($R2^*$), proportional to iron; and effective longitudinal relaxation ($R1$). The MPM protocol consists of 3 co-localized 3D multi-echo fast low angle shot (FLASH) acquisitions with 1 mm isotropic resolution and 2 additional calibration sequences to correct for inhomogeneities in the RF transmit field (Lutti et al., 2010). The FLASH datasets were acquired with predominantly PD, T1 and MT weighting determined by the repetition time ($TR = 24.5$ ms) and flip angle ($FA = 6^\circ$ for PD & MT, 21° for T1), referred to in the following as PDw, T1w and MTw echoes. MTw contrast was obtained using an additional off-resonance Gaussian-shaped RF pulse with 4 ms duration and 220 nominal flip angle, 2 kHz off-resonance before nonselective excitation. A high readout bandwidth of 320 Hz/pixel was used to minimize off-resonance and chemical shift artifacts (Helms and Dechent, 2009). Volumes were acquired in 176 sagittal slices using a 256x224 voxel matrix. GRAPPA parallel imaging was combined with partial Fourier acquisition to speed up acquisition time to approximately 20 min. Gradient echoes were acquired with alternating readout gradient polarity at 6 equidistant echo times [2.34, 4.68, 7.02, 9.36, 11.7,

14.04] ms. Two additional echoes were acquired for the PDw and T1w acquisitions at 16.38 ms and 18.72 ms.

B1 field mapping images (transmit B1+ and receive B1- fields) were also acquired to reduce spatial heterogeneities related to B1 effect, which was essential for proper quantification of T1 (or $R1=1/T1$) in particular. Finally, B0 field mapping images were acquired for image distortions correction: two magnitude images acquired at 2 different TE's, and pre-subtracted phase images.

3.2.3 Image data Processing

Collected data were anonymized and organized according to the Brain Imaging Data Structure (BIDS) (Gorgolewski et al., 2016) and its extensions for PET (Knudsen et al., 2020) and qMRI data (Karakuzu et al., 2022), the latter using BIDSme (<https://github.com/CyclotronResearchCentre/bidsme>), and the former with custom MATLAB scripts. All information needed for subsequent analysis was incorporated into the dataset. Data is available from the corresponding authors upon reasonable request.

MRI

To obtain the quantitative maps, MRI data were processed with SPM12 (www.fil.ion.ucl.ac.uk/spm) and the hMRI (<https://hmri.info/>) toolbox, where the latter is an extension to SPM (Tabelow et al., 2019). T1w, PDw, and MTw images acquired at multiple TEs were extrapolated to TE=0 to increase the signal-to-noise ratio and remove the otherwise remaining $R2^*$ bias (Tabelow et al., 2019). The TE=0 extrapolated MTw, PDw, and T1w images were used to calculate MT saturation, R1 and apparent signal amplitude A^* maps. A^* maps were rescaled to generate PD maps. All quantitative maps were corrected for inhomogeneities from local RF transmit field (B1+), using B1 and B0 field mapping images (Lutti et al., 2010). The receive bias field map (B1-) was used to correct PD maps for instrumental biases (Ashburner and Friston, 2005). $R2^*$ maps were estimated using the ESTATICS method from the three different FLASH acquisitions by accounting for the varying contrasts. The ordinary least squares (OLS) log-linear fit was also used to detect and down weight echoes affected by motion artifacts (Weiskopf et al., 2014).

R1 maps were corrected for the radio frequency (RF) transmit field inhomogeneity B1+ (Preibisch and Deichmann, 2009). Quantitative maps were segmented into gray matter (GM), white matter (WM), and cerebrospinal fluid (CSF) using the unified segmentation approach as implemented in SPM (Ashburner and Friston, 2005). Inter-subject registration of the GM and WM tissue maps was performed using DARTEL, a nonlinear diffeomorphic algorithm (Ashburner, 2007). This algorithm estimates the deformations that best align the tissue probability maps by iterative registration of these maps to their average. The tissue probability maps were then normalized to the stereotactic space specified by the Montreal Neurological Institute (MNI) template using the resultant DARTEL template and deformations. Example maps are illustrated in **Figure 3-1**. Then, for voxel-based morphometry (VBM) analysis, specific tissue-weighted smoothing, with a 3mm FWHM isotropic kernel, was applied to avoid mixing values from different tissues classes, as would happen with standard Gaussian smoothing.

A GM mask was created using the mean segmented MTsat image from all participants to be later used as an explicit mask in the statistical analysis.

PET

PET data were processed as described previously (Bastin et al., 2020). In brief, [F^{18}]UCB-H PET dynamic frames were corrected for motion without re-slicing. The images were corrected for partial volume effects (PVE) using the iterative Yang voxel-wise method implemented in the PETPVC toolbox (Thomas et al., 2016), with GM, WM, CSF and “other” as ROI masks. Kinetic modeling using PVE-corrected dynamic PET data and image-derived input function was done with PMOD (Version 3.7, PMOD Technologies, Zurich, Switzerland). Input function was derived from the dynamic images (Bahri et al., 2017) and corrected for metabolites using the measured group mean unchanged plasma fraction. Logan graphical analysis (with $t^* = 25$ min) was used to calculate the distribution volume (V_t) map of [F^{18}]UCB-H in the brain. Finally individual V_t maps were coregistered with their corresponding MTsat map, then their spatial normalization transformations were applied to warp the V_t maps in the same reference space.

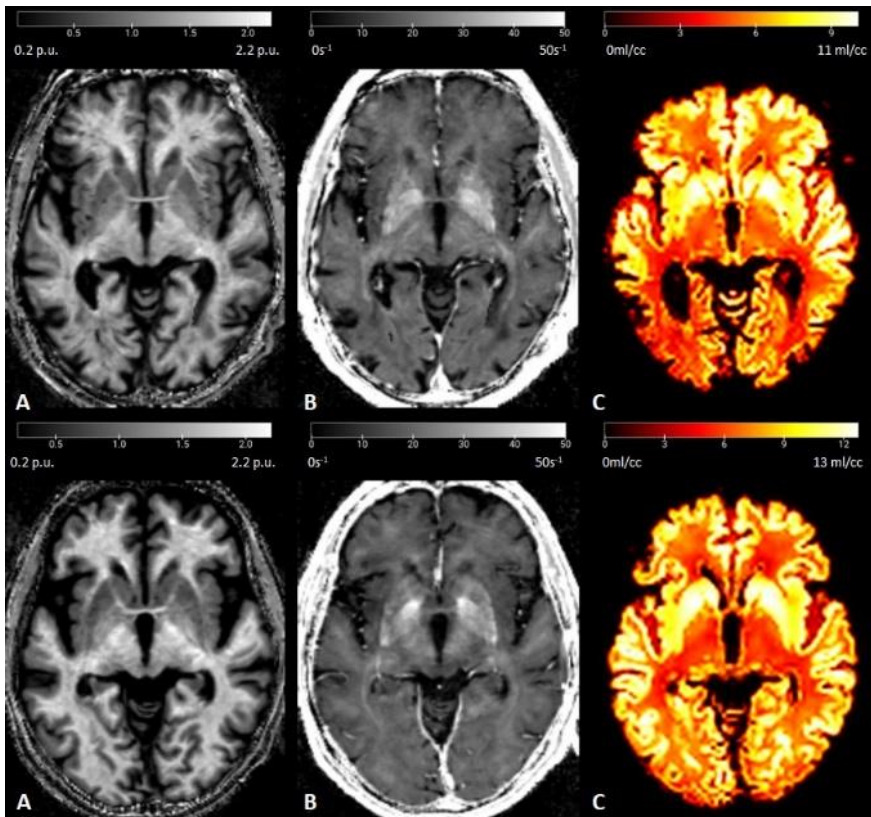


Figure 3-1. Example maps from two participants. First row, AD patient, Second row, healthy control. A) Magnetization transfer saturation, MTsat; B) Effective transverse relaxation rate, $R2^*$; C) $[F^{18}]UCB-H$ total volume distribution, V_t .

3.2.4 Statistical Analyses

All analyses focused on GM only as PET images indexing synaptic density are only interpretable for gray matter. Therefore, an explicit mask for GM was applied on all the analysis. Since each parametric map has a specific unit, e.g., Hertz for $R2^*$ images and ml/cc for V_t maps, their intensities are not directly comparable. Thus, all maps were Z-transformed - per modality and across participants - using the grand mean and variance over each voxel, to ensure comparability of different

modalities for our multivariate analysis. All statistical analyses were performed on standardized data.

For quantitative MRI, we decided not to investigate R1 and PD maps, as they are associated with multiple tissue properties at the same time, and would lead to underestimation of microstructural differences that we are interested in.

Three quantitative modalities (MTsat, R2*, and Vt) and GM density maps were individually analyzed using a univariate 2-sample t-test GLM with age and sex of the participants as covariates. We tested the difference between the two groups for each modality. The t-student contrast defined for MTsat, Vt, and GM volume (GMvol) maps was HC>AD, hypothesizing that healthy controls have more myelin, synapses, and GM volume than AD patients. For R2* maps, we used contrasted AD>HC, hypothesizing that R2* values in AD group are superior to those of healthy participants, as increased iron load is considered toxic.

A MANOVA model was specified using the design matrixes of the three univariate models in the MSPM toolbox (Gyger et al., 2021), a newly developed toolbox working under SPM as a multivariate extension of univariate GLM (Chen et al., 2014; McFarquhar et al., 2016). The multivariate GLM (mGLM) models the multivariate observations as $Y=XB+E$, where $Y_{43 \times 4}=[Y_1, Y_2, Y_3, Y_4]$ is the multi-modal data matrix, each row of Y represents one participant, and each column of Y represents one modality MTsat, R2*, GMvol, and Vt at a single voxel; and $X_{43 \times 4}=[X_1, X_2, X_3, X_4]$ is the design matrix, representing the AD and HC groups in the first two columns, and age and sex of the participants in the last two columns. The matrix B is a 4×4 matrix of size of regression coefficients; and E is the residual matrix of size 43×4 . Matrix B is estimated using an ordinary least square method.

The regression model can be used to partition the total variation in the outcome into explained variance and unexplained variance. In this sense, the total sums of square and cross products (SSCP) terms are calculated as: $SSCP_{Total}=SSCP_{Model}+SSCP_{Residual}$. The SSCP matrix is used to estimate the variance-covariance matrix of the predictor variables in linear regression analysis and can be presented as

$SSCP_{Total} = (\hat{Y}^T \hat{Y} - N \bar{y} \bar{y}^T) + E^T E$, where in our case $N=4$, the total number of observations. To test the null hypothesis that all the coefficients in B are equal to zero, we can compute the eigenvalues of $SSCP_{Model} SSCP_{Residual}^{-1}$. Then the Wilk's lambda summary statistics Λ is calculated based on the eigenvalues solving the equation of eigen-decomposition for the determinant matrix.

Here, we determine the canonical vectors for our test statistic. In this context, canonical vectors refer to the linear combinations of the original variables that maximize the separation between groups or conditions in the multivariate space (Tabachnick and Fidell, 2007). These vectors are determined by performing a multivariate analysis of variance (MANOVA) and extracting the canonical variates. The F-test is then applied to test the significance of the overall multivariate effect. Canonical vectors provide insights into the relationships between variables and facilitate the identification of the most influential factors driving group differences. For illustrative purposes only, we extracted the original values, after Z-transformation, from the MTsat, R2*, GMvol, and Vt maps used at the voxels within significant clusters, which corresponds to the difference in real tissue property values.

To test the hypothesis of the association between all dependent variables and contrasts among predictors, we applied this linear hypothesis: $H_0: CBL = 0$, where $L_{4 \times 4}$ is a full rank matrix to test the hypothesis, here an identity matrix to test the hypothesis for the joint effect of all modalities (columns of B). The contrast matrix $C = [1 \ -1 \ 0 \ 0 \ 0]$ would perform a standard F-test to assess the difference between the 2 groups, AD and HC. See (Tabachnick and Fidell, 2007) for mathematical details.

Additional group comparison was performed on MTsat, R2*, GMvol, and Vt maps after adjustment for age and gender covariates and masking for the significant ROIs resulted from the mGLM model.

Correlation analyses between memory, age, and sex with different modalities, was performed on the AD and HC group.

3.3 Results

Statistical inference was performed using a p-value $< .05$ “family-wise error rate” (FWER) corrected, at the voxel or cluster extent levels. For the latter, the cluster forming threshold used was a voxel level $p < .001$ uncorrected.

3.3.1 Univariate Analyses

Coordinates and anatomical labels of the peaks are presented in **Table 3-2**, showing the voxel-wise comparisons of two groups of AD and HC for different univariate analysis performed on MTsat, $R2^*$, GMvol, and Vt maps.

3.3.2 Magnetization Transfer Saturation (MTsat)

MTsat maps revealed a significant difference at cluster-level between AD patients and healthy controls after correcting for FWER ($P < .05$) which covers the right hippocampus and amygdala indicating lower values in AD than in controls. **Figure 3-2-A** shows the statistical parametric map of univariate analysis of MTsat maps at $p < .001$ uncorrected.

3.3.3 Effective Transverse Relaxation Rate ($R2^*$)

No significant difference in $R2^*$ maps, representative of iron level content in the brain, was detected between the groups. However, at a more lenient statistical threshold ($p < .001$ uncorrected), the results for $R2^*$ analysis show differences in the superior part of orbitofrontal cortex bilaterally as well as in the left hippocampus and right mid-temporal gyrus (see **Figure 3-2-B**).

3.3.4 Voxel-based Morphometry

We could identify significant reduction in GM volume in AD group ($p < .05$, corrected for FWER) bilaterally in hippocampus and fusiform cortex, and in left amygdala, olfactory bulb, and anterior cingulate cortex (**Figure 3-2-C**).

3.3.5 Total [F^{18}]UCB-H Volume Distribution

Vt data shows higher intensities in healthy controls compared to AD patients in the left and right hippocampus and amygdala at voxel-level ($P_{FWE} < .05$) as well as, right and left thalamus (**Figure 3-2-D**).

3.3.6 Correlation Analyses

The results from Pearson's correlation analyses in the AD group are presented in **Table 3-3**. There were significant correlations between MTsat and GMvol maps ($r = .462$, $p < .05$) in right para hippocampal cortex. A strong correlation was also observed in the left fusiform between MTsat and Vt maps ($r = .724$, $p < .001$). $R2^*$ and GMvol maps were negatively correlated in right para hippocampal cortex ($r = -.574$, $p < .01$) and left fusiform ($r = -.628$, $p < .01$). GMvol and Vt maps were found positively correlated in left hippocampus ($r = .472$, $p < .05$) and fusiform ($r = .447$, $p < .05$).

In the AD group, there were no significant correlations between memory (indexed by DSM48 score) and the different imaging modalities. Moreover, MTsat showed a negative correlation with age and gender in left and right hippocampus of AD participants ($r = -.431$, $r = -.445$, $p < .05$), as well as in left fusiform and temporal clusters.

The results of Fisher's z-transformation test support the homogeneity of regression slopes between the groups. Detailed correlation results for age and gender are presented in the Chapter 6, Appendix-B (**Table 7-1**, **Table 7-2**, **Table 7-3**, **Table 7-4**).

3.4 Multivariate Analysis

The multivariate GLM (mGLM) model, controlling for the effect of age and sex, shows significant difference at voxel-level ($PFWE < .05$) between the two groups in both left and right hippocampus and amygdala, left fusiform and superior temporal gyrus, and right para hippocampal (**Figure 3-3**). Coordinates and anatomical labels of the peaks are presented in **Table 3-4**. We also investigated the multicollinearity between different maps in the significant clusters of the mGLM model.

The variance inflation factor (VFI) in all cases is in the [0.98, 1.3] range, suggesting no multicollinearity.

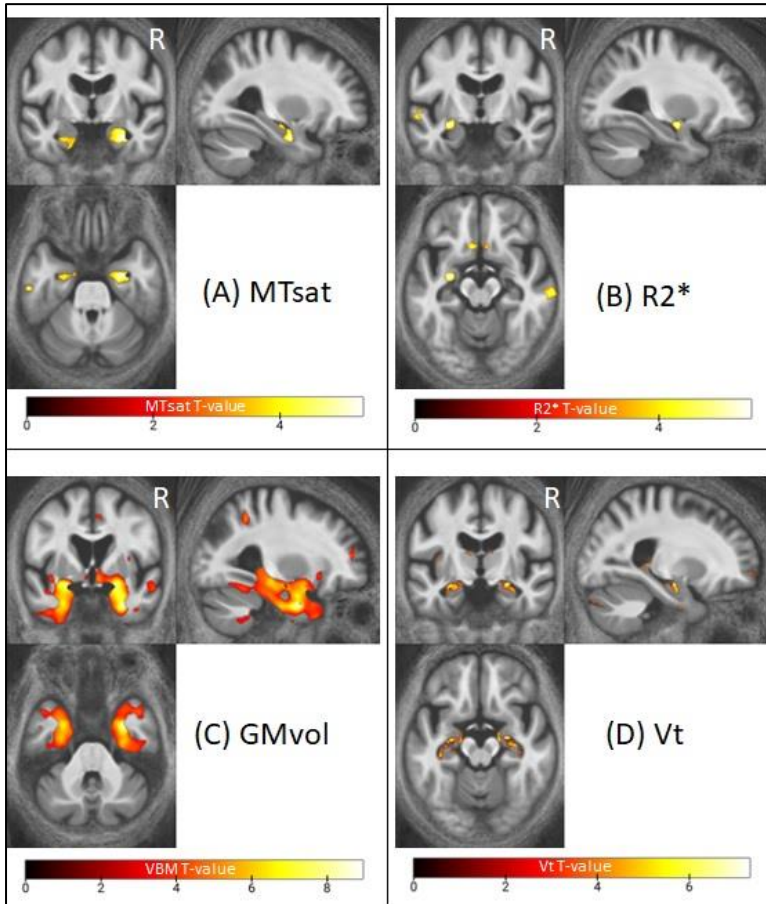


Figure 3-2. Statistical parametric maps of the univariate analysis for the difference between AD and HC groups. The SPMs were super imposed on the mean MTsat map for both groups on MNI space. For illustration purposes displayed at $p < .001$ uncorrected for FWER. Abbreviations: MTsat, magnetization transfer saturation; $R2^*$, effective transverse relaxation rate; gray matter volume; Vt, total volume distribution; FWER, family-wise error rate.

Table 3-2. Significant differences between AD participants and healthy controls for MTsat and Vt maps. Brain regions were labeled with the AAL3 atlas toolbox in SPM. This table shows up to 3 peaks (at least 8mm apart) within each cluster. Clusters were thresholded to contain >20 voxels. Coordinates are MNI coordinates. FWER correction was applied for P<0.05 at cluster level. Clusters highlighted with *, were significant at voxel level (P<.05).

peak [x y z] Coordinates	Cluster P-value	Cluster Size #voxels	Brain Region
MTsat (df=39)			
[31 -7 -27]	0.001	2508	Right Para hippocampal g
[37 -21 -12]			Right Hippocampus
[20 -11 -20]			Right Amygdala
GM volume (df=39)			
[30 1 -34]	0.000	5855	Right Hippocampus
[21 -1 -16]			Right Amygdala
[31 -24 -15]			Right Para hippocampal g
[-21 -1 -16]	0.000	4848	Left Amygdala
[-27 -11 -16]			Left Hippocampus
[-25 -4 -38]			Left Fusiform
[-24 -23 -23]	0.000	966	Left Hippocampus
[-40 -51 -15]	0.020*	30	Left fusiform
[6 5 -12]	0.009*	27	Right Olfactory blub
[-38 -12 12]	0.012*	57	Left Insula
[5 34 31]	0.019*	34	Right Mid. Cingulate
[-7 38 14]	0.016*	41	Left Pre. ACC
[52 -46 -16]	0.015*	47	Right Inf. Temporal
[36 -33 -23]	0.01*	69	Right Fusiform
Vt (df=39)			
[25 -11 -15]	0.000*	1462	Right Hippocampus
[30 -9 -21]			Right Amygdala
[17 -7 -15]			Right Para hippocampal g
[40 49 22]	0.008*	137	Right Mid. Frontal
[-27 -12 -16]	0.000*	1506	Left Hippocampus
[-22 -36 4]			Left Thalamus
[3 -6 8]	0.000	200	Right Thalamus

Key: FWER, family-wise error rate; MTsat, magnetization transfer saturation; Vt, total volume distribution; GM, gray matter; df, degree of freedom; g, gyrus.

Table 3-3. Pearson's correlations between different maps in AD group.
Significant correlations are highlighted by * p < .05, ** p < .01, *** p < .001.

	Pearson's r	p-value	Lower 95% CI	Upper 95% CI	Fisher's z	VIF
Left hippocampus						
MTsat – R2*	0.158	0.460	-0.262	0.528	0.160	1.026
MTsat -GMvol	0.281	0.184	-0.138	0.614	0.288	1.086
MTsat - Vt	0.122	0.569	-0.296	0.501	0.123	1.015
R2* - GMvol	0.053	0.805	-0.358	0.447	0.053	1.003
R2*- Vt	-0.066	0.758	-0.457	0.346	-0.066	0.996
GMvol - Vt	0.472*	0.020	0.085	0.736	0.513	1.287
Right hippocampus						
MTsat – R2*	0.234	0.271	-0.187	0.583	0.239	1.058
MTsat -GMvol	0.382	0.065	-0.025	0.681	0.403	1.171
MTsat - Vt	0.289	0.171	-0.130	0.620	0.297	1.091
R2* - GMvol	0.146	0.497	-0.274	0.519	0.147	1.022
R2*- Vt	-0.109	0.611	-0.491	0.308	-0.110	0.988
GMvol - Vt	0.187	0.383	-0.234	0.549	0.189	1.036
Right para hippocampal cortex						
MTsat – R2*	0.043	0.844	-0.367	0.438	0.043	1.002
MTsat -GMvol	0.462*	0.023	0.072	0.730	0.500	1.271
MTsat - Vt	-0.159	0.458	-0.528	0.261	-0.160	0.975
R2* - GMvol	-0.574**	0.003	-0.794	-0.223	-0.654	0.752
R2*- Vt	-0.012	0.954	-0.414	0.393	-0.012	1
GMvol - Vt	0.218	0.305	-0.203	0.571	0.222	1.050
Left fusiform						
MTsat – R2*	-0.070	0.745	-0.460	0.343	-0.070	0.995
MTsat -GMvol	0.302	0.151	-0.115	0.629	0.312	1.100
MTsat - Vt	0.724***	< .001	0.453	0.873	0.916	2.102
R2* - GMvol	-0.628**	0.001	-0.823	-0.301	-0.738	0.717
R2*- Vt	-0.061	0.778	-0.453	0.351	-0.061	0.996
GMvol - Vt	0.447*	0.029	0.053	0.720	0.480	1.250
Left temporal						
MTsat – R2*	0.180	0.400	-0.241	0.544	0.182	0.968
MTsat -GMvol	0.212	0.320	-0.209	0.567	0.215	0.955
MTsat - Vt	0.193	0.367	-0.229	0.553	0.195	0.963
R2* - GMvol	0.330	0.115	-0.085	0.647	0.343	0.891
R2*- Vt	-0.100	0.641	-0.484	0.316	-0.101	0.990
GMvol - Vt	-0.013	0.951	-0.414	0.392	-0.013	1

Key: CI, confidence interval; MTsat, magnetization transfer saturation; Vt, total volume distribution; R2*, effective transverse relaxation rate, GMvol, gray matter volume; VIF, variance inflation factor.

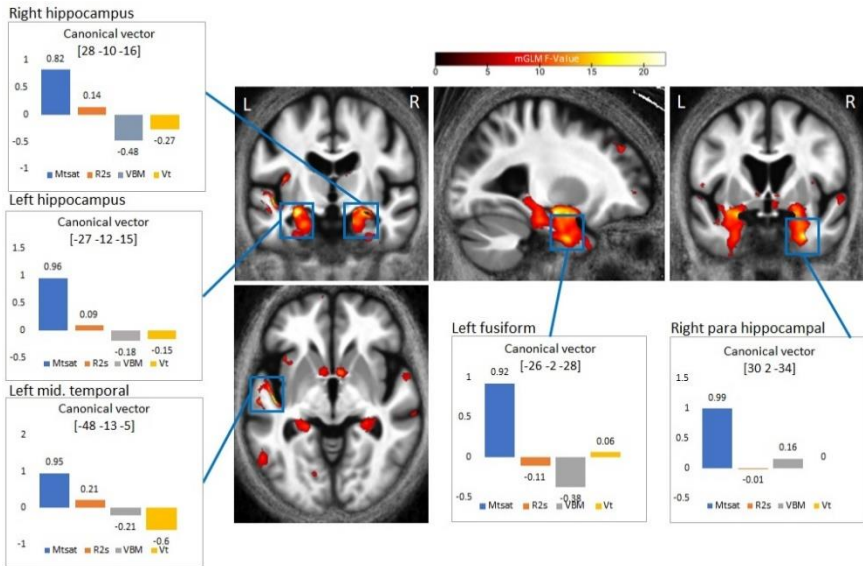


Figure 3-3. Statistical parametric map of the multivariate analysis for the difference between AD and HC groups. The mGLM results were super imposed on the mean MTsat map for both groups in MNI space. For illustration purposes displayed at $p < .001$ uncorrected for FWER. Canonical vectors for the peak voxel of each cluster in Table 4 are depicted in colored bars (blue=MTsat, orange=R2*, gray, GM vol., yellow=Vt) with arbitrary units. Abbreviations: MTsat, magnetization transfer saturation; R2s, effective transverse relaxation rate; GMvol, gray matter volume; Vt, total volume distribution; FWER, family-wise error rate.

3.4.1 Canonical vectors

Canonical vectors are evaluated for the mGLM model for each modality. The canonical vectors at the peak voxel of significant clusters presented in **Table 3-4** are illustrated in **Figure 3-3** with colored bars. They suggest that MTsat maps were the most contributing factor to the observed difference between AD and HC groups.

The violin plots in **Figure 3-4** represent the distribution of mean voxel values across participants within different modalities and the significant clusters from the mGLM model in the original maps (after Z-transformation and correcting for age and gender). Group comparison

for each ROI was computed with Student t test ($p < 0.05$) as presented in **Table 3-5**. A significant difference was detected in the left fusiform and temporal for MTsat maps. In $R2^*$ maps, we could indicate a statistically significant difference in the left hippocampus. GM volume was significantly different in all the selected ROIs between the groups. Significant differences were observed in the right para hippocampal and left temporal cortices.

Table 3-4. Significant differences between AD and HC groups in the mGLM model. Brain regions were labeled with the aal3 atlas toolbox in SPM. This table shows up to 3 peaks (at least 8mm apart) within each cluster. Clusters were thresholded to contain >20 voxels. FWER correction was applied for $P < .05$ at cluster level. Clusters highlighted with *, were significant at voxel level ($P < 0.05$).

mGLM (df=36)			
peak [x y z] Coordinates	Cluster P-value	Cluster Size #voxels	Brain Region
[-27 -12 -15]	0.000*	569	Left Hippocampus
[-22 0 -16]			Left Amygdala
[28 -10 -16]	0.000*	707	Right Hippocampus
[19 -2 -16]			Right Pallidum
[22 -8 -21]			Right Amygdala
[30 2 -34]	0.000*	111	Right Para hippocampal g
[-26 -2 -38]	0.002*	54	Left Fusiform
[-48 -13 -5]	0.006*	30	Left Sup. Temporal

The multivariate approach results for the difference in the right hippocampus go along with those of the univariate analyses of MTsat, GMvol, and Vt maps; narrowing the regions in which different micro- and macrostructural alterations coincide.

Table 3-5. ROI based voxel-level group comparison in MTsat, R2*, GM volume, Vt maps. The ROIs were selected from the statistical parametric map of the mGLM model. All maps were masked for these ROIs, then T-tests were performed for confidence interval of .95% on the adjusted values for age and gender.

Modality	T(df)=t-stat	P_value	Mean_diff ± sd	Cohen's d
Left hippocampus, #voxels per cluster = 569				
MTsat	T(41)= -1.6	P = .12	- .44 ± 0.90	0.49
R2*	T(41)= 2.53	P = .01	.59 ± 0.74	0.79
GMvol	T(41)= -6.93	P < .001	-1.38 ± 0.65	2.14
Vt	T(41)= -2.68	P = .01	-.58 ± 0.71	0.81
Right hippocampus, #voxels per cluster = 707				
MTsat	T(41)= -2.71	P <.001	-.70 ± 0.82	0.83
R2*	T(41)= 1.87	P = 0.07	.44 ± 0.75	0.59
GMvol	T(41)= -7.50	P < .001	-1.47 ± 0.62	2.34
Vt	T(41)= -3.19	P < .001	-.69 ± 0.71	0.96
Right para hippocampal cortex, #voxels per cluster = 111				
MTsat	T(41)= .50	P = .62	.14 ± 0.91	0.16
R2*	T(41)= 2.15	P = 0.38	.59 ± 0.87	0.68
GMvol	T(41)= -7.16	P < .001	-1.47 ± 0.67	2.20
Vt	T(41)= -2.09	P = .04	-.51 ± 0.81	0.63
Left fusiform, #voxels per cluster = 54				
MTsat	T(41)= -2.17	P = .04	-.62 ± 0.90	0.68
R2*	T(41)= -.44	P = .66	-.13 ± 0.99	0.13
GMvol	T(41)= -5.97	P < .001	-1.35 ± .72	1.86
Vt	T(41)= -1.80	P = .07	-.49 ± 0.87	0.57
Left Sup. Temporal, #voxels per cluster = 30				
MTsat	T(41)= -1.72	P = .09	-.51 ± .95	0.54
R2*	T(41)= 2.78	P = .09	.79 ± .93	0.85
GMvol	T(41)= -3.46	P < .001	-.95 ± .91	1.04
Vt	T(41)= -2.27	P = .03	-.59 ± .85	0.69

Key: MTsat, magnetization transfer saturation; R2*, effective transverse relaxation rate; Vt, total volume distribution; GMvol, gray matter volume; mGLM, multivariate GLM; df, degrees of freedom; diff, difference; sd, standard deviation.

3.5 Discussion

In this study, we investigated the association of myelination, iron accumulation, gray matter volume, and synaptic density, in patients with Alzheimer's disease (i.e., presence of cerebral amyloid burden) compared to healthy individuals (with no/minimal hippocampal atrophy) in a univariate and multivariate manner to discuss the co-occurrence of these AD-related neuropathological events at the voxel level.

The three different microstructure markers are assumed to play a role during AD, with a hypothesized cascade of pathological processes whereby increased iron and decreased myelin would lead to neuronal death and a reduction of synapses (Bartzokis, 2011).

Only a longitudinal study could capture this hypothetical chronobiology. Nevertheless, we hypothesized that, when reaching the clinical stage where amyloid-positive individuals demonstrate symptoms of cognitive decline, co-occurrence of alterations in the myelination, iron level, and synaptic density should be seen if they were linked in previous stages.

On the other perspective, macrostructural tissue loss has proven to be a sensitive marker for neurodegeneration despite its poor pathologic specificity (Mc Donald et al., 2010). Macrostructural atrophy was observed where microstructural abnormalities occurred, but correlations differed in different brain regions. Patterns of GM volume loss and A β aggregation in mild cognitive impairment and AD patients in frontal regions (Wirth et al., 2018).

3.5.1 Myelination

Taubert et al. showed an age-related myelin loss in the somatosensory and motor cortices as well as in thalamus nuclei (Taubert et al., 2020). Here, we reported a significant difference in the right hippocampus, indicating less myelin content in AD patients than healthy controls. At a more lenient statistical threshold ($p < .001$ uncorrected), there was a bilateral difference between groups indicating less myelin content in bilateral hippocampi in AD. This asymmetry of myelin deficits

at the strictest statistical threshold can be related to our small sample size (only 24 participants within the AD continuum). These results agree with the previous findings on myelin deficits that lead to motor dysfunction, impaired cognitive functions, psychiatric disorders, and neurodegenerative disease (Chen, 2021; Wang et al., 2018). To assess the asymmetry of GM myelin alterations in AD, future studies with larger sample sizes and specifically designed analyses could provide more insights.

We also could show positive correlations between myelination, as indexed by MTsat map, and GM volume in AD, suggesting concurrence of GM loss and demyelination in the right para hippocampal area. Myelination was also highly correlated with synaptic density in the left fusiform. Our findings supports previous works that show myelin deficits are shown to relate to neurological setbacks such as motor dysfunction and neural degeneration (Wang et al., 2018). More generally, little is known about the GM myelination in the brain (Timmler and Simons, 2019), the specific relationship for myelination in gray matter is less well-studied. This is the first study to investigate myelination in GM using quantitative MRI method in Alzheimer's disease.

3.5.2 Iron level

Studies on brain aging using the MPM approach demonstrated consistent findings on widespread negative correlation between age and MT saturation indicative for myelin loss paralleled by positive correlations between age and R2* in basal ganglia interpreted as iron content increases (Callaghan et al., 2014; Draganski et al., 2011; Taubert et al., 2020). We could not confirm the correlation between myelin and iron in our AD group. Previous *in vivo* studies (Duijn, 2017; Zeineh et al., 2015) showed that although iron content in the brain cortex and hippocampus is not affected by normal aging, in case of AD, accumulation of iron is observed in plaques, activated iron-containing microglia, and, in the most severe cases of AD, in the mid-cortical layers along myelinated fibers. Duijn et al also showed a difference in iron and myelin distribution in frontal cortex between the healthy controls and

AD patients that are visible after development of AD pathological hallmarks (Duijn, 2017).

We didn't observe any significant group difference (at voxel level) at the corrected statistical threshold for $R2^*$ maps indicative of iron content. However, at a more lenient statistical threshold ($p < .001$ uncorrected), we observed an increase in the iron content bilaterally in temporal lobe, and olfactory bulb, left hippocampus, and right supra marginal gyrus.

Su et al. reported that the iron content in the brain increased in one year compared to the baseline in AD participants and that iron accumulation was correlated with the neuropsychiatric behavior of participants (Su et al., 2016). Here, we showed a negative correlation between iron and GM volume in the right para hippocampal gyrus and left fusiform. The voxel-level comparison in the left hippocampus shows a significant mean difference between the groups.

3.5.3 GM volume

Voxel-based morphometry analysis showed bilateral difference between our groups, indicating loss in GM volume in AD patients consistently with the ROI comparisons, which are in accordance with aging studies that illustrate bilateral GM loss with respect to aging covering amygdala and hippocampus (Callaghan et al., 2014; Taubert et al., 2020). AD patients also showed reduced GM volume in left insula, right olfactory bulb, and cingulate gyrus.

Although a correlation between memory and GM volume in hippocampus was expected (Dubois et al., 2007), here, we could not detect a significant correlation in our AD group perhaps due to the small size of the group.

3.5.4 Synaptic density

Our findings on the synaptic density, which is indexed by the V_t maps, show that synaptic loss occurred bilaterally in the hippocampus, where we could detect differences in the myelination and GM volume. Other regions that faced decreased synaptic density are the right and

left thalamus. These results agree with previously published findings in (Bastin et al., 2020).

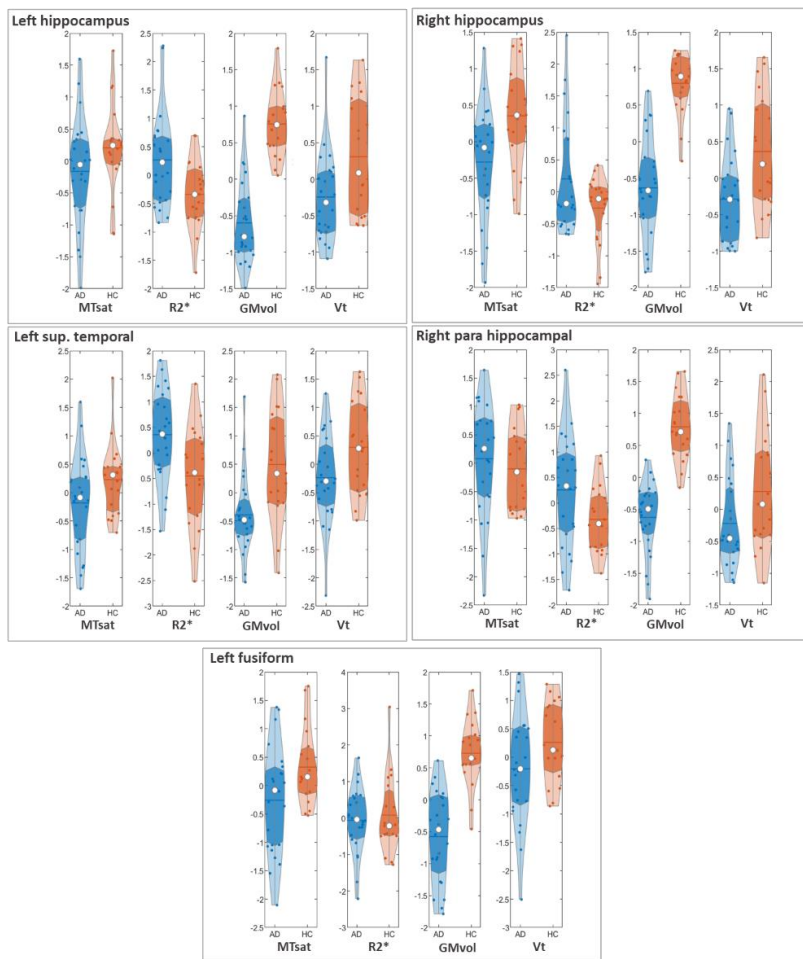


Figure 3-4. Raw voxel distribution of Z-transformed maps within each mGLM significant cluster. Each violin plot represents the distribution of the mean values across participants within each AD (in blue) and HC (in red) cohort in the original map, after adjusting for age and gender. White circles represent the median value within each group per cluster. The range of y axes is based on the variations within each modality. The first and third quartiles are shown with darker shadows within each violin. The mean value within each group per modality and cluster is shown with the horizontal line. Abbreviations: MTsat, magnetization transfer saturation;

R2s, effective transverse relaxation rate; GMvol, gray matter volume; Vt, total volume distribution; mGLM, multivariate GLM.

3.5.5 Simultaneous brain alterations

The most important findings are provided by the multivariate results indicating that there is a significant co-occurrence of demyelination, iron accumulation, and GM and synaptic loss, in the hippocampal area bilaterally, left fusiform and temporal regions of AD brains compared to healthy brains. A recent study on aging indicates a complex pattern of atrophy, demyelination, and iron content change in the somatosensory cortex and motor area (Taubert et al., 2020).

Assuming that the probability maps are independent, the canonical vector information that measures the contribution rate of each modality within the multivariate model shows that in the clusters derived from statistical parametric map from mGLM, MTsat maps contribute the most to the observed difference, while R2* maps contribute the least in all clusters (see **Figure 3-3**). Currently, it is not possible to summarize and evaluate whether the profile of canonical vectors within a particular cluster is uniform or diverse. Furthermore, the interpretation of the findings is limited due to the lack of directionality of effects based on F-tests.

Comparisons of the original mean voxel values from the Z-transformed maps within the regions that the mGLM model could detect as significantly different between the groups suggest that most of these maps are independent. As a result, the canonical vectors are reliable measures for demonstrating the contribution rate of different image-derived biomarkers in the brain.

3.5.6 Limitations and conclusion

One limitation of the current study is the fact that only eight HC participants had a [F^{18}]Flutemetamol PET scan to confirm A β -negativity. Although participants who did not undergo an amyloid PET were considered controls if they showed no or only minimal hippocampal atrophy on MRI, as assessed by visual inspection by a neurologist

(Dubois et al., 2007), this does not preclude the possibility of the A β -positivity of some of the healthy controls. Despite this potential uncertainty, it is noteworthy that the AD group still showed a decrease in synaptic density in the hippocampus at voxel-level analysis. Another limitation is the lack of verification of the microstructural changes of the brain in different stages within the AD group, which consisted of participants at various stages. There is still the need to conduct a longitudinal study from a large dataset that contains participants in different stages of AD. This would provide valuable insights into the chronobiology of microstructural changes and enable early detection of neurodegenerative diseases. Additionally, voxel-based quantification (VBQ) technique could be employed to preserve the quantitative value of the original qMRI maps (Draganski et al., 2011). Furthermore, future research should explore the use of quantitative susceptibility mapping (QSM) to overcome the limitations of R 2^* , as it is independent of water content, echo time, and field strength (Li et al., 2021).

Although MTsat maps are suggested to be proportional to the myelin content in the brain, they might also carry information on other macromolecular compounds in the brain that might reduce the specificity of MTsat to myelin alone. Inhomogeneous magnetization transfer (ihMT) is an alternative variant for MT that can address this issue (Munsch et al., 2021; Varma et al., 2020)

In conclusion, in this study, we compared individuals with Alzheimer's pathology (amyloid positive) and healthy controls (HC) with multiple univariate and multivariate general linear models (GLMs) for three semi-quantitative maps (MTsat, R 2^* , and Vt) as well as gray matter (GM) volume. The complex interaction between various AD risk factors, such as myelination, iron accumulation, and neural degeneration, necessitates the use of a multivariate analytic approach. This approach is preferred over conducting multiple univariate comparisons for each modality studied, as it reduces the risk of false positives associated with multiple testing and increases sensitivity.

Although our study had a small sample size, the findings suggest that combining different image-derived AD risk factors in a multivariate

analysis allows for the identification of specific brain regions where multiple neuropathological processes associated with the early stages of AD coincide. In addition to considering iron content and myelin using quantitative MRI, the novelty of our study lies in the comprehensive assessment of combined AD image-derived biomarkers across the entire brain. In summary, our study underscores the importance of investigating AD from various pathological perspectives, as it is believed to involve a cascade of processes. By characterizing AD using non-invasive imaging techniques, we enhance the opportunity to detect and study the disease in its early stages, when interventions are most likely to be effective.

Chapter summary

Multiple neuropathological changes are involved in Alzheimer's disease (AD). AD hallmark biomarkers are amyloid-beta, tau pathology, and neuronal and synaptic loss. Other possible brain tissue-related biomarkers, such as iron and myelin content in the brain, are less frequently studied. Thanks to quantitative MRI (qMRI), tissue parameters such as magnetization transfer (MT), effective transverse relaxation ($R2^*$), and proton density (PD) can be determined quantitatively, enabling the detection of microstructural tissue-related alterations in aging and neurodegenerative diseases. The current study investigated the co-occurrence of neurodegeneration (as measured with synaptic density), increased iron content, and decreased myelin content in Alzheimer's disease. The study involved 24 amyloid-positive patients (AD, 11 males) and 19 healthy controls (HC, 9 males). All participants underwent a multi-parameter mapping MRI protocol, from which quantitative maps for MTsat and $R2^*$ were estimated. Synaptic density was indexed by the total volume distribution map (V_t) derived from [F^{18}]UCB-H PET imaging. First, groups were compared with univariate statistical analyses applied to $R2^*$, MTsat and V_t maps. Then multivariate General Linear Model (mGLM) was used to detect the co-occurrence of changes in $R2^*$, MTsat, and V_t at the voxel level. Univariate GLM analysis of $R2^*$ showed no significant difference between the two groups. In contrast, the same analysis for MTsat resulted in a significant between-group difference in the right hippocampus at the cluster level with a corrected threshold (p -value $< .05$). We also could detect a reduction in GM volume in AD patients bilaterally in the hippocampus, amygdala, and fusiform, right olfactory bulb, and anterior cingulate gyrus compared to the HC group under a corrected threshold for family wise error (p -value $< .05$). The mGLM analysis revealed a significant difference in both right and left hippocampus between the AD and HC groups, as well as in the left precuneus, right middle frontal, and left superior orbitofrontal gyrus when all three modalities were present, suggesting these regions as the most affected despite the diverse changes of myelin, iron, and synapse degeneration in AD. Here, the mGLM is introduced as an alternative for multiple comparisons between different modalities, as it reduces the risk of false positives due to the multiplicity of the tests while informing about the co-occurrence of neuropathological processes in dementia.

Chapter 4

Multivariate Age-related variations in quantitative MRI maps: Widespread age-related differences revisited.

This chapter is based on our article submitted as a preprint in MedRxiv:

Moallemian, S., Bastin, C., Callaghan, M. F., Phillips, C., “Multivariate Age-related analysis of variance in quantitative MRI maps: Widespread age-related differences revisited”. medRxiv 2023.10.19.23297253. <https://doi.org/10.1101/2023.10.19.23297253>

Preface

Aging emerges as a primary risk factor for neurodegenerative diseases like Alzheimer's (AD), Parkinson's (PD), and frontotemporal lobar dementia (FTD) (Azam et al., 2021; Jeremic et al., 2021).

In this chapter, we explore concurrent alterations in brain tissue properties with respect to age. We will focus on (semi-)quantitative metrics, including $R2^*$, $R1$, PD, and MTsat, as well as gray and white matter volume maps.

Studies have shown an age-related decline in the brain myelin content (Callaghan et al., 2014; Peters and Sethares, 2002; Tian et al., 2022). On the other hand, iron accumulation with respect to age was confirmed in some aging studies within the putamen and supplementary motor area (Callaghan et al., 2014). Callaghan and colleagues (2014) also reported negative correlations between $R1$, and age bilaterally along the optic radiation and in the genu of the corpus callosum. They identified negative correlations between effective proton density and age in the putamen, pallidum, caudate nucleus, and the red nucleus (Callaghan et al., 2014).

By reanalyzing data from Callaghan et al. (2014) using a multivariate modeling approach, in gray and white matter separately, in the MSPM toolbox, we aim to assess the advantages of this methodology over conventional multiple univariate analysis. This technical paper offers insights into the sensitivity and specificity of our approach, shedding light on the nuances of aging-related changes in the brain's microstructure and providing a foundation for future investigations into neurodegenerative diseases. Finally, we will indicate regions in the brain that undergo simultaneous microstructural and macrostructural changes during healthy aging, thanks to the multivariate analysis approach.

4.1 Introduction

Aging is an inevitable part of our lifecycle that is associated with physical deterioration of different organs. Various hallmarks of aging have been identified over the past years that associate with neurodegenerative pathological changes in the brain, making age a primary risk factor for most neurodegenerative diseases including Alzheimer's disease (AD), Parkinson's disease (PD), and frontotemporal lobar dementia (FTD) (Azam et al., 2021; Jeremic et al., 2021).

Quantitative MR imaging (qMRI) enables us to extract sensitive and specific information about the microstructural properties of the brain tissue *in vivo*, such as axon, myelin, iron and water concentration (Weiskopf et al., 2021). The estimation of (semi-)quantitative metrics normally includes effective transverse relaxation rates ($R2^*$), which is primarily sensitive to iron, longitudinal relaxation rate ($R1$), which is sensitive to iron, myelin and water content, proton density (PD), indicative of free water content, and magnetization transfer saturation (MTsat), associated with macromolecular content, predominantly myelin (Tabelow et al., 2019; Taubert et al., 2020)

Many studies of aging focus on alterations in the nervous system, such as (de-)myelination or iron accumulation (Peters, 2002; Tian et al., 2022). Callaghan et al., (2014) investigated age-related differences of biologically relevant *in vivo* measures over the course of normal aging using quantitative multiparameter mapping (MPM) and showed significant demyelination in white matter (WM), concurrent with an increase in iron levels in the basal ganglia, red nucleus, and extensive cortical regions, but decreases along the superior occipitofrontal fascicle and optic radiation. Steiger et al. investigated the difference in iron and myelin levels between two groups of young and older participants using qMRI, and showed that age-related higher levels of iron are accompanied by a negative correlation of iron and myelin in the ventral striatum (Steiger et al., 2016). Although demyelination primarily affects the WM of the brain, recent research shows that it can also occur in gray matter (GM), which is made up of cell bodies of neurons. Studies have shown that gray matter myelination can occur during development,

particularly in the prefrontal cortex, and may continue throughout late adulthood in response to learning and experience (Fields, 2008; Timmler and Simons, 2019). Khattar and colleagues assessed the association of myelination and iron accumulation in the aging brain of a cohort of 21-94 year-old healthy controls and found a negative correlation between whole brain myelin water fraction and iron content in most brain regions; they also highlight that the myelination continues until middle age overall in the brain (Khattar et al., 2021). Taubert et al., (2020) reported robust evidence for spatial overlap between volume, myelination, and iron decomposition changes in aging that affect predominantly motor and executive networks under a modified normal probability curve approach from the Permutation Analysis of Linear Models (PALM) (Winkler et al., 2016, 2014) toolbox.

In this technical note, we re-analyze the data from (Callaghan et al., 2014) with a multivariate modeling approach as implemented in MSPM toolbox (Gyger et al., 2021) to assess the advantages of such an approach, in term of sensitivity and specificity, over the conventional multiple univariate analysis.

4.2 Method

4.2.1 Participants and data preprocessing

We took advantage of the processed data from (Callaghan et al., 2014), which include 138 healthy participants aged 19-75 years (35.5% male, mean = 46.64, s.d = 21). Quantitative multiparameter maps (R1, R2*, PD, and MTsat) were reconstructed with the VBQ toolbox, a preliminary version of the hMRI toolbox (Draganski et al., 2011; Tabelow et al., 2019). Processing steps included segmentation and diffeomorphic morphing to MNI space using DARTEL (Ashburner, 2007). Tissue-weighted smoothing (for GM and WM separately) with a 3mm FWHM isotropic kernel applied to account for residual misalignment while preserving the quantitative nature of the data. Finally, group level GM and WM masks were created to be further used as exclusive masks in the statistical analysis. For full details see (Callaghan et al., 2014).

4.2.2 Univariate GLM analyses

In this re-analysis, the 4 resulting sets of qMRI maps were z-transformed per modality and across subjects to ensure comparability between maps utilizing the mean and variance over each voxel. This procedure ensured comparability of different modalities for our multivariate analysis. The univariate general linear models were performed on each map (after z-transformation) using age, gender, total intracranial volume (TIV), and scanner (TRIO) as regressors. To assess the correlation between the individual tissue property maps and age, an F-test was performed on each map at voxel-level over GM and WM separately. All univariate statistical analyses were performed under the general linear model framework in SPM12, considering two p-values, .05 and .0125, family wise error rate corrected (FWER) thresholds. The latter threshold accounts for the fact that for both tissue classes, 4 similar inferences are performed (one per map) thus applying a Bonferroni correction the applied threshold is divided by 4, i.e. $.0125 = .05/4$.

4.2.3 Multivariate GLM (mGLM)

The multivariate GLM (mGLM) is specified using the design matrices of the 4 univariate models in the MSPM toolbox (Gyger et al., 2021). The mGLM models the multivariate observations as $Y=XB+E$, where $Y_{138 \times 4} = [Y_1, Y_2, Y_3, Y_4]$ is the multi-modal data matrix, each row of Y represents one participant, and each column represents one map; and $X_{138 \times 5} = [X_1, X_2, X_3, X_4, X_5]$ is the design matrix, the first column represents the mean over subjects, the rest of the columns represent mean-centered regressors (age, TIV, gender, scanner) respectively. Thus, B is a 5×4 matrix of regression coefficients; and E is the residual matrix of size 138×4 . B is estimated using an ordinary least-square method, as $\hat{B} = (X^T X)^{-1} X^T Y$. The residual matrix \hat{E} is estimated on a per-voxel basis that allows for a straightforward determination of a unique covariance structure for each voxel. This feature is a significant advantage of mass multivariate approaches when dealing with dependent neuroimaging data. However, it's important to note that in this framework, the assumption of normality for the residuals implies that the covariance

structure is assumed to be the same across different groups or conditions. There is an assumed degree of correlation between the columns of Y, this correlation is expressed by estimation of the variance-covariance matrix $\hat{\Sigma} = \frac{1}{n-k} \hat{E}^T \hat{E}$, where n is the number of subjects and k is number of covariates.

Hypothesis testing

Hypothesis testing in mGLM relies on the contrast $CBL=0$. This extension of the univariate scheme combines standard hypotheses on the rows of matrix B, represented by matrix C, with hypotheses on the columns of B, represented by matrix L. In the context of multivariate ANOVA (MANOVA) models, contrasts of main effects and interactions are formulated by setting $L=I_t$, the $t \times t$ identity matrix, as the dependent variables in multimodal neuroimaging applications are not assumed to be directly proportional. This method is the most suitable for conducting hypothesis testing on multimodal neuroimaging applications.

Test statistics in mGLM

In hypothesis testing using the multivariate GLM, there are four standard test statistics available, which can be constructed based on the calculation of two sums-of-squares and cross-products (SSCP) matrices: Pillai's trace (Pillai, 1955), Wilks' lambda (Wilks, 1932), Hotelling-Lawley trace (Hotelling, 1951), and Roy's largest root (Roy, 1945). For any particular contrast, there is an SSCP matrix associated with the hypothesis.

$$SSCP_{\text{hypo}} = (C\hat{B}L^T)^T (C(X^T X)^{-1} C^T) (C\hat{B}L^T) \quad (1)$$

And an SSCP matrix associated with the residuals.

$$SSCP_{\text{residual}} = L(\hat{E}^T E)L^T \quad (2)$$

These matrices are generalizations of the numerator and denominator sums-of-squares from the univariate GLM hypothesis-testing approach. When L is an identity matrix, the main diagonal of $SSCP_{\text{hypo}}$ contains the sums of squares for the hypothesis in C as

applied to the estimated parameters for each dependent variable separately. And $SSCP_{\text{residual}}$ matrix is an unscaled form of the estimated covariance matrix $\hat{\Sigma}$.

Construction of the test statistics rely on some linear combination of m eigenvalues $(\lambda_1, \dots, \lambda_q)$ of $SSCP_{\text{residual}}^{-1}SSCP_{\text{hyppo}}$. Here, we will only focus on Wilks' lambda test statistics. It quantifies the proportion of variance not accounted for by the hypothesis compared to the total variance in the data.

The Wilks Lambda statistic can be calculated based on the calculated m eigenvalues as $\Lambda = \prod_{i=1}^m \frac{1}{1+\lambda_i}$. This has an approximate F distribution with degrees of freedoms a and b :

$$F(a,b) = \frac{1-\Lambda^{\frac{1}{t}}}{\Lambda^{\frac{1}{t}}} \cdot \frac{b}{a} \quad (3)$$

Where $a=lq$ and $b=rt-2u$.

$$l = \text{rank}(L) \quad (4)$$

$$q = \text{rank}(C) \quad (5)$$

$$u = \frac{a-2}{4} \quad (6)$$

$$r = N - q - \frac{a+1}{2}, \quad N = \text{sample size} \quad (7)$$

$$t = \begin{cases} \sqrt{\frac{l^2 q^2 - 4}{l^2 + q^2 - 5}} & , l^2 + q^2 - 5 > 0 \\ 1 & , l^2 + q^2 - 5 \leq 0 \end{cases} \quad (8)$$

If the minimum value between $l=4$ and $q=1$ is ≤ 2 , the distribution is exactly F.

Age related microstructural changes- mGLM

The hypothesis $H_0: \text{CBL} = 0$ can be tested to assess the different potential co-occurrence of change between the modalities. To test the joint effect on the 4 quantitative maps in a specific tissue type, $L_{4 \times 4}$ is

defined as an identity matrix corresponding to the number of dependent variables (quantitative maps). As explained before, each column of L will perform a univariate analysis on each column of B . Here, C was defined as $[0 \ 1 \ 0 \ 0 \ 0]$ to only see the correlation between age and maps. In this case, Λ has an exact F distribution with $a = 4$ and $b = 130$ degrees of freedom.

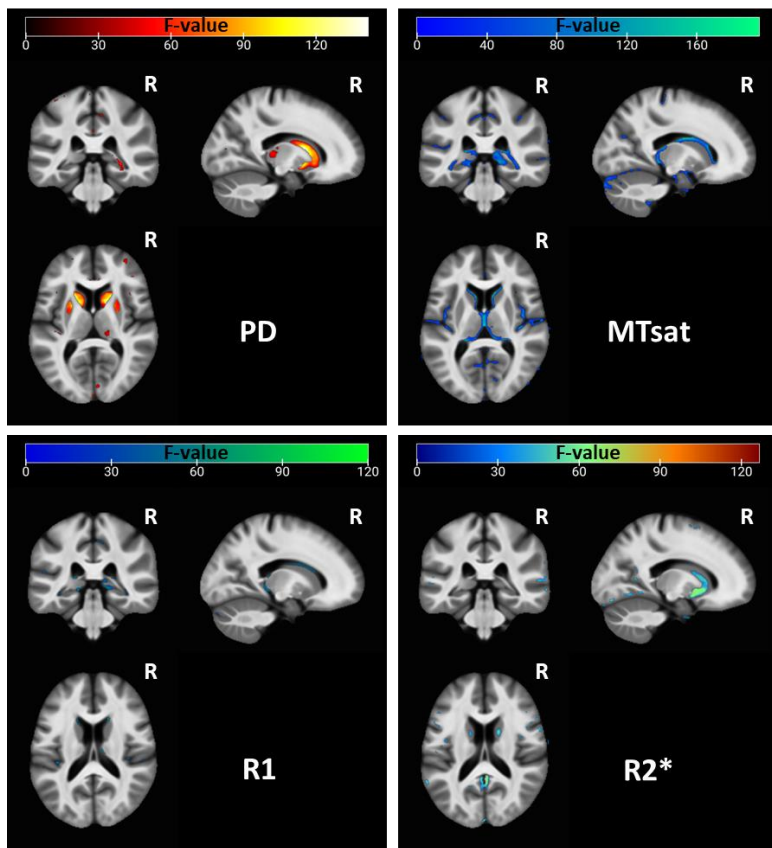


Figure 4-1. Statistical parametric maps of uGLMs in GM; showing all the voxels with significant correlation with age, as detected by uGLMs for PD, MTsat, R1, and R2* maps. The F-tests were thresholded at $p < 0.0125$ FWER corrected at voxel-level. The critical F-value cutoff for these analyses was 6.412. The SPMs were overlaid on the mean MTsat map for the cohort in the MNI space. Abbreviation: GLM, general linear model; uGLM, univariate GLM; GM, gray matter; FWER, family-wise error rate; SPM, statistical parametric map.

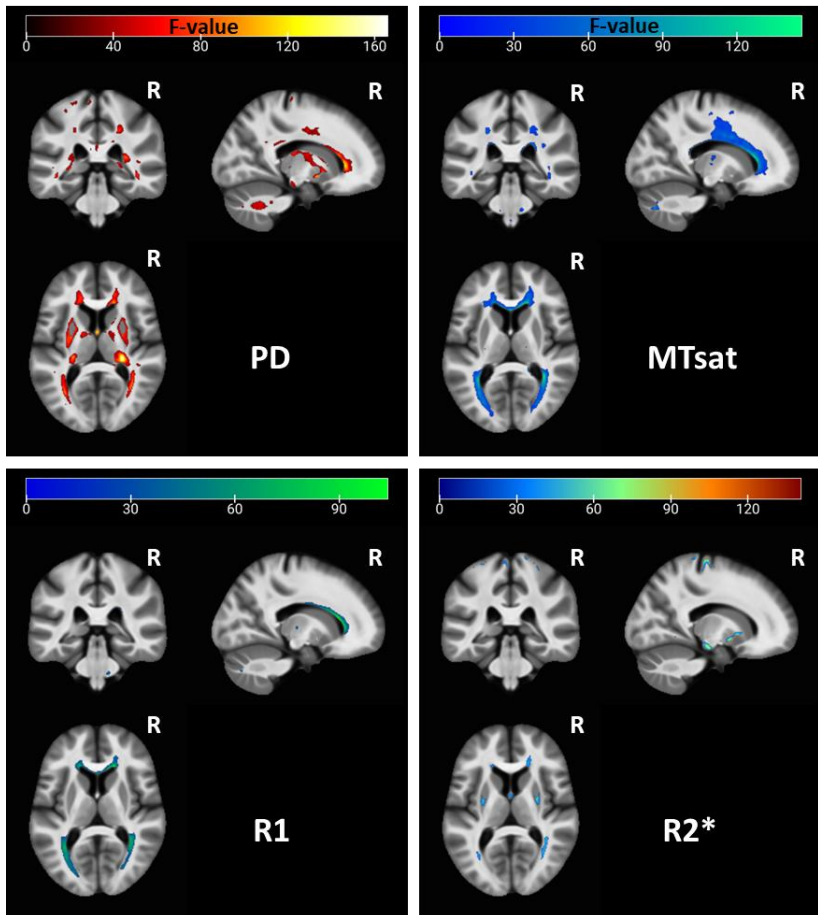


Figure 4-2. Statistical parametric maps of uGLMs in WM; showing all the voxels with significant correlation with age, as detected by uGLMs for PD, MTsat, R1, and R2* maps. The F-tests were thresholded at $p < 0.0125$ FWER corrected at voxel-level. The critical F-value cutoff for these analyses was 6.412. The SPMs were overlaid on the mean MTsat map for the cohort in the MNI space. Abbreviation: GLM, general linear model, uGLM, univariate GLM, mGLM, multivariate GLM, WM, white matter, FWER, family-wise error rate, SPM, statistical parametric map.

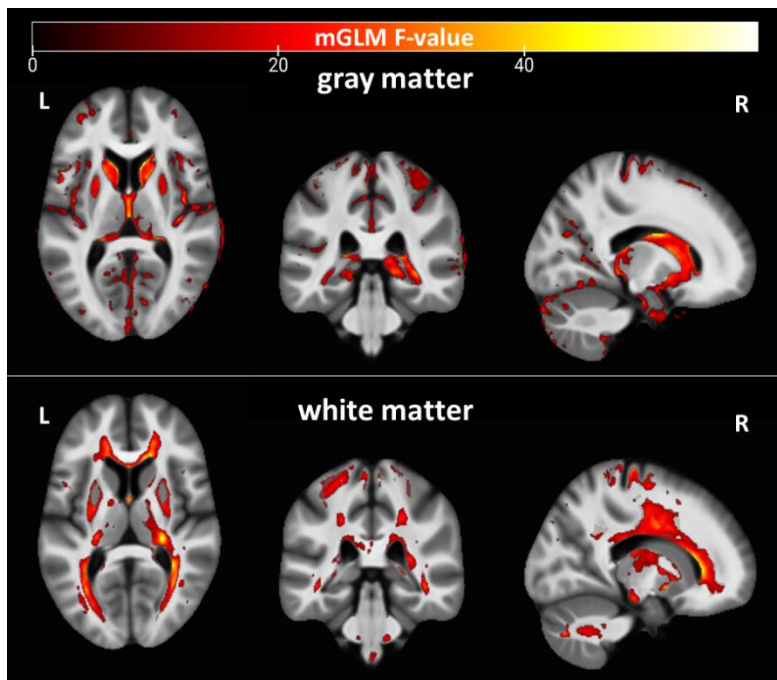


Figure 4-3. Statistical parametric maps of mGLMs in GM and WM; showing all the voxels with significant correlation with age, as detected by the multivariate model. The F-tests were thresholded at $p < 0.05$ FWER corrected at voxel-level. The critical F-value cutoff for these analyses was 2.730. The SPMs were overlaid on the mean MTsat map for the cohort in the MNI space. Abbreviation: GLM, general linear model; mGLM, multivariate GLM; WM, white matter, FWER, family-wise error rate, SPM, statistical parametric map.

Canonical Correlation Analysis

Canonical vectors are calculated under the assumption that matrix L involves multiple dependent variables ($l > 1$), to extract the contribution of each dependent variable to the test statistics Λ . This contribution corresponds to the eigen vectors of the eigen decomposition of $SSCP_{residuals}^{-1} SSCP_{hippo}$ (Tabachnick and Fidell, 2007).

ROI analyses

The age-related parameter differences in selected ROIs will be further described. ROIs were defined according to the “automated

anatomical labeling” (AAL3) atlas (Rolls et al., 2020) and selected based on identified significant areas in our mGLM results and in (Callaghan et al., 2014). For each participant and quantitative map, the measure from each voxel in an ROI was extracted. The regressors of no interest (gender, TIV and scanner) were regressed out. Another regression was applied on the adjusted median values and age (our regressor of interest). For each selected ROI, the relation between age and median value across subjects will be examined.

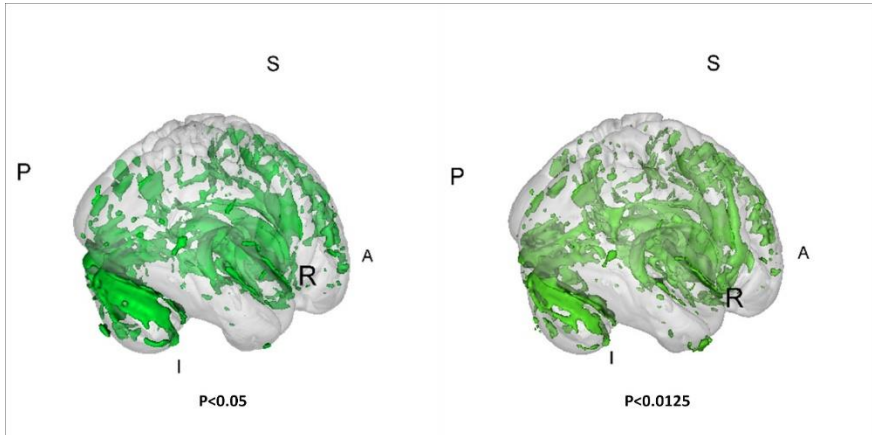


Figure 4-4. The union of all uGLM statistical parametric masks in GM. On the left side, the F-tests for the uGLMs were thresholded at $p < 0.05$ FWER corrected at voxel-level. On the right side, the F-tests for the uGLMs were thresholded at $P < 0.0125$ after correction for FWER at voxel-level. The masks were overlaid on the mean MTsat map for the cohort in the MNI space. Abbreviation: GLM, general linear model; uGLM, univariate GLM; GM, gray matter; FWER, family-wise error rate.

4.3 Results

The analyses were conducted on both gray matter (GM) and white matter (WM). Consequently, explicit masks for GM and WM were applied to each analysis. Since each parametric map has its specific unit, such as Hertz for $R2^*$ images and p.u. for MTsat maps, their values cannot be directly compared. All statistical analyses were performed on standardized z-transformed data. The multivariate statistical analyses

were conducted at a corrected threshold of $p < .05$ FWER. The univariate analyses were thresholded twice: once at $p < .05$ to replicate the results from a previously published paper (Callaghan et al., 2014), and once at $p < .0125$ to account for the effect of multiple comparisons.

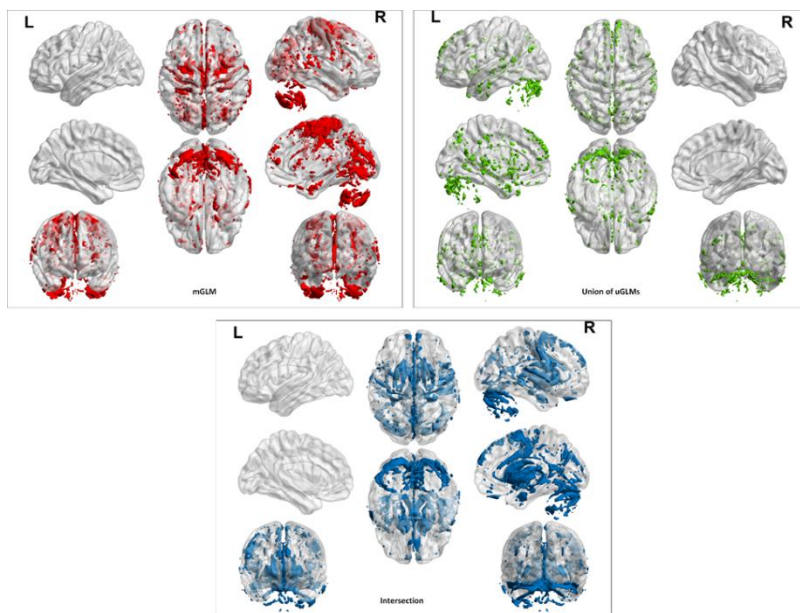


Figure 4-5. mGLM vs multiple uGLMs in GM. The right upper panel represents the union of all uGLM statistical parametric masks (in green). The left upper panel shows the mGLM results (in red), and the intersection between both univariate and multivariate (in blue) is presented in the lower panel. The F-tests for the uGLMs were thresholded at $P < 0.0125$ after correction for FWER at voxel-level. The F-test for the mGLM was thresholded at $P < 0.05$ FWER corrected at voxel-level. The masks were overlaid on MNI152 template image in BrainNet. Abbreviation: GLM, general linear model; uGLM, univariate GLM; mGLM, multivariate GLM; GM, gray matter; FWER, family-wise error rate.

4.3.1 uGLM vs mGLM: Voxel level analyses

The individual GM and WM analyses on $R2^*$, PD, MTsat, and $R1$ maps at a corrected threshold of $p < .05$ FWER, concur with those in (Callaghan et al., 2014). The statistical parametric maps for age-related changes in the microstructure of the brain in GM and WM (at a corrected threshold

of $p < .05$ FWER) are depicted in **Figure 7-1** and **Figure 7-2** of the Appendix-C. The statistical parametric maps for the same analyses at a corrected threshold of $p < .0125$ FWER) are presented in **Figure 4-1** and **Figure 4-2** for GM and WM.

Table 4-1. Summary statistics for significant voxels in uGLMs and mGLM. “United” rows show the union of significant voxels in SPMs for all modalities. Univariate GLMs were thresholded at $p < .05$ FWER corrected per tissue class (GM or WM). Abbreviation: GLM, general linear model; uGLM, univariate GLM; mGLM, multivariate GLM; GM, gray matter; WM, white matter.

		Map name	#clusters	Cluster size	#voxels
GM	uGLMs	MTsat	284	1-42251	62334
		PD	271	1-7001	28563
		R1	181	1-1336	9078
		R2*	329	1-6416	44262
		United	666	1-82030	115957
	mGLM		564	1-130197	154098
WM	uGLMs	MTsat	58	1-67245	70285
		PD	78	1-7292	43051
		R1	36	1-11290	18301
		R2*	115	1-3789	18031
		United	191	1-84201	105068
	mGLM		188	1-82807	102390

Voxel-wise mGLM results presented in **Figure 4-3**, indicate bidirectional correlation between all modalities and age at $p < .05$ FWER corrected. The correlation is observed bilaterally in caudate nucleus, putamen, insula, cerebellum, lingual gyri, hippocampus, and olfactory bulb.

Table 4-1 provides a statistical summary of the F-tests results (thresholded at voxel-level $p < .05$ FWER) from both the univariate general linear models (uGLMs) and mGLM for all maps within the two

tissue classes. Additionally, **Table 4-2** presents the statistical summary of the uGLM F-tests results with Bonferroni-adjusted threshold. Comparing the spatial extent of significant results between uGLMs and mGLM in Tables 1 and 2 reveals that the multivariate model identifies a larger number of significant voxels compared to the union of all uGLMs with both family-wise error (FWE) and Bonferroni corrections.

Table 4-2. Summary statistics for significant voxels in uGLMs and mGLM. “United” rows show the union of significant voxels in SPMs for all modalities. Univariate GLMs were thresholded at $p < 0.0125 = .05/4$ FWER corrected, to account for the multiplicity of maps tested (4) per tissue class (GM or WM). The mGLM was thresholded at $p < 0.05$ FWER corrected.

		Map name	#clusters	Cluster size	#voxels
GM	uGLMs	MTsat	265	1-16445	50041
		PD	212	1-6671	22168
		R1	142	1-670	6276
		R2*	256	1-5919	31993
		United	570	1-54926	90323
	mGLM		564	1-130197	154098
WM	uGLMs	MTsat	45	1-52838	35281
		PD	73	6378	54894
		R1	27	1-8640	14344
		R2*	101	1-3223	13518
		United	163	1-56506	83187
	mGLM		188	1-82807	102390

To illustrate the voxels affected by age at a threshold of $p < .0125$ and $p < .05$ in at least one of the (semi-)quantitative maps, the union of all statistical parametric maps derived from uGLMs in GM was binarized and depicted in **Figure 4-4**.

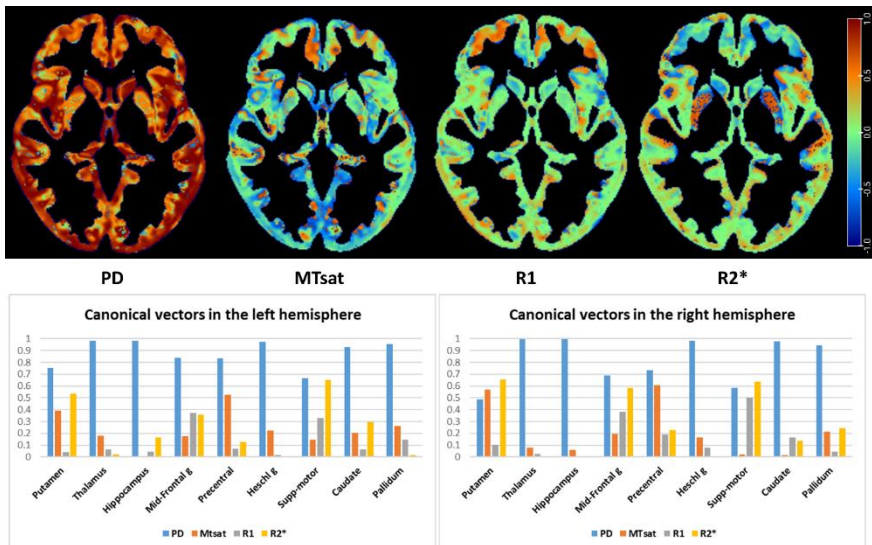


Figure 4-6. Canonical vectors for different modalities from the mGLM model, representing the contribution of each modality in each voxel. The color bar shows arbitrary values. The vectors correspond to the peak voxels at the selected ROIs. Detailed vector sizes are reported in **Table 7-5** of Appendix-C. Abbreviation: mGLM, multivariate general linear model; ROI, region of interest.

In **Figure 4-5**, the differentiates of the binarized union of all statistical parametric maps derived from the uGLMs with $p < .0125$ FWER in GM and the binarized statistical parametric map for mGLM (with $p < .05$ FWER) to visualize the voxels that can be uniquely detected either by the multivariate model (shown in red) or by at least one of the univariate models (shown in green).

Among the models used, only the mGLM detected an age effect in certain regions, including portions of the superior medial frontal lobe, supplementary motor area, paracentral lobule, middle and anterior cingulum, parts of the precuneus, cuneus, calcarine, lingual gyrus, cerebellum, hippocampus, and para hippocampus bilaterally, as well as the left fusiform gyrus. Schematic representations of these regions can be found in **Figure 4-5**, highlighted in red.

4.3.2 ROI analyses

Canonical vectors

To further investigate the impact of aging on myelination, iron content, and water concentration in various brain regions, quantitative MR parameters were selected from bilateral regions including the putamen, thalamus, hippocampus, middle frontal gyrus, precentral gyrus, Heschl gyrus, supplementary motor area, caudate, and pallidum (Callaghan et al., 2014; Darnai et al., 2017; Tian et al., 2022; Wang et al., 2020).

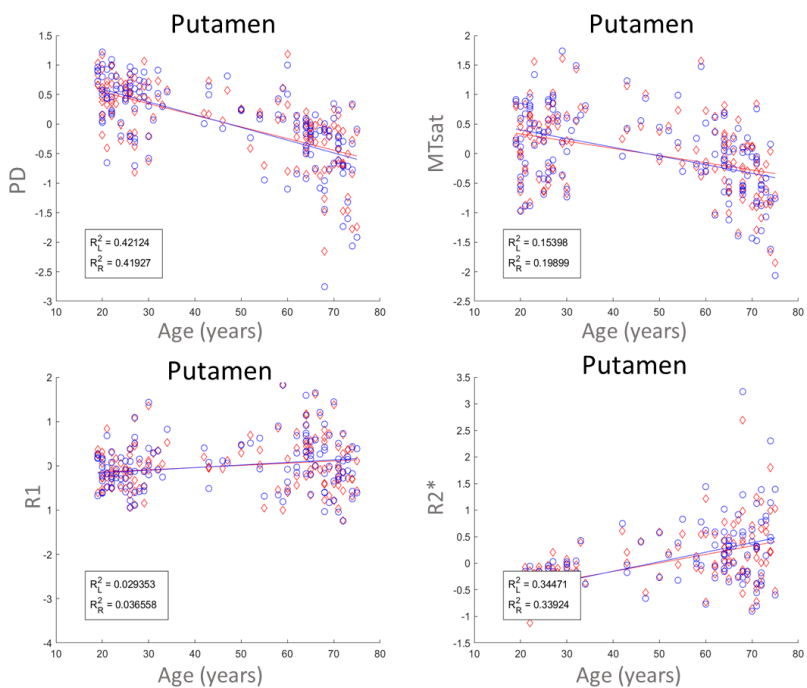


Figure 4-7. Median voxel values in Putamen. The median values within the right putamen are illustrated with blue circles and the median values within the left putamen are illustrated with red diamonds. The blue and red lines depict the linear model fit to the right and left values respectively. These data are shown for illustration purposes only and were not used for any additional analyses.

For each region of interest (ROI), the canonical vectors corresponding to each quantitative map within the gray matter (GM) were estimated, as shown in the upper panel of **Figure 4-6**. It is important to note that the canonical vectors displayed in the lower part of **Figure 4-6** represent the contribution of each map in the peak voxel of the respective ROI and do not represent the contribution factor for the entire ROI. Additionally, the direction of these vectors cannot be interpreted as they are derived from F-tests, therefore we have displayed the absolute weights. For example, in the right and left hippocampus, PD signals exhibit the highest contribution while in the right putamen, MTsat signal contributes the most as indicated by the canonical vectors.

Median values

The median values of normalized, smoothed, and z-transformed $R2^*$, MTsat, PD, and R1 maps within the Putamen and Hippocampus ROIs with respect to age are illustrated in **Figure 4-7** and **Figure 4-8**. Region-based regression analysis for the adjusted medians and age, within each cluster are along with the respective linear age dependence observed from the uGLM analyses in the selected regions. We observe a bilateral decrease in the normalized MTsat and PD values in GM with respect to aging. While the PD and MTsat median values decrease with age in all regions of the brain, median $R2^*$ values show an increase in most regions of the brain except for the thalamus where there is a significant negative age-related variation. These results are consistent with previously published results for the mean values in thalamus for $R2^*$ (Taubert et al., 2020). R1 median signals show a weak positive correlation with age. The alteration in median values as a function of age concurs with the magnitude of the associated canonical vector. The bivariate correlation analysis indicates strongest correlations for PD in most selected regions, see **Table 4-3**.

4.4 Discussion

The multivariate approach used in this study to investigate age-related changes in the microstructural tissue properties of the brain, incorporating image-derived quantitative maps for myelin, iron, and free

water content, enables the identification of regions that are influenced by the simultaneous occurrence of various parameter differences.

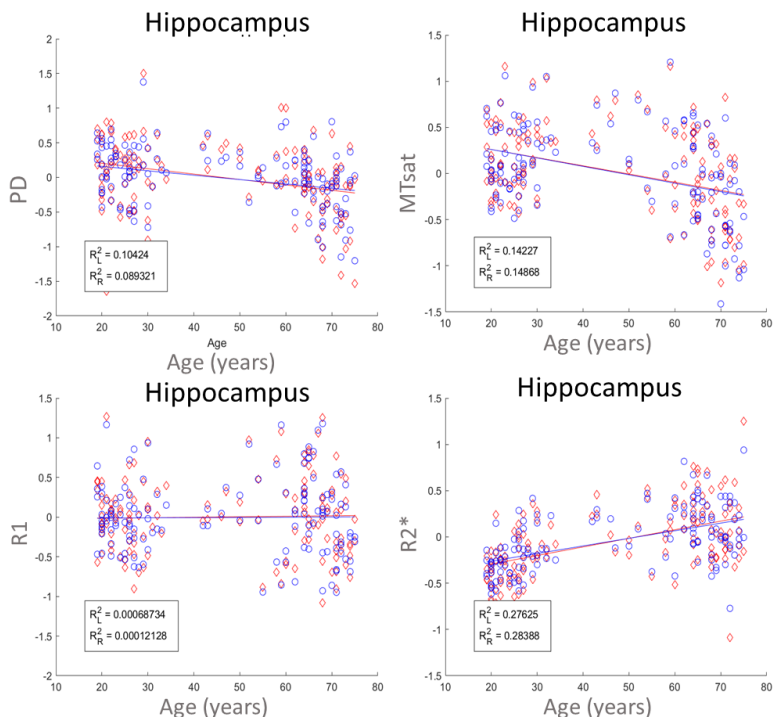


Figure 4-8. Median voxel values in Hippocampus. The median values within the right putamen are illustrated with blue circles and the median values within the left putamen are illustrated with red diamonds. The blue and red lines depict the linear model fit to the right and left values respectively. These data are shown for illustration purposes only and were not used for any additional analyses.

By considering multiple quantitative maps simultaneously, the multivariate approach provides a comprehensive understanding of how these different tissue properties interact and contribute to age-related differences. This method enables the identification of specific brain regions that exhibit coordinated alterations in myelin, iron, and water content, offering insights into the underlying mechanisms of aging.

Table 4-3. Pearson Partial Correlations with age on the median voxel values bilaterally within different regions of interest.

	Pearson's r	p-value	Effect size (Fisher's z)		Pearson's r	p-value	Effect size (Fisher's z)
Caudate				Pallidum			
MTsat	-0.44***	< .001	-0.47	MTsat	-0.10	0.253	-0.10
PD	-0.63***	< .001	-0.75	PD	-0.70***	< .001	-0.86
R1	0.09	0.289	0.09	R1	0.44***	< .001	0.47
R2s	0.48***	< .001	0.52	R2s	0.66***	< .001	0.80
Cerebellum				Precentral Gyrus			
MTsat	-0.55***	< .001	-0.62	MTsat	-0.34***	< .001	-0.358
PD	-0.26**	0.002	-0.27	PD	-0.44***	< .001	-0.472
R1	-0.11	0.198	-0.11	R1	-0.02	0.852	-0.016
R2s	0.38***	< .001	0.41	R2s	0.50***	< .001	0.545
Heschl Gyrus				Putamen			
MTsat	-0.51***	< .001	-0.56	MTsat	-0.23**	0.007	-0.237
PD	-0.18*	0.037	-0.18	PD	-0.61***	< .001	-0.709
R1	-0.21*	0.014	-0.21	R1	0.30***	< .001	0.307
R2s	0.21*	0.012	0.22	R2s	0.62***	< .001	0.719
Middle Frontal Gyrus				Superior motor cortex			
MTsat	-0.13	0.129	-0.13	MTsat	-0.13	0.139	-0.129
PD	-0.45***	< .001	-0.48	PD	-0.45***	< .001	-0.480
R1	0.07	0.423	0.070	R1	0.05	0.560	0.051
R2s	0.437***	< .001	0.47	R2s	0.59***	< .001	0.68
Hippocampus				Thalamus			
MTsat	-0.131	0.130	-0.13	MTsat	-0.56***	< .001	-0.64
PD	-0.282***	< .001	-0.29	PD	-0.24**	0.006	-0.24
R1	0.200*	0.020	0.20	R1	-0.35***	< .001	-0.37
R2s	0.316***	< .001	0.33	R2s	-0.20*	0.022	-0.20

Note. Conditioned on variables: Gender, TIV, TRIO (scanner). * p < .05, ** p < .01, *** p < .001

The observed differences in the quantitative MR parameters align with findings from *ex vivo* histologic studies and demonstrate a high specificity for tissue properties, including myelin content, iron content, and free water content.

Using voxel-wise analysis with the multivariate GLM (mGLM), a bidirectional correlation between age and all the examined modalities was observed bilaterally in various brain regions. These regions encompassed the caudate nucleus, putamen, insula, cerebellum, lingual gyri, hippocampus, and olfactory bulb. Importantly, the multivariate approach demonstrated advantages over univariate analyses that focus on individual tissue parameters separately.

While examining individual tissue properties in isolation may provide insights into specific aspects of brain aging, the multivariate model revealed large clusters in the brain that could not be detected by analyzing each property individually. This indicates that the combined examination of multiple tissue properties enables the detection of additional regions associated with aging despite the presence of contrary changes in different properties. As observed in **Table 4-2**, mGLM outperformed the individual univariate GLMs (uGLMs) by detecting a larger number of significant voxels within clusters that cover the supplementary motor area, frontal cortex, hippocampus, amygdala, occipital cortex, and cerebellum bilaterally. This finding suggests that mGLM is a more effective/sensitive technique for detecting age-related differences in the brain.

In this study, the application of a multivariate model such as MANOVA proves advantageous due to the well-established correlations among brain tissue characteristics and the interrelated nature of quantitative map values. By accounting for this inherent correlation, MANOVA effectively reduces potential biases in the results that could arise from using multiple ANOVAs. MANOVA's ability to consider the complex relationships between multiple variables allows it to detect effects that might be smaller than those detectable by ANOVA, providing a more comprehensive understanding of the data.

Additionally, independent covariates can affect the relationship between the brain microstructure characteristics rather than influencing only a single variable; such patterns cannot be detected by the univariate models. Moreover, MANOVA offers a convenient means to manage the family-wise error rate when simultaneously analyzing

multiple dependent variables, effectively reducing type-1 errors. In this study, where four different variables were examined concurrently, better results were achieved under the same p-value threshold compared to multiple univariate analyses on the same GM and WM maps. This underscores the robustness and appropriateness of a multivariate approach for understanding the intricate relationships within the dataset. Here, we utilized Bonferroni threshold for combining the p-values to build up the same power for univariate and multivariate techniques. However, there are other methods for combining p-values for detection of partial association such as Fisher and weighted Fisher methods, which are more relevant in case of many comparison (Yoon et al., 2021).

The nonlinear relationship between MTsat values and age, as visible in **Figure 4-7** and **Figure 4-8**, could be explained by the fact that myelination is not limited to early development, but can also occur throughout adulthood, with the pattern of myelination depending on the hierarchy of connections between different brain regions (Peters, 2002; Snaidero and Simons, 2014; Timmler and Simons, 2019). Potential nonlinear age dependency is also seen in the $R2^*$ profile in some regions such as amygdala and putamen (**Figure 4-7**) which could be due to slower accumulation of iron in these regions. (Hagiwara et al., 2021) showed the nonlinear behavior of different brain tissue properties. However, within the scope of this study, our examination was limited to linear age-related variations, as the original analysis of these data only looked at the linear effects.

The canonical vectors shown in **Figure 4-6**, indicate the contribution of each modality in the multivariate model. Of note that the canonical vectors can only highlight the contribution by their size and cannot inform us about the direction.

The ROI-based partial Pierson's correlations, presented in **Table 4-3**, are evidence of stronger correlations between the GM PD maps and age, which concur with the canonical weights regarding the contribution of PD maps within the GM.

4.4.1 Limitations and conclusion

It is important to note that MANOVA differs from multiple ANOVA analyses, as it does not focus on the signal-to-noise ratio of independent variable effects on each dependent variable individually. Instead, it tests for effects of interest on a combination of outcome variables. For an assessment of the former, a return to univariate analyses is necessary.

Aging involves not only microstructural changes in the brain but also macrostructural and functional alterations, such as changes in GM and WM volume and cognitive behavior changes. Therefore, there remains a need to investigate aging by considering different combinations of changes together. Furthermore, longitudinal studies are required to elucidate how normal aging deviates from pathological aging within a multivariate system.

In summary, the findings of this study underscore the importance of employing advanced statistical models like the mGLM to detect subtle microstructural changes associated with aging. The results highlight the significance of ROI analyses in identifying specific brain regions affected by aging and their relationships with different modalities. This study provides valuable insights into the neural mechanisms underlying age-related differences in brain structure, which may have implications for developing effective interventions to slow down or prevent cognitive decline in older adults.

Chapter summary

This study utilized multivariate ANOVA analysis to investigate age-related microstructural changes in the brain tissues driven primarily by myelin, iron, and water content. Voxel-wise analyses were performed on gray matter (GM) and white matter (WM), in addition to region of interest (ROI) analyses. The multivariate approach identified brain regions showing coordinated alterations in multiple tissue properties and demonstrated bidirectional correlations between age and all examined modalities in various brain regions, including the caudate nucleus, putamen, insula, cerebellum, lingual gyri, hippocampus, and olfactory bulb. The multivariate model was more sensitive than univariate analyses as evidenced by detecting a larger number of significant voxels within clusters in the supplementary motor area, frontal cortex, hippocampus, amygdala, occipital cortex, and cerebellum bilaterally. The examination of normalized, smoothed, and z-transformed maps within the ROIs revealed age-dependent differences in myelin, iron, and water content. These findings contribute to our understanding of age-related brain differences and provide insights into the underlying mechanisms of aging. The study highlights the need for multivariate analysis to identify subtle microstructural changes linked to aging, potentially guiding interventions to alleviate cognitive decline in older adults.

Chapter 5

Relationships between Cognition and Brain Tissue Properties: A Longitudinal Study on Healthy Older Adults

This chapter is based on our article under preparation:

*Moallemian, S., Chylinski, D., Van Egroo, M., Narbutas, J., Salmon, E., Maquet, P., Collette, F., Vandewalle, G., Phillips, C., Bastin, C., “**Relationships between Cognition and Brain Tissue Properties: A Longitudinal Study in Healthy Older Adults**”, under preparation.*

Preface

The healthcare landscape has witnessed remarkable advancements, ushering in an era where life expectancy has exceeded 60 years in developed countries (Beard et al., 2016). Age-related cognitive decline, a complex phenomenon impacting various domains such as sensory perception, memory, attention, executive function, language, reasoning, and spatial navigation (Yang et al., 2023), demands careful unraveling for its paramount significance in disease prevention and the enhancement of life quality.

Aging casts a pervasive influence on sensory and perception functions, with olfactory impairment emerging as a prevalent sensory challenge, correlated with accelerated decline across various cognitive domains (Attems et al., 2015; Yang et al., 2023). Episodic memory, significantly impacted by aging and Alzheimer's disease, manifests through altered efficiency in information binding and encoding (Bäckman et al., 2001), with structural and functional changes observed in critical brain regions such as hippocampus and medial temporal area, and cerebellum (Fließbach et al., 2007; Hayes et al., 2004; Jacobs et al., 2018; Rugg and Vilberg, 2013).

Studies have illuminated associations between cognition and brain atrophy in normal aging (Good et al., 2001; Pini et al., 2016). While conventional studies lean heavily on functional and structural MRI, the emergence of qMRI techniques opens a gateway to (semi)quantitative measures, enabling a microscopic lens on brain microstructure (Helms et al., 2010, 2009; Weiskopf et al., 2011).

In this chapter, we attempt to find associations between cognition and brain micro- and macro-structure in healthy older adults, leveraging the power of qMRI and multivariate modeling. Our hypotheses are grounded in a wealth of prior research linking aging and the brain's structural intricacies (Callaghan et al., 2014; Draganski et al., 2011; Moallemian et al., 2023a, 2023b; Taubert et al., 2020). The focus of our inquiry lies in unraveling the connections between myelin content, iron levels, and cognitive performance.

5.1 Introduction

Thanks to the development in the healthcare system, today, the life expectancy has risen to more than 60 years in developed countries (Beard et al., 2016). Throughout the course of human life, advancing age typically brings about cognitive alterations, sometimes leading to a decrease in functional capacity (Yang et al., 2023). Age-related cognitive decline is heterogeneous in the different cognitive domains including sensory perception, memory, attention, executive function, language, reasoning, and the capacity of navigation in space, with the most frequent changes affecting memory and executive functioning (Yang et al., 2023). Understanding the mechanism of cognitive aging is of great value for disease prevention, improving the quality of life, and ultimately achieving healthy aging.

In terms of brain anatomy, normal aging is associated with structural changes, on account of extensive gray matter (GM) and white matter (WM) atrophy (Callaghan et al., 2014; Good et al., 2001; Pini et al., 2016; Taubert et al., 2020). The GM atrophy is reported throughout the cortex with greater involvement of the frontal regions and the putamen (Callaghan et al., 2014). In more recent studies, GM loss was also observed in frontal, parietal, temporal, insular, and occipital lobes, and cerebellum along with hippocampus, amygdala, basal ganglia, and thalamus (Ramanoël et al., 2018; Taubert et al., 2020). Age-related WM volume loss was observed in bilateral frontal, temporal, and parietal regions, additional to the splenium and cerebellum (Taubert et al., 2020).

Furthermore, numerous neuroimaging studies have investigated the association between cognition in aging and brain changes via functional MRI (fMRI) techniques, or GM and WM atrophy (Attems et al., 2015; Dintica et al., 2019; Yang et al., 2023).

Aging exerts a global effect on sensory and perception functions in elderly individuals. Olfactory impairment, a common sensory impairment (Attems et al., 2015), is correlated to faster decline in almost all cognitive domains including visuospatial ability, perceptual speed,

semantic memory, and especially the episodic memory domain (Yang et al., 2023). It is associated with lower volumes of fusiform and middle temporal cortices, which include the entorhinal cortex and hippocampus as measured with structural MRI studies (Dintica et al., 2019).

Episodic memory is one of the most severely affected cognitive domain in aging and Alzheimer's disease (Bäckman et al., 2001). This is due to a decreased efficiency of binding different pieces of information together at encoding, as well as to a difficulty in initiating strategies to efficiently encode and retrieve new information (Fandakova et al., 2014; Naveh-Benjamin et al., 2004). Episodic memory difficulties in aging have been related to changes in the structure and function of a network of brain regions including medial temporal lobe, prefrontal, and posterior midline regions. In particular, age-related memory decline is associated with changes to the hippocampus and the prefrontal cortex. The other cognitive domain which is most affected by healthy aging is executive functioning such as switching, inhibition and strategic search abilities, as well as working memory processes (Bryan and Luszcz, 2000; Ramanoël et al., 2018; Troyer et al., 1997). GM atrophy was found related to a decline in executive function within the frontal lobe (Good et al., 2001; Ramanoël et al., 2018).

While a majority of studies has used functional and structural MRI in their investigation of cognition and aging, the development in quantitative magnetic resonance imaging (qMRI) techniques has provided the opportunity to calculate (semi)quantitative measures such as magnetization transfer saturation (MTsat) map, proportional to myelin, effective transverse rate ($R2^*$) proportional to iron level, and proton density (PD) map (Helms et al., 2010, 2009; Weiskopf et al., 2011). These measures allow to approach microstructural changes in the brain. (Acosta-Cabronero et al., 2016) identified age-related changes in several deep-brain nuclei and across motor, premotor, posterior insular, superior prefrontal, and cerebellar cortices, using quantitative susceptibility maps (QSM) - a quantitative MR technique that assesses the magnetic properties of cerebral iron *in vivo*. (L. Chen et al., 2021) identified a negative correlation between iron content in the hippocampus and a global cognitive composite score. Furthermore, the

iron level in the hippocampus and putamen is negatively associated with executive function (L. Chen et al., 2021; Kalpouzos et al., 2021).

QMRI maps derived from the multiparametric maps (MPM) protocol (Weiskopf et al., 2013) have been used in some studies (Callaghan et al., 2014; Draganski et al., 2011; Kalpouzos et al., 2017; Taubert et al., 2020). All their findings point to the association between demyelination and age within the GM with higher age-related demyelination in the somatosensory and motor cortices, and thalamus (Callaghan et al., 2014; Draganski et al., 2011; Taubert et al., 2020). Within the WM, there is a decrease in MTsat signal as a function of age in frontal and parietal regions (Callaghan et al., 2014; Draganski et al., 2011). Proton density was found to decrease with aging in the frontal, parietal, temporal, insular, occipital, and cerebellar lobes (Taubert et al., 2020). Iron content within the GM increased in pallidum, putamen, and caudate bilaterally (Callaghan et al., 2014; Taubert et al., 2020). Also, a decrease in iron level was detected bilaterally in the somatosensory and motor cortices (Taubert et al., 2020). Finally, a recent study investigated associations between white and gray matter microstructural changes, using neurite orientation dispersion and density imaging (NODDI), a diffusion MR imaging technique used in clinics to quantify the packing density of axons or dendrites. In mild cognitive impairment (MCI) and Alzheimer's disease (AD), this study showed that the cognitive performance of patients was significantly associated with the neurite density index (NDI) (Zhong et al., 2023).

In this study, we aim to investigate the association between cognition and brain micro- and macro-structure, measured from the MPM quantitative maps, in healthy older adults. We assessed whether cognitive performance at one time point and the decline in cognition over a 2-year follow-up are associated with brain characteristics such as gray and white matter volume, iron level, and myelin content. We build our hypotheses on previous findings linking aging and micro- and macro-structure of the brain (Callaghan et al., 2014; Draganski et al., 2011; Moallemian et al., 2023b; Taubert et al., 2020). Therefore, we hypothesize that lower myelin content is associated with worse cognitive performance, while more iron content has a negative

association with cognition. We will also investigate if we can characterize the association between PD and R1 maps and cognition. Furthermore, brain characteristics are related to each other, so that myelin and iron can co-occur and lead to neuronal loss, captured by gray matter volume loss (Bartzokis, 2011). Therefore, we hypothesized that investigating the association between cognition and all brain properties in a multivariate manner would lead to specific brain regions in which several changes are related to cognition. This would represent the most sensitive regions to cognitive decline due to aging.

5.2 Methods

5.2.1 Participants

The study included 101 healthy middle-aged to old participants (age range [50 69] y.o., 32 males). All participants underwent a multimodal cross-sectional study on the relationships between Alzheimer's disease biomarkers, sleep-related processes, lifestyle factors and cognitive aging (Chylinski et al., 2022; Narbutas et al., 2019; Van Egroo et al., 2019). The exclusion criteria consisted of 1. taking medications that affect the central nervous system, 2. psychiatric or/and neurological disorders, 3. sleep apnea/hypopnea index $\geq 15/h$, assessed during an in-lab night of sleep under polysomnography, 4. body mass index < 18 and > 30 kg/m², 5. smoking, illicit drug consumption, excessive consumption of caffeine (> 4 cups/day) or alcohol (> 14 units/week), 6. Diabetes, 7. shift-work. All participants showed normal performance on the Mattis Dementia Rating Scale [*i.e.* score > 130]. The study described in this research received ethical approval from the Ethics Committee of the Faculty of Medicine at the University of Liège, Belgium. Prior to their participation, all subjects provided their informed consent and were given financial compensation.

The participants were asked to return to the lab for a follow-up cognitive assessment after two years. Only 67 participants agreed to perform a second set of cognitive assessment (age range [52 71] y.o., 22 males). A summary of the participants' characteristics at the baseline and after two years is presented in **Table 5-1**.

Table 5-1. Demographics of the participants. The values are calculated from 101 participants at the baseline. We report the z-scores for attention, executive (function), memory, and PACC5 at the baseline. The scores reported at the follow up for attention, executive (function), memory, and PACC5 are the rate of change.

	Mean	sd	Min	Max	Mean	sd	Min	Max
	Baseline (n=101)				Follow up (n=67) ^b			
Age (years)	59.44	5.29	50	69	61.86	5.36	52	71
bmi ^a	24.62	2.89	18	30	24.61	2.68	19	30
Edu(years)	15.22	3.01	9	25	14.91	3.24	9	25
attention	0.00	0.99	-2.37	2.06	-0.05	1.58	-4.37	3.70
executive	0.00	0.99	-2.14	2.76	0.00	2.29	-8.33	4.46
memory	0.00	0.99	-3.88	1.66	0.06	1.73	-6.78	3.08
PACC5	0.00	2.91	-7.94	8.35	0.05	2.30	-5.04	7.98

Note. ^abmi, body mass index; ^b the reported values correspond to the rate of change in scores for attention, executive, memory and PACC5

5.2.2 Imaging Data

Collected data were anonymized and organized according to the Brain Imaging Data Structure (BIDS) (Gorgolewski et al., 2016) and its extensions for PET and quantitative MRI (qMRI) data (Karakuzu et al., 2022), the latter using BIDSme, an in-lab developed toolbox, (<https://github.com/CyclotronResearchCentre/bidsme>), and the former with custom MATLAB scripts. All information needed for subsequent analysis was incorporated into the dataset. Data is available from the corresponding authors upon reasonable request.

5.2.3 Quantitative MRI

MRI data was acquired on a 3T whole-body MRI-scanner (MAGNETOM Prisma, Siemens Medical Solution, Erlangen, Germany) using a standard 64-channel head receiving coil. The whole-brain MRI acquisitions included a multiparameter mapping protocol (MPM) (Weiskopf et al., 2013), enabling the estimation of (semi)quantitative maps for various parameters: magnetization transfer saturation (MTsat) associated with myelin, proton density (PD) linked to water content,

transverse relaxation ($R2^*$) related to iron, and effective longitudinal relaxation ($R1$) linked to iron, myelin contents (Stüber et al., 2014).

The MPM protocol consisted of 3 co-localized 3D multi-echo “fast low angle shot” (FLASH) acquisitions with 1 mm isotropic resolution and 2 additional calibration sequences to correct for inhomogeneities in the RF transmit field (Lutti et al., 2010). The FLASH datasets were acquired with predominantly PD, T1 and MT weighting determined by the repetition time ($TR = 24.5$ ms) and flip angle ($FA = 6^\circ$ for PD & MT, 21° for T1), referred to in the following as PDw, T1w and MTw echoes. MTw contrast was obtained using an additional off-resonance Gaussian-shaped RF pulse with 4 ms duration and 220 nominal flip angle, 2 kHz off-resonance before nonselective excitation. A high readout bandwidth of 320 Hz/pixel was used to minimize off-resonance and chemical shift artifacts (Helms and Dechent, 2009). Volumes were acquired in 176 sagittal slices using a 256x224 voxel matrix. GRAPPA parallel imaging was combined with partial Fourier acquisition to speed up acquisition time to approximately 20 min. Gradient echoes were acquired with alternating readout gradient polarity at 6 equidistant echo times [2.34, 4.68, 7.02, 9.36, 11.7, 14.04] ms. Two additional echoes were acquired for the PDw and T1w acquisitions at 16.38 ms and 18.72 ms.

B1 field mapping images (transmit B1+ and receive B1- fields) were also acquired to reduce spatial heterogeneities related to B1 effect, which was essential for proper quantification of T1 (or $R1=1/T1$) in particular. Finally, B0 field mapping images were acquired for image distortions correction: two magnitude images acquired at 2 different TE's, and pre-subtracted phase images.

To obtain quantitative maps from the MRI data, the following processing steps were performed using the SPM12 software (www.fil.ion.ucl.ac.uk/spm) and the hMRI (<https://hmri.info/>) toolbox, which is an extension to SPM (Tabelow et al., 2019). T1-weighted (T1w), proton density-weighted (PDw), and magnetization transfer-weighted (MTw) images acquired at multiple TEs were extrapolated to TE=0 to increase the signal-to-noise ratio and remove the otherwise remaining $R2^*$ bias (Tabelow et al., 2019). The TE=0 extrapolated MTw, PDw, and

T1w images were then used to calculate MT saturation (MTsat), R1 and apparent signal amplitude (A^*) maps. A^* maps were rescaled using the receive fields to generate PD maps. All quantitative maps were corrected for inhomogeneities caused by local RF transmit field ($B1+$), using $B1$ and $B0$ field mapping images (Lutti et al., 2010). The receive bias field map ($B1-$) was used to correct PD maps for instrumental biases (Ashburner and Friston, 2005). $R2^*$ maps were estimated using the ESTATICS method from the three different at low angle shot (FLASH) acquisitions by accounting for the varying contrasts. Additionally, the ordinary least squares (OLS) log-linear fit was applied to identify, and down-weight echoes affected by motion artifacts (Weiskopf et al., 2014). $R1$ maps were corrected for the radio frequency (RF) transmit field inhomogeneity $B1+$ (Preibisch and Deichmann, 2009). Quantitative maps were segmented into gray matter (GM), white matter (WM), and cerebrospinal fluid (CSF) using MTw maps by the unified segmentation approach implemented in SPM (Ashburner and Friston, 2005). Inter-subject registration of the GM and WM tissue maps was performed using DARTEL, a nonlinear diffeomorphic algorithm (Ashburner, 2007). The tissue probability maps were subsequently normalized to the stereotactic space specified by the Montreal Neurological Institute (MNI) template using the resultant DARTEL template and deformations. Then, for voxel-based quantification (VBQ) analysis, specific tissue-weighted smoothing, with a 3mm FWHM isotropic kernel, was applied to avoid mixing values from different tissues classes, as would happen with standard Gaussian smoothing.

5.2.4 Cognitive Assessments

Our assessments focus on memory, attention, and executive functions. Global cognitive functioning was tested by the Mattis Dementia Rating Scale (MDRS) (Mattis, 1988).

Episodic memory efficiency was evaluated using the verbal Free and Cued Selective Reminding Test (FCSRT) that includes immediate and delayed free and cued recall tasks (Grober et al., 2009) and the Logical Memory subtest from the MEM-III. Additionally, visual episodic memory was assessed by means of the mnemonic similarity task (MST) which

assesses fine-grained discrimination between similar objects in recognition memory (Stark et al., 2019). Direct and reverse digit span tasks were used to assess working memory (St Clair-Thompson, 2010).

Several aspects of executive functioning were assessed including organized retrieval of semantic information in memory through the verbal fluency test, including Letter Fluency task and Category Fluency Task (Patterson, 2011), inhibitory abilities were tested using the Stroop test (Stroop, 1935), flexibility was tested by the Trail-making test (Correia et al., 2015). Updating of information in working memory was assessed by the n-back task, with 1-back, 2-back and 3-back conditions (Zimmermann and Fimm, 1994).

Attentional functioning and processing speed were assessed by a Choice Reaction Time (CRT) task (Salthouse et al., 1991), the Digit Symbol Substitution Test (DSST) (Wechsler, 1997), and a divided attention task from Paced Auditory Serial Addition Test (PASAT) (Gronwall and Sampson, 1974).

The preclinical Alzheimer's cognitive composite (PACC5) score (Donohue et al., 2014; Papp et al., 2017), was obtained by the sum of z-scores of the following cognitive measures: Free and Total Recall in the Free and Cued Selective Reminding Test (FCSRT), Delayed Recall in the Logical Memory Test, Total score in the Digit Symbol Substitution Test, scores in the Category Verbal Fluency Tests, and Mattis Dementia Rating Scale.

In addition, we computed composite scores for attention, executive function, and memory. The composite attention score was calculated as the sum of DSST, 1back (dprime: performance accuracy calculated by contrasting correct and incorrect answers), and TMT-A (RT, where RT stands for reaction time). The executive function composite score is a combination of reverse digit span, TMT-B (RT), Verbal fluency sum (2 min. score for category and letter), and 3-back (dprime). The composite memory score is derived from FCSRT (sum of all free recalls), MST (recognition memory (RM) scores representing hits minus false alarms), and logical memory (delayed recall).

To assess the rate of decline in cognitive function, decline scores were computed as the baseline performance minus the follow-up performance, divided by the baseline performance, so that a higher score indicates a greater decline over the 2 years. Decline scores were obtained for the three composite scores as well as for the PACC5 score. Composite scores and PACC5 scores at the baseline and decline scores in cognitive assessments for the 67 subjects are presented in **Table 5-1**.

5.2.5 Statistical Analysis

In this study, we only employed composite cognitive scores and the PACC5 score for the statistical analysis. Gray matter (GM) and white matter (WM) are processed separately, using explicit non-overlapping GM and WM masks. Quantitative maps contain different units, addressing distinct tissue properties; for instance, Hertz for R2* and R1, and p.u. for MTsat and PD maps, therefore they are not directly comparable. To ensure comparability across different maps within the multivariate model, all maps underwent Z-transformation, per modality and across subjects, using the grand mean and variance calculated over each voxel. All statistical analyses were performed on standardized data.

To perform statistical analysis, first, we used separate linear regression models embedded in the general linear model (GLM) framework of SPM12 for 5 parameter maps (GM: MTsat, R1, R2*, PD, GM volume; WM: MTsat, R1, R2*, PD, WM volume). Age, gender, and education were added as covariates of no-interest, while in each model, one of the composite scores (memory, executive function, attention, and PACC5) was used as the regressor of interest. Therefore, a total of 4 regressors (age, gender, education, and one composite score) were used in each regression model to assess myelin, iron, as well as volume and free water content with respect to each cognitive composite score.

Next, in order to assess association of different characteristics of the brain, we tested for the association between cognition and combined micro- and macro-structural characteristics of the brain by jointly processing all the standardized maps in a multivariate GLM model, with the same regressors using MSPM toolbox (Gyger et al., 2021) in SPM12.

To further investigate the results obtained with the multivariate approach, we returned to univariate correlation analysis in the gray matter for each map, within the regions of interest (ROI) segmented using Neuromorphometrics, Inc. label template (Bakker et al., 2015). The ROIs were selected based on the significant clusters from the multivariate model F-tests. Segmented masks are applied on z-transformed raw maps. We then calculated the correlation between the mean voxel values within each masked map and the cognitive composite score after controlling for age, gender, and education as covariates of no interest.

For all regression analyses, we report the results at $p < 0.05$ after family-wise error (FWE) correction at cluster-level for multiple comparisons across the GM or WM compartment. The results are overlaid on the population mean GM or WM maps. The regions are reported based on the AAL3 atlas. For the multivariate analyses, contribution of each map is reported from the absolute values of their corresponding canonical vectors in each cluster (Gyger et al., 2021).

5.3 Results

5.3.1 Baseline scores

Univariate analyses

The coordinates for the peak voxel within the significant clusters from all univariate regression analyses at the baseline are presented in

Table 5-2. We did not find any significant relationship between R1 maps and any of the cognitive aspects.

Attention. Univariate analyses at the baseline revealed no significant correlations between attention and MTsat, R1, R2* and PD maps, and GM or WM volume.

Table 5-2. Univariate regression results at the baseline, showing the correlation between different maps and cognition. Brain regions were labeled with the AAL3 atlas toolbox in SPM. Coordinates are reported in MNI space. This table shows 3 local maxima more than 8.0 mm apart within the clusters. The cluster peak values are reported after FWER correction for $p < 0.05$ at either voxel or cluster level.

peak [x y z] Coordinates	Tissue	Modality	Cluster P-value FWERcorr (voxel-level)	Cluster Size #voxels	Brain Region
Executive function (df=96)					
[35 -53 -45]	GM	GMvol	0.000(0.000)	575	Right Cerebellum VIII
[39 -27 -17]	WM	PD	0.006(0.003)	64	Right Fusiform
Global memory (df=96)					
[-11 -46 -45]	GM	MTsat	0.009(0.026)	1991	Left Cerebellum IX
[-11 -46 -51]					Left Cerebellum IX
[-29 -18 -14]	GM	MTsat	0.002(0.004)	1105	Left Hippocampus
[-26 -20 -23]					Left Para hippocampal G
[9 -48 -23]	GM	MTsat	0.011(0.631)	1908	Right Cerebellum IV_V
[-2 -56 -22]					Vermis IV_V
[7 -37 -16]					Cerebellum III
[-24 -64 29]	WM	MTsat	0.000(0.009)	16565	Left Mid. Occipital G
[-52 -46 40]					Left Inf. Parietal G
[-19 -45 48]					Left Precuneus
[-9 -48 -27]	WM	MTsat	0.003(0.009)	7305	Left Cerebellum IV_V
[6 -47 -25]					Vermis III
[-14 -43 -44]					Left Cerebellum IX
[9 -33 57]	WM	MTsat	0.000(0.054)	23922	Right Paracentral lobule
[6 -24 32]					Right MCG
[32 1 30]					Right MFG
[-17 5 -18]	GM	PD	0.040(0.372)	1359	Left Olfactory bulb
[-26 16 -13]					Left Insula
[-28 18 -5]					Left Insula
[36 -26 35]	WM	PD	0.046(0.021)	798	Right Postcentral G
[29 37 19]	WM	PD	0.004(0.037)	1375	Right Mid. Frontal G
[40 24 31]					Right Mid. Frontal G
[28 29 28]					Right Sup. Frontal G
[-52 -45 40]	WM	PD	0.731 (0.045)	194	Left Inf. Parietal G
[-31 -32 48]	WM	PD	0.017(0.030)	1218	Left Postcentral G

[-32 -32 39]						Left Inf. Parietal G
[-40 -30 54]						Left Precentral G
[46 13 0]	GM	R2*	0.005(0.214)	2276		Right Insula
[37 4 -10]						Right Insula
PACCS (df=96)						
[-60 -28 -12]	WM	MTsat	0.467(0.036)	652		Left MTG
[0 36 -9]	GM	R2*	0.138(0.032)	979		Left ACG

Key: GM: gray matter; WM: white matter; G: gyrus Cerebellum IV_V: lobule IV, V of cerebellar hemisphere; Vermis IV_V: lobule IV, V of vermis; MCC: middle cingulate gyrus; MTG: middle temporal gyrus; ACG: anterior cingulate gyrus.

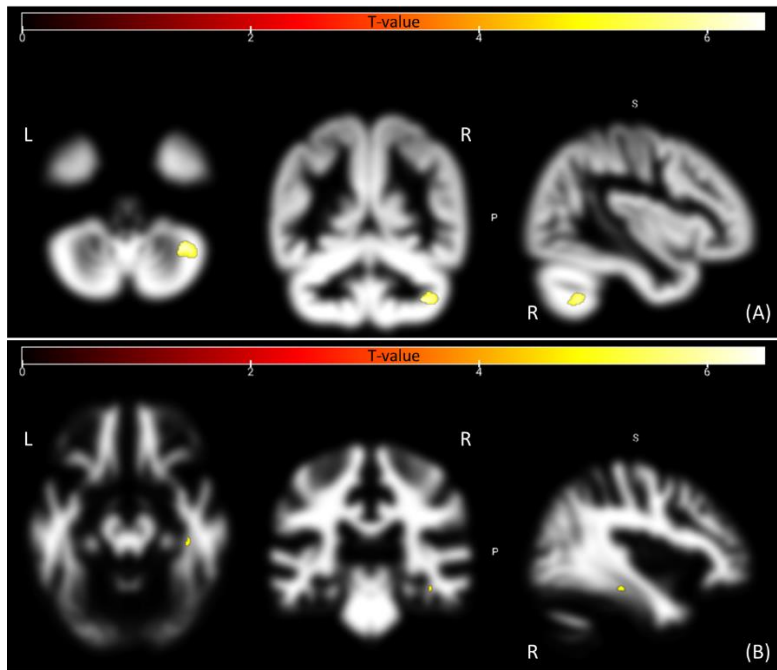


Figure 5-1. Statistical parametric maps (SPM) for the regression analysis, using executive function as the covariate of interest. (A) gray matter volume positive association with executive functioning. (B) negative association between PD maps in white matter with executive functioning. The SPMs are shown at $p < 0.05$ corrected for FWER at cluster-level, and they are overlaid on the mean population gray matter and white matter maps in MNI space.

Executive function. Following correction for FWE rates at the voxel level ($p < 0.05$), a positive correlation was found between executive function and GM volume in a large cluster within the right cerebellum. Furthermore, a negative association was observed between PD maps in WM and executive function in the right fusiform and hippocampal area. **Figure 5-1** illustrates the statistical parametric maps for the univariate analysis with executive function as the covariate of interest at the baseline.

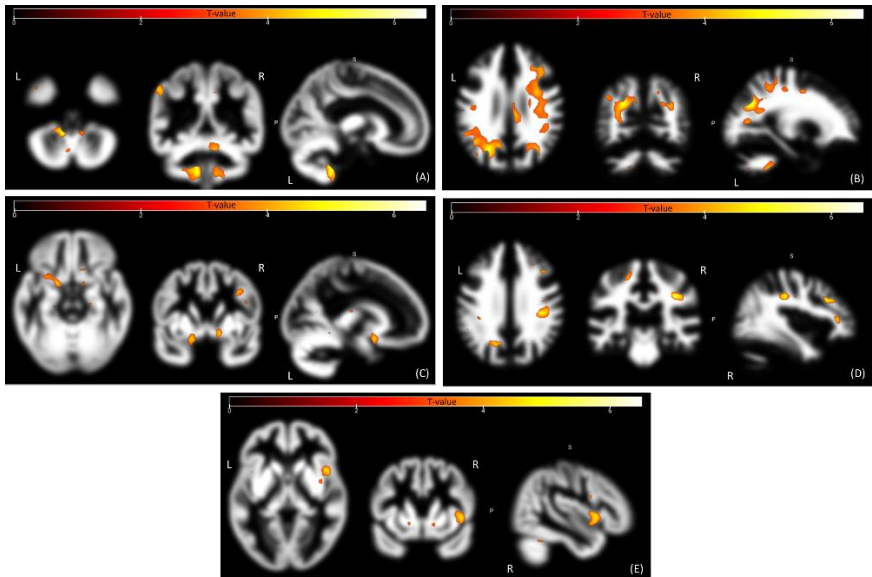


Figure 5-2. Statistical parametric maps for univariate analysis, using memory as the covariate of interest. (A) positive association between gray matter MTsat signal and memory, (B) positive correlation between white matter MTsat signal and memory, (C) positive correlation within the PD gray matter map with memory, (D) negative association between white matter PD signal and memory, (E) negative correlation between $R2^*$ gray matter signal and memory. The SPMs are shown at $p < 0.001$ uncorrected for illustration purposes, and they are overlaid on the mean population gray matter and white matter maps in MNI space.

Memory. In GM, positive correlations were detected between MTsat map and memory bilaterally in the cerebellum. In WM, positive correlations between memory and MTsat map were found bilaterally in

large clusters covering left and right cerebellum, left middle and superior occipital lobe, right paracentral lobule and superior motor area, and middle cingulate gyrus on the right side of the brain. A positive association between PD GM signal and memory was detected in the left olfactory bulb, while a negative association was detected within the PD WM map and memory bilaterally in postcentral regions, right middle frontal gyrus, left inferior parietal and supramarginal gyri, and left medial frontal gyrus. Moreover, R2* GM signal had a negative association with memory in the right insula. WM volume exhibited no positive correlation with memory. The statistical parametric maps for T-test analysis for the association of memory with different maps are illustrated in **Figure 5-2**.

PACC5. Regarding PACC5, a significant positive correlation was only observed within the WM for MTsat maps in the left middle temporal region at the voxel level. A negative correlation between R2* GM signal and PACC5 was found in the medial orbitofrontal cortex. See **Figure 5-3** for the statistical parametric maps.

Multivariate regression analyses

No significant association was observed between attention and all maps. In contrast, as illustrated in panel (A) of **Figure 5-4**, a significant correlation in the right cerebellum was detected between executive function and GM signal from all maps.

In gray matter, memory showed a correlation with all the combined modalities in the right anterior cingulate gyrus (ACG) and insula (**Figure 5-4**, panel B). Moreover, in white matter, memory was associated with the combined signals from all modalities in the left supramarginal and right middle frontal regions at the voxel level (**Figure 5-4**, panel C). There was a correlation in the right ACG between PACC5 and all the combined modalities (**Figure 5-4**, Panel D). The peak voxel coordinates for the significant clusters surviving the $p < 0.05$ FWER correction at cluster level are presented in **Table 5-3**.

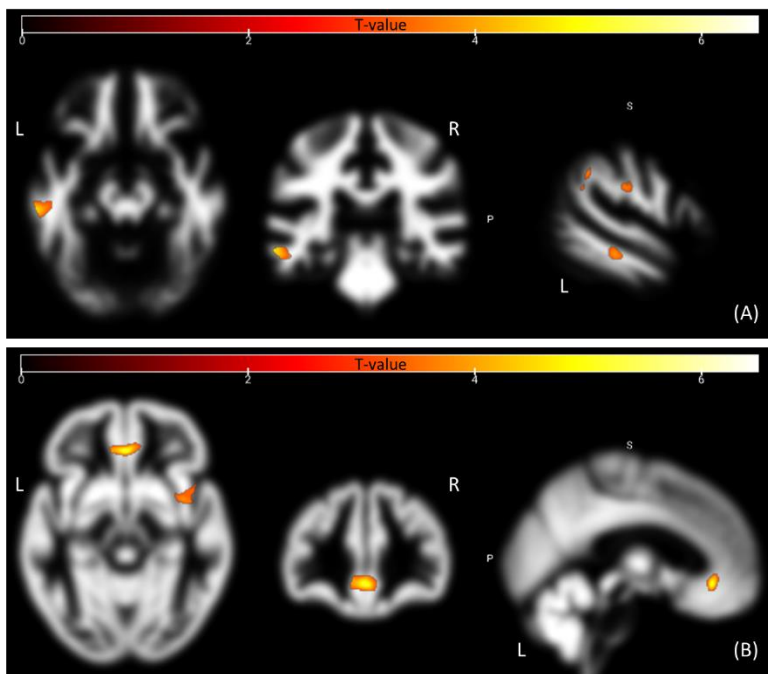


Figure 5-3. Statistical parametric maps for the univariate regression analyses, using PACC5 as the covariate of interest. (A) negative association of R2* gray matter signal with PACC5. (B) positive association between MTsat maps in white matter with PACC5. The SPMs are shown at $p < .001$ uncorrected for illustration purposes, and they are overlaid on the mean population gray matter and white matter maps in MNI space.

The canonical vectors showing the contribution of each dependent variable to the test statistics were calculated. The canonical vectors for the peak voxel of the reported significant clusters in the multivariate model (see **Table 5-3**) are presented in **Figure 5-5** (within the GM) and **Figure 5-6** (within the WM). Note that in our case, only the weights of the canonical vectors are meaningful. Gray matter volume explains the major proportion of cognition-related (executive function, memory, and PACC5) variance across gray matter. Consistently, within the WM, among different modalities, white matter volume was the dominant factor explaining the memory-related variance.

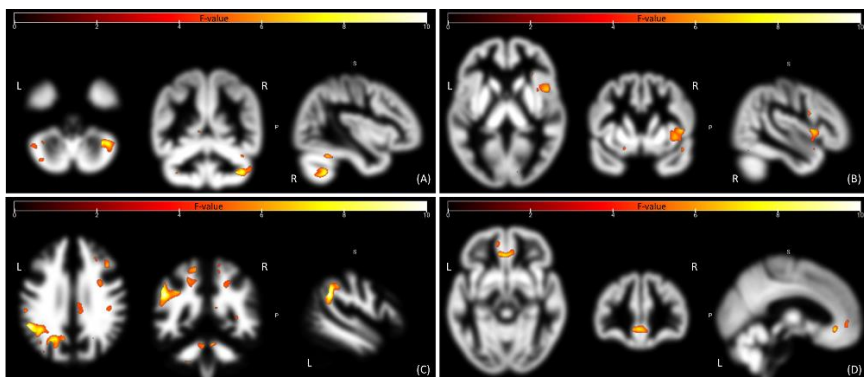


Figure 5-4. Statistical parametric maps (SPM) for the multivariate regression analyses within gray and white matter. The multivariate SPMs (mSPMs) show correlations between all modalities within either white matter or gray matter with respect to different cognitive composite scores (A) executive function within the gray matter, (B) memory within the gray matter, and (C) memory within the white matter, (D) PACC5, within the gray matter. The mSPMs are shown at $p < .001$ uncorrected for illustration purposes, and they are overlaid on the mean population gray matter and white matter maps in MNI space.

5.3.2 Cognitive decline at 2-year follow-up

At follow-up, 67 participants took part in the same cognitive assessment as at baseline and decline scores were computed. Of note, for some participants, all cognitive scores allowing us to compute the composite scores were not available. Therefore, the composite score and the related decline score were not calculated in these cases. The number of participants for which the decline scores could be related to brain measures is as follows (# valid scores for attention, executive function, memory, and PACC5 are 64, 66, 62, 62 respectively).

A Shapiro-Wilk normality test was performed on the residuals of the decline scores of composite scores for attention, executive function, memory and PACC5. This ensures us of the normality of the rate of decline within each cognitive aspect, allowing us to perform the same statistical tests as we did at the baseline.

Table 5-3. Multivariate regression results at the baseline, showing the correlation between different maps together (in GM or WM) and cognition. Brain regions were labeled with the AAL3 atlas toolbox in SPM. Coordinates are reported in MNI space. FWER correction was applied for $p < 0.05$ at voxel or cluster level.

peak [x y z] Coordinates	Tissue	Cluster P- value (voxel- level)	Cluster Size #voxels	Brain Region
Executive function				
[41 -53 -45]	GM	0.026(0.089)	1370	Right Cerebellum
Global memory				
[3 34 -12]	GM	0.015(0.057)	1557	Right ACG
[47 10 4]	GM	0.005(0.435)	1974	Right Insula
[-50 -47 31]	WM	0.001(0.005)	3402	Left Supramarginal G
[30 37 19]	WM	0.074(0.016)	1253	Right Mid. Frontal G
[-21 -62 29]	WM	0.003(0.036)	3011	Left Sup. Occipital G
[33 3 36]	WM	0.210(0.045)	794	Right Mid. Frontal G
[-49 -49 33]	WM	0.000(0.000)	1577	Left Supramarginal G
[32 4 37]	WM	0.002(0.000)	801	Right Mid. Frontal G
PACC5				
[-2 36 -9]	GM	0.026(0.254)	1379	Left ACG

Key: GM: gray matter; WM: white matter; ACG: anterior cingulate gyrus; G: gyrus.

Univariate analyses

No significant correlation was observed between the rate of decline in attention or executive function and GM and WM volume, MTsat, PD, and R2* gray matter and white matter maps. A significant negative correlation ($p < 0.05$ FWER-corrected at voxel level) was detected between gray matter R1 signal within the left fusiform and decline in attention (i.e., greater decline indexed by a higher decline score was related to smaller R1 signal). Decline in memory shows to be negatively correlated ($p < 0.002$ FWER-corrected at cluster level) with gray matter R1 signal in the left fusiform region.

Multivariate analyses

No significant correlation was detected using the multivariate regression for different maps and cognitive scores.

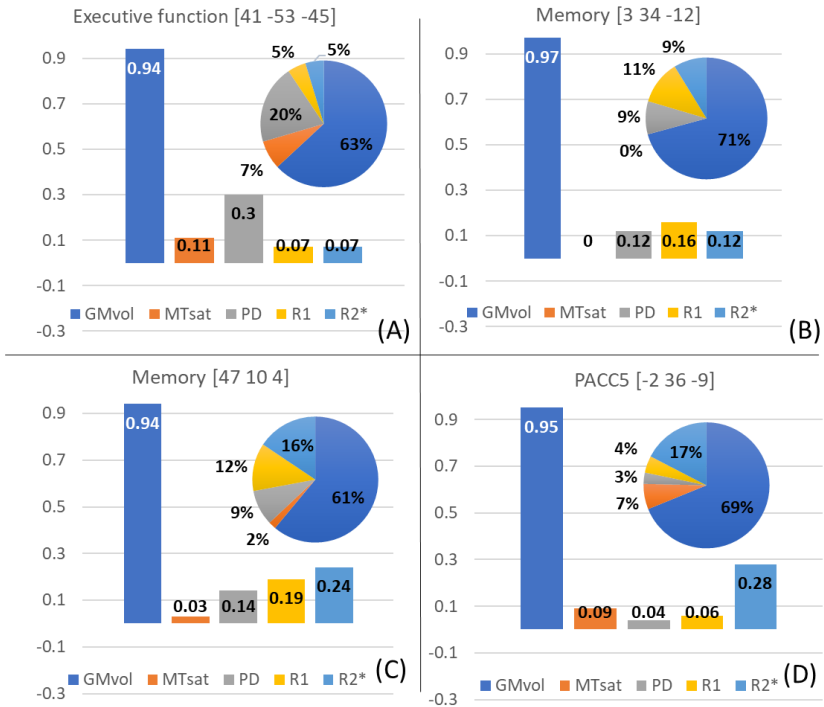


Figure 5-5. Canonical values for the peak voxels within the significant clusters in the GM. A) The peak voxel canonical value for correlation between executive function and all modalities within the right cerebellum, B) and C) The peak voxel canonical value for correlation between memory and all modalities within the right anterior cingulate gyrus and right insula respectively, D) The peak voxel canonical value for correlation between PACC5 and all modalities within the left anterior cingulate gyrus. The pie charts illustrate the percentage of contribution of each modality to our multivariate model.

5.4 Discussion

The findings of this study provide insights into the relationship between cognitive function and various micro- and macro-structural brain properties in healthy older adults. The results point to associations between cognition and all types of brain changes that were investigated: gray and white matter volume, iron levels, myelin content, and water

content. As already demonstrated by previous studies (Callaghan et al., 2014; Draganski et al., 2011), aging affects the brain at various levels, including the microstructural level indicative of neurobiological factors such as oligodendrocyte integrity, ferritin levels, and myelin production. In this study, we additionally show that such changes are related to cognitive performance in domains that are particularly vulnerable to aging such as episodic memory and executive functions.

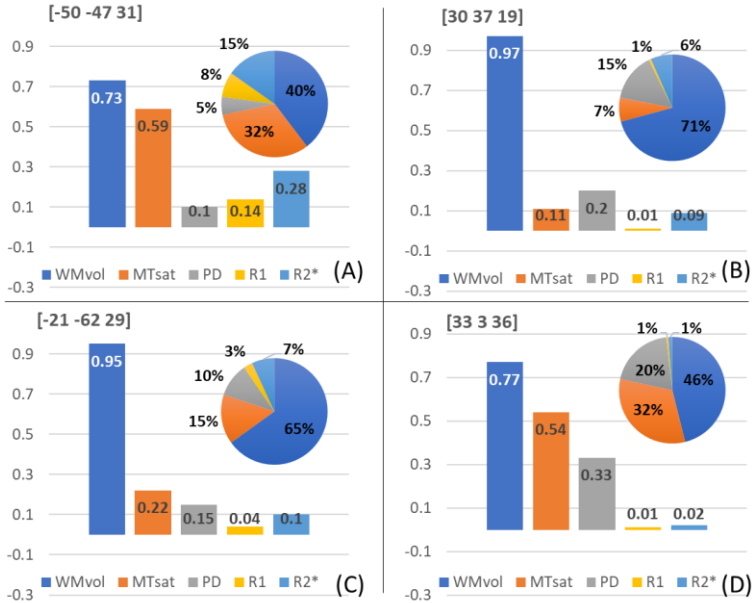


Figure 5-6. Peak voxel canonical vector within the WM for memory. The vectors are reported at the peak voxels within the A) left supramarginal, B) and D) right middle frontal, and C) left superior occipital areas. The percentages in the pie charts show the contribution of each modality to the multivariate model.

Executive function

Executive functioning was related to cerebral changes in the cerebellum and fusiform/hippocampal area. The cerebellum, traditionally linked to motor coordination, has increasingly been recognized for its role in cognitive processes, including executive functions (Beuriat et al., 2022, 2020; Jacobs et al., 2018). There is a clear segregation between “sensorimotor” and “cognitive” cerebellum, with

the former in the anterior lobe (Jacobs et al., 2018) and the latter in the posterior lobe (lobules VIIa, Crus I, and II), connecting to the prefrontal and posterior-parietal cortices related to cognitive and emotional functions (Cheng et al., 2023). In this study, the significant associations between the executive function and gray matter volume in the right cerebellum were specifically in lobules VIII, VIIb, and Crus II. The observation that the combination of micro- and macrostructural measures in the cerebellum correlated with executive function additionally points to the particular vulnerability of this region in aging and its role in supporting executive functioning.

WM volume loss within the cerebellum has been previously observed in aging (Taubert et al., 2020). Furthermore, WM volume tends to decline more rapidly than gray matter (GM) volume in the cerebellum and extends into the anterior lobe in AD patients (Jernigan et al., 2001). However, we could not detect any cognitive-related variation in WM volume maps in our study.

We also identified a negative correlation between executive function and white matter PD maps in the right fusiform and hippocampal regions. These findings align with previously published age-related changes in the free water contents within WM (Callaghan et al., 2014; Taubert et al., 2020), and may suggest that alterations in white matter microstructure in these regions contribute not only to aging but also to executive function decline.

Memory

Memory performance was related to the integrity of many brain regions across various imaging modalities, also when considering their co-occurrence. As for executive functions, the cerebellum appears to contribute to age-related memory decline. The entire cerebellum receives modulatory input from the inferior olivary nuclei and the locus coeruleus, which contribute to sensorimotor and memory functions (Jacobs et al., 2018). Cerebellum's involvement in memory processes is consistent with emerging research (Almeida et al., 2023; Beuriat et al., 2020). Task-related fMRI studies in individuals with mild cognitive impairment (MCI) have shown a reduced activation within the posterior

lobe (lobules V, VI and crus I). This activation reduction also included the anterior cerebellar regions in AD patients (Braskie et al., 2013, 2012).

In aging, alterations in myelin sheaths are frequently observed within the primary visual cortex (Peters et al., 2000) and middle frontal cortex (Peters and Sethares, 2002). Myelin alteration in the left hippocampus and cerebellum was found significantly correlated with the decline in memory that occurs with increasing age (Steiger et al., 2016). This correlation could be explained by the reduction in the speed of conduction along nerve fibers associated with demyelination, which disrupts the memory network. In this study, we also found that poorer memory performance is associated with lower myelin content within the GM in the left temporal lobe, covering hippocampus and fusiform cortex, and the left cerebellum covering lobules VIII, IX.

Within the WM, we found that less myelination in the left middle occipital and cerebellar regions (lobules VIIb, VIII, IX) is associated with worse memory performance. This is in line with age-related alterations in MT maps (Draganski et al., 2011; Steiger et al., 2016) and cognitive-related changes in myelin sheaths (Peters et al., 2000). Here, we did not detect any significant correlation between the GM/WM volume and memory.

Taubert et al. (2020) reported a decrease in PD maps with respect to aging in the frontal, parietal, temporal, insular, occipital, and cerebellar lobes as well as in the basal ganglia and thalamus. They also demonstrated an increase within the PD maps bilaterally in the somatosensory and motor cortices and parietal areas. In a recent review on microstructural gray matter changes in AD and MCI, using NODDI images, (Zhong et al., 2023) showed that no significant association was observed between the orientation dispersion index (ODI) and cognition, but the neurite density index (NDI) was significantly correlated to MMSE and Montreal cognitive assessment (MoCA) scores. Our results, however, reveal a positive correlation between memory performance and PD values in the olfactory bulb and negative associations within the white matter bilaterally in frontal, parietal, and supramarginal regions. Olfaction is a sensory perception, and its dysfunction may manifest early

in neurodegenerative diseases and other diseases, olfactory functioning may be a valid indicator of the integrity of the aging brain (Attems et al., 2015).

Increased levels of iron with respect to aging is confirmed in the basal ganglia, caudate, ventral striatum, putamen, thalamus, and pallidum (Acosta-Cabronero et al., 2016; Bartzokis et al., 2000; Ficiarà et al., 2022; Steiger et al., 2016). Iron level in the sensory-motor cortex and insular areas were also found to be associated with age (Acosta-Cabronero et al., 2016). In this study, we showed that increased iron level (greater R2* signal) is associated with poorer memory performance in the right insula. The involvement of the insula in memory is dependent on the saliency of the cues or events, which is marked through dopaminergic and cholinergic signaling (Gogolla, 2017). Moreover, the insula mediates dynamic switching between the central executive network and the default mode network, facilitating access to cognitive resources, such as attention and working memory, when a salient event is detected (Namkung et al., 2017).

PACC5

We observed a positive correlation between PACC5 and WM MTsat maps within the left middle temporal lobe. This region is primarily associated with functions related to language and auditory processing. PACC5 scores were also related to iron content, as well as a combination of all imaging modalities, in a region encompassing the anterior cingulate and posterior orbitofrontal cortex. This region has been shown to be particularly vulnerable to aging (Resnick et al., 2007) and contributes to the control over other brain regions during demanding tasks and to the decoding of sensory inputs (Rolls, 2004). Although iron level in the medial temporal lobe was shown to change in case of AD (Zeineh et al., 2015), we could not detect any significant associations between the PACC5 score and medial temporal areas such as hippocampus. This lack of correlation could be attributed to the high cognitive performance and overall health of our participants. Our results suggest that iron deficits in the middle temporal lobe are more prominent when no cognitive impairment is evident.

Cognitive decline

When examining the rate of cognitive decline, we observed a significant negative correlation between gray matter R1 signal and memory and executive function decline, particularly in the left fusiform region. This result suggests that changes in R1 signal in this region may serve as an early indicator of cognitive decline in aging individuals. However, it is challenging to determine if this association is driven by iron content or myelin, as the R1 map is proportional to both brain tissue characteristics (Stüber et al., 2014). However, there are studies that emphasize on the R1 signal strong relationship between R1 and tissue myelin content (Sigalovsky et al., 2006).

Multivariate analyses

In this study, we demonstrated that various tissue properties are associated with cognition and aging. Therefore, it is essential to recognize that cognitive aging cannot be solely explained by GM and WM atrophy. Instead, brain tissue properties that exhibit complex interactions (Hardy and Higgins, 1992; Villain et al., 2010; Falahati et al., 2017; Nasrabady et al., 2018; Biel et al., 2021) also play roles. Due to the interaction between different brain tissue properties, employing a multivariate model that simultaneously measures property variations in relation to cognition and its decline could yield more specific results.

Previous research has already assessed age-related variations within different tissue properties, revealing associations across diverse brain regions (Callaghan et al., 2014; Draganski et al., 2011; Taubert et al., 2020). Our findings include correlations between executive function and GM signal from all maps within the right cerebellum, covering parts of lobules VIIb, VIII, and crus II. These results underscore the significance of this region in executive functioning (Beuriat et al., 2022; Cheng et al., 2023; Jacobs et al., 2018), emphasizing the cerebellum's role in cognition and aging.

Within GM, memory displayed correlations within the right anterior cingulate gyrus (ACG) and insula. This aligns with cognitive aging studies in macaque monkeys that stress the importance of the prefrontal cortex in cognition and memory (Upright and Baxter, 2021). In white matter,

we detected correlations between memory and tissue micro- and macro- structural properties in frontal and occipital areas which agrees with age-related associations shown in (Taubert et al., 2020).

Concerning the association between PACC5 and all maps, we detected correlations within the right ACG. The ACC shows to decline in metabolism with aging (Pardo et al., 2007), and it is involved in diverse cognitive tasks (Apps et al., 2016). Moreover, memory displayed significant correlations within the white matter with all maps together in the left supramarginal and bilaterally in right middle frontal gyri regions at the voxel level. (Rajah et al., 2011) showed that the volume of middle frontal gyrus is associated with the activity in episodic memory network. However, the multivariate approach couldn't pinpoint a specific region correlating with the two-year decline rate.

Overall, these findings advance our understanding of cognitive aging and its potential links to brain micro- and macro- structural properties. The study highlights the multifaceted nature of cognitive decline, underscoring the importance of considering both micro- and macro-structural brain changes in the context of aging. We emphasize the importance of cerebellum in cognitive aging, particularly in executive functioning. These implications could be further used for early detection, prevention, and intervention strategies for age-related cognitive decline and neurodegenerative diseases, such as Alzheimer's disease. Further research is needed to elucidate the underlying mechanisms and to develop targeted interventions to mitigate cognitive decline in aging populations.


Chapter summary

The aging process is often accompanied by cognitive alterations, collectively known as cognitive aging, which can lead to a decline in functional capacity. Normal aging is also accompanied by macro- and micro- structural changes in the brain, such as gray matter (GM) and white matter (WM) atrophy, iron accumulation, and demyelination.

This study investigates the association between cognition and various brain micro- and macro-structural properties over a 2-year period in healthy older adults (baseline: n=101, 31.68% male, follow-up: n=67, 32.84% male). Participants underwent cognitive assessments at baseline and after 2 years, resulting in composite scores for attention, executive function, and memory. The preclinical Alzheimer's cognitive composite (PACC5) was calculated for all participants. Quantitative MRI data were obtained at baseline using a multiparametric mapping protocol. The association between cognitive composite scores and tissue properties, both at baseline and for cognitive decline over 2 years, was tested using univariate and multivariate general linear models.

The univariate analyses conducted at baseline revealed several significant associations between cognition and brain structural properties. Executive function showed a positive correlation with GM volume in the cerebellum, while memory exhibited positive associations with myelin content in the cerebellum and hippocampus. GM iron levels were linked to lower composite memory scores in the right insula. A significant positive correlation emerged between WM myelin content and PACC5 in the left middle temporal region. Conversely, higher iron levels in the medial orbitofrontal cortex were associated with smaller PACC5 values. Multivariate regression analyses at baseline revealed significant associations between executive function and the combination of macro- and microstructural changes in the cerebellum, as well as between memory and combined changes in the cingulate gyrus and insula. Finally, multivariate regression did not reveal any significant correlations between the different maps and cognitive decline.

In summary, these findings highlight the intricate relationships between cognition and brain micro- and macro-structural properties in aging, with a particular emphasis on the role of the cerebellum in cognitive aging.

Chapter **6** 

Discussion and Conclusion

6.1 General Discussion

Aging is the first and an inevitable risk factor for neurodegenerative diseases, with Alzheimer's disease standing as the most common form of dementia. The prevalence of AD is increasing all over the world, mirroring the rise in life expectancy. While the accumulation of amyloid-beta and the pathological aggregation of neurofibrillary tangles are recognized as hallmark features of AD, research has unveiled additional biomarkers such as demyelination, iron accumulation, free water content, and synaptic density alterations that contribute to cognitive impairment and AD development.

It is hypothesized that there is a cascade of pathological processes in which increased iron levels and decreased myelin content contribute to the death of neurons and a reduction in synapses (Bartzokis, 2011). To prove this hypothetical sequence, a longitudinal study would be necessary. However, we hypothesized that when amyloid-positive individuals with cognitive decline symptoms reach the clinical stage, there should be concurrent changes in myelination, iron levels, and synaptic density if they are indeed interconnected in earlier stages.

Moreover, gray matter volume loss has proven to be a sensitive marker for neurodegeneration (Mc Donald et al., 2010). In mild cognitive impairments (MCI) and AD, patterns of GM volume reduction and amyloid-beta aggregation have notably been previously observed in frontal regions of the brain (Wirth et al., 2018).

The exact order in which these risk factors exert their effects is still under investigation, but emerging evidence suggests that these biomarkers do not act independently; instead, they appear to interact and influence each other (Bartzokis, 2011; Calabrò et al., 2020).

The main goals of this thesis center on investigating the simultaneous presence of macroscopic and microscopic brain tissue properties within both the gray and white matter of aging brains. To accomplish this objective, we had to address some critical research questions:

1. Are we able to detect differences in the brain micro-structural properties in healthy adults vs. AD patients using quantitative

neuroimaging techniques? Additionally, would a combination of brain property quantitative maps together empower us in indication of brain regions initially affected by AD?

2. Is it possible to identify specific regions within the brain where the co-occurrence of micro-structural alterations is more likely to manifest with respect to individuals' age?
3. How cognitive performance and its decline relate to micro-structural characteristics within the brain in healthy older adults?

In this thesis, various quantitative MRI maps were employed to assess brain myelin, iron, and free water contents including magnetization transfer saturation, effective transverse relaxation rate, and proton density. Synaptic density was assessed using the total volume distribution map generated from [F^{18}]UCB-H PET images, while gray matter and white matter volume maps were derived from structural MR images via Voxel-Based Morphometry (VBM) analysis.

Of note, all image data utilized in this thesis underwent a rigorous anonymization process and were standardized into the Brain Imaging Data Structure (BIDS) format (Gorgolewski et al., 2016; Karakuzu et al., 2022). Cognitive scores were assessed through a battery of different tests assessing short-term and long-term memory, executive functioning, and attention.

The investigation of (semi)quantitative maps in the context of Alzheimer's disease (AD) and cognitive aging represents a novel aspect of this research, offering valuable future avenues for the application of qMRI techniques in AD and cognitive studies.

Moreover, the multivariate statistical analysis on multiple image modalities highlights the complex association of different risk factors for AD. The canonical analysis showed the specific contributions of each modality to the multivariate tests, helping us better understand their respective impacts.

Hereunder, we will discuss the main findings presented within each chapter of this thesis.

Brain characteristics in AD vs healthy controls

In our first study, myelination, iron accumulation, gray matter volume, and synaptic density were assessed in patients with AD and healthy individuals in a univariate and multivariate manner to assess the co-occurrence of these AD-related neuropathological events at the voxel level.

We found a decrease in MTsat maps (indexing myelin) in AD participants in the hippocampal area and amygdala; which is in line with previously published results on human myelination in temporal lobe, and specifically the hippocampal regions (Bartzokis, 2004a; Benes et al., 1994; Braak and Braak, 1999). R^2^* analysis shows an increase in case of AD in the superior part of orbitofrontal cortex bilaterally as well as in the left hippocampus and right mid-temporal gyrus. These regions are reported to have low concentrations of iron in postmortem studies on healthy adults (Hallgren and Sourander, 1958). Our univariate analysis on GM volume also confirms atrophy in AD patients in hippocampus and amygdala, which is consistent with the known early neurodegeneration of the medial temporal lobe which is considered as a hallmark of AD (Dubois et al., 2007). Our findings on the synaptic density also agree with previous findings in (Chen et al., 2018); showing a bilateral synapses loss within the hippocampus, where we also detected demyelination and GM atrophy in AD patients.

The most critical finding of this study is provided by the multivariate analysis results, indicating a significant co-occurrence of demyelination, iron accumulation, atrophy, and synaptic loss bilaterally within the hippocampal region, left fusiform, and temporal regions in AD patients.

Under the assumption of independency of the quantitative maps, the canonical vector information reveals that within the multivariate model, where all the quantitative maps indexing myelin, iron, synaptic density, and GM volume are present, alterations in myelin content contribute the most, and iron accumulation contributed the least.

Overall, one key finding of this study is identification of myelin alterations as the leading factor in differentiating AD patients from healthy individuals. Myelin breakdown is at the core of the earliest

changes involved in AD progression and aging (Bartzokis, 2004a, 2004b). Demyelination, along with the subsequent neuronal loss, results in functional disconnections of associated cortical regions and progression to permanent deficits (Bartzokis, 2004a). Our results support previous findings, and suggest demyelination as the primary biomarker for developing AD.

The aging effect

In our second study, a multivariate approach was used to investigate how various microstructural tissue properties of the brain change with age. By examining quantitative maps for myelin, iron, and free water content simultaneously, this approach identified brain regions influenced by differences in these parameters. The multivariate analysis confirmed (Taubert et al., 2020) findings on correlations with age in regions such as caudate nucleus, putamen, insula, cerebellum, lingual gyri, hippocampus, and olfactory bulb. Importantly, it outperformed univariate analyses, by detecting more significant changes across various brain regions. Examining these properties individually could not reveal the findings as the multivariate model did (see **Figure 4-5**), which highlights the advantages of the multivariate approach.

Of note, MANOVA accounts for correlations, detects subtle effects, and manages family-wise error rates when analyzing multiple variables simultaneously. This approach yielded better results compared to multiple univariate ANOVAs. Finally, canonical vectors highlighted the contribution of each modality in the multivariate model within selected regions, known to be related to aging and dementia. Over the selected regions, in general and at voxel-level, PD maps made the most contribution to the results compared to other maps. However, within the right superior motor area, iron content is the most influencing factor in detecting age-related changes in brain microstructural tissue properties. Our results supports the findings of (Taubert et al., 2020) concerning co-occurrence of changes of $R2^*$, MTsat, and PD signal in the motor cortex. Our results provide evidence for the age-related differences impacted by the physical values derived from the quantitative maps.

Brain micro-structure and cognitive aging

Our last study aimed to uncover the mechanisms behind cognitive aging, particularly focusing on associations between cognition and gray and white matter volume, iron levels, myelin content, and water content.

Cerebellum gray matter volume was found positively associated to executive function. Executive function was also found to be associated to all tissue property maps at the baseline within the right cerebellum. These findings highlight the critical role of the cerebellum in cognition (Almeida et al., 2023; Beuriat et al., 2022, 2020; Jacobs et al., 2018). Moreover, higher levels of gray matter myelin content were associated with better memory performance in cerebellum and hippocampus. Hippocampus is known to be a critical structure for learning and memory (Anand and Dhikav, 2012). Furthermore, cerebellum was found associated with episodic memory (Almeida et al., 2023).

Our findings on the negative association between executive function and white matter proton density (PD) in the right fusiform and hippocampal regions suggest that age-related changes found in free water content in these regions (Callaghan et al., 2014; Taubert et al., 2020) contribute to executive function decline. Within the WM, the negative associations between PD maps and memory spread over different brain regions covering postcentral, middle, and superior frontal gyri, as well as precuneus. These results suggest that lower water content can be used as a biomarker for detecting age-related changes within the motor cortex (Taubert et al., 2020). Also, it may reflect the fact that white matter integrity decreases with aging, affecting connectivity, and that such compromised connectivity is particularly problematic for executive functions because such functions require large-scale networks.

PACC5, indexing preclinical composite score for AD, showed positive correlation with all maps in the multivariate approach within the anterior cingulate cortex, which is vulnerable to aging (Resnick et al., 2007). Moreover, the posterior ACC shows high functional connectivity with the para hippocampal regions (Rolls, 2019), which are involved in

memory, along with connections with precuneus, which is involved in spatio-topographical and related memory functions (Cavanna and Trimble, 2006). WM myelin content showed a positive association with PACC5 in the mid temporal gyrus, which confirms our previous findings for the lower myelin content within this region in AD patients (Moallemian et al., 2023b). Conversely, we report negative associations between gray matter iron levels (R^2^*) and PACC5 in the medial orbitofrontal cortex, covering pre-ACC. However, most of the previous works assessing iron with respect to aging and cognition have emphasized basal ganglia, and more specifically putamen as the brain region to be affected by changes in iron level (Biel et al., 2021; Tian et al., 2022). Our results also confirm the opposite relationship between demyelination and iron accumulation, as explained in the Introduction chapter of this thesis.

Within this longitudinal study, we investigated the rate of decline in cognition after 2 years. We looked for correlations between all tissue properties as assessed at the baseline and the decline in cognition. R1 maps, that are proportional to myelin and iron content in the brain, showed a correlation within the left fusiform for attention and memory decline. Although we cannot relate the result to the alterations of one of these brain properties alone, our findings are valuable in the sense that they show co-localization of alterations in myelin and iron contents in the brain.

The multivariate approach with respect to all tissue properties could not detect any significant correlations with the composite cognitive scores.

6.2 Limitations and future perspectives

Like any other study, we were confronted with limitations in our work. One major limitation of our work is the small sample size of the AD group, that limits the generalizability. The small sample size was also a limiting factor for using machine learning methods for clustering participants into different groups based on their brain tissue properties.

Moreover, the study included patients with AD at different stages. This heterogeneity within the AD group could increase variability in the findings, making it challenging to identify stage-specific effects. Future studies are needed to include larger and more homogeneous AD cases, allowing for more robust differentiation of the brain tissue properties between healthy control and mild cognitive impairment stage.

From a more physical point of view, we employed (semi)quantitative maps as assessed from MPM protocol to quantify myelin and iron within the brain tissues. However, these techniques may have limitations, including potential confounding factors and reduced specificity. For instance, MTsat maps might carry information on other macromolecular compounds in the brain that might reduce the specificity of MTsat to myelin alone. Inhomogeneous magnetization transfer (ihMT) is an alternative variant for MT that can address this issue (Munsch et al., 2021; Varma et al., 2020). Furthermore, future research should explore the use of quantitative susceptibility mapping (QSM) to overcome the limitations of $R2^*$, as it is independent of water content, echo time, and field strength (Li et al., 2021). More precise methods that can index brain tissue properties would lead to better understanding of the brain micro-structural behavior within the context of aging and cognition.

In our longitudinal study, the participants did not experience any significant decline in their cognition at the group level, even though there was individual variability with some participants showing decline and others showing either stability or improved scores. To better capture the neural correlates of cognitive decline, a longer period of follow-up or a selection of participants with subjective cognitive decline would be needed. A future study might also investigate cognitive aging and the changes in micro-structure of the brain of healthy participants using quantitative maps, which would allow a predictive approach that can help prognosis of AD before exhibiting high levels of amyloid-beta aggregation and noticeable cognitive impairment.

Throughout the thesis, we emphasized that multivariate models are preferable to multiple univariate models, as they reduce the chance of false positives. But it is noteworthy that MANOVA tests for effects of

interest on a combination of dependent variables. In other words, it investigates the relationships and covariation among the dependent variables. Therefore, to assess a specific dependent variable regarding some effects of interest, one needs to return to ANOVA.

In terms of statistical analysis, we suggest going beyond the standardized regression coefficients and employ regression commonality analysis (Nimon and Oswald, 2013); allowing partitioning the regression effect into commonality coefficients representing unique and shared variance between different model dependent factors. Therefore, commonality coefficients represent variance unique to one predictor and all possible subsets of predictors.

6.3 Conclusion

In conclusion, this research investigated complex relationships between various brain tissue properties, aging, AD, and cognition.


Firstly, in our investigation of brain characteristics in AD compared to healthy controls, we discovered a significant co-occurrence of myelin breakdown, iron accumulation, gray matter atrophy, and synaptic loss within specific brain regions, particularly in the hippocampus. This highlights the pivotal role of myelin alterations as a primary distinguishing factor in AD, suggesting that myelin breakdown is at the core of the earliest changes in AD progression and aging.

Secondly, our work on the aging effect on brain microstructural properties demonstrated the interplay of myelin, iron, and water content in various brain regions, shedding light on the specific areas influenced by these parameters. Our multivariate approach surpassed univariate analyses, emphasizing the advantages of considering these properties together to detect age-related changes more comprehensively.

Lastly, our study on brain microstructure and cognition uncovered several associations between different cognitive functions and brain tissue properties. Notably, the cerebellum emerged as a critical role player in cognition, and myelin content, iron levels, and water content were shown to impact various aspects of cognitive function.

In summary, this research provides a deeper understanding of the intricate relationships between brain tissue characteristics, aging, AD, and cognition.

These findings establish a solid foundation for future investigations and have the potential to inform the development of diagnostic and prognostic strategies for AD and age-related cognitive decline. Despite the constraints of our study, such as the small sample size and the need for more precise quantification methods, our work represents a pivotal step forward in unraveling the complexities of brain aging and AD.

Chapter **7** 

Appendices

7.1 Appendix-A: Statistical modeling

General Linear Model (GLM)

General Linear Model (GLM) is used in almost every statistical analysis. It is the foundation of the t-test, F-test, Analysis of Variance (ANOVA), Analysis of Covariance (ANCOVA), regression analysis, and many others e.g., multivariate methods including factor analysis, cluster analysis, multidimensional scaling, discriminant function analysis, canonical correlation.

When using a GLM, we hypothesize that the dependent variable can be explained by a weighted linear combination of a group of independent variables (covariates), in presence of errors that have normal distribution (Equation 7-1). In image processing, GLM is often used to examine the association between the signal within each voxel and specific covariates. In other words, a GLM would use some predictors to predict an observed phenomenon (Christensen, 2020). GLM can also be used to perform group comparisons. This can be done by including a categorical factor variable in our model, which allows for testing the difference between groups (e.g., patients vs. controls) while controlling for other factors.

$$Y = XB + E$$

Equation 7-1

Multivariate General Linear Model (mGLM)

The multivariate form of the GLM is also expressed as Equation 7-1, where Y is an $n \times m$ matrix of observations (dependent variables), X is the $n \times k$ design matrix (independent variables), B is the $k \times m$ matrix of model parameters (weights), and E is $n \times m$ matrix of normally distributed errors ($E \sim N(0, \Sigma)$). This can be written as:

$$\begin{pmatrix} Y_{11} & \cdots & Y_{1m} \\ \vdots & \ddots & \vdots \\ Y_{n1} & \cdots & Y_{nm} \end{pmatrix} = \begin{pmatrix} x_{11} & \cdots & x_{1k} \\ \vdots & \ddots & \vdots \\ x_{n1} & \cdots & x_{nk} \end{pmatrix} \begin{pmatrix} b_{11} & \cdots & b_{1k} \\ \vdots & \ddots & \vdots \\ b_{k1} & \cdots & b_{km} \end{pmatrix} + \begin{pmatrix} e_{11} & \cdots & e_{1m} \\ \vdots & \ddots & \vdots \\ e_{n1} & \cdots & e_{nm} \end{pmatrix} \quad \text{Equation 7-2}$$

Where n can be taken as the number of subjects, m as the number of dependent modalities (here, the number of different modalities), and k as the number of predictors. Estimation of B is usually performed using ordinary least squares, $\hat{B} = (X^T X)^{-1} X^T Y$, which is identical to performing m univariate estimates using the columns of Y .

In this context, the primary distinction from univariate methods becomes apparent, as we shift from a set of estimated parameters in vector form to a matrix format. This matrix consists of columns representing the m dependent variables and rows corresponding to the k predictors in X . To compute the multivariate residuals, we employ the equation $\hat{E} = Y - X\hat{B}$. This allows us to obtain an unbiased estimate of the covariance matrix $\hat{\Sigma} = \frac{1}{n-k} \hat{E}^T \hat{E}$ (Fox and Fox, 2016).

Here we use mGLM for modelling multimodal group-level images. Therefore, each row of Y represents measurements from one subject (for a particular voxel), and each column on Y represents a specific observation (image modality).

Hypothesis testing in the mGLM is based on contrast.

$$CBL = 0 \quad \text{Equation 7-3}$$

Here, the univariate scheme is extended by combining standard hypotheses C on the rows of B , and the hypotheses L on the columns of B . For multivariate ANOVA (MANOVA) models contrasts of main effects and interactions involve setting $L = I_m$, the $m \times m$ identity matrix, as the dependent variables are not assumed to be equivalent. This is the scheme most suitable for multimodal neuroimaging applications.

There is a choice of four standard test statistics that can be constructed based on the calculation of two sums-of-squares and cross products (SSCP) matrices. For any given contrast, there is an SSCP matrix associated with the hypothesis.

$$SSCP_H = (C\hat{B}L^T)^T [C(X^T X)^{-1}C^T]^{-1}(C\hat{B}L^T) \quad \text{Equation 7-4}$$

And the SSCP associated with the error

$$SSCP_E = L(\hat{E}^T \hat{E})L^T \quad \text{Equation 7-5}$$

When $L_{m \times m}$ is an identity matrix, the main diagonal of $SSCP_H$ contains the sums of squares for the hypothesis in C as applied to the estimated parameters for each dependent variable separately, and the $SSCP_E$ matrix is simply an unscaled form of the estimated covariance matrix $\hat{\Sigma}$.

Construction of a test statistic from this hypothesis-testing scheme can be done in a few ways. Generally speaking, the different methods all rely on some linear combination of the q eigenvalues $(\lambda_1, \dots, \lambda_q)$ of $SSCP_E^{-1}SSCP_H$. The four standard tests statistics (Hotelling, 1951; Lawley, 1938; Pillai, 1955; Roy, 1945; Wilks, 1932) are:

$$\text{Pillai's trace} = \text{trace} [(SSCP_H + SSCP_E)^{-1}SSCP_H] = \sum_{i=1}^q \frac{\lambda_i}{1+\lambda_i}$$

$$\text{Wilks's lambda} = \frac{|SSCP_E|}{|SSCP_H + SSCP_E|} = \prod_{i=1}^q \frac{\lambda_i}{1+\lambda_i}$$

$$\text{Hotelling-Lawley trace} = \text{trace}(SSCP_E^{-1} SSCP_H) = \sum_{i=1}^q \lambda_i$$

$$\text{Roy's largest root} = \frac{\lambda^*}{1+\lambda^*}$$

Where λ^* is the largest eigenvalue of $SSCP_E^{-1}SSCP_H$.

A natural question that arises is which test statistics should be used, but the answer to this question depends on the data itself. For example, a Pillai's trace is the most powerful test when the population eigenvalues are somewhat equal, whereas the Hotelling-Lawley trace is the most powerful test when they are unequal (Davis, 2002). These values are population parameters and are not controllable. (Davis,

2002) recommends Wilk's lambda on the basis that its power remains relatively consistent across simulation studies. It is worth mentioning that in most case scenarios, the F approximation to the test statistic is exact and will therefore be identical irrespective of the test chosen.

Approximations to an F-statistic and the corresponding degrees of freedom can be calculated for all these statistics, allowing the designation of an approximate p-value. Here we only bring the details for Wilk's lambda statistic (coded as Λ).

The Wilk's lambda test statistics can be calculated as a function of the q largest eigenvalues:

$$F(df_1, df_2) = \left(\frac{1 - \Lambda^{1/s}}{\Lambda^{1/s}}\right) \left(\frac{df_2}{df_1}\right) \tag{Equation 7-6}$$

With $df_1 = lq$ and $df_2 = rt - 2u$, where:

$$l = \text{rank}(L)$$

$$q = \text{rank}(C)$$

$$u = \frac{df_1 - 2}{4}$$

$$r = N - q - \frac{df_1 + 1}{2}, \text{ N = sample size}$$

$$t = \begin{cases} \sqrt{\frac{l^2 q^2 - 4}{l^2 + q^2 - 5}} & , l^2 + q^2 - 5 > 0 \\ 1 & , l^2 + q^2 - 5 \leq 0 \end{cases}$$

If $\min(l, q) \leq 2$, the F approximation is exact (Tabachnick and Fidell, 2007). A further point for neuroimaging is that all hypothesis tests in the multivariate GLM framework are based on F-statistics, meaning that it is not possible to test directional (one-tailed) hypotheses.

Canonical Component Analysis (CCA)

Generally, when using MANOVA models, the calculation of a sufficiently large multivariate test statistic naturally leads to the question of the degree to which any of the dependent variables are contributing to the rejection of the null hypothesis. Although it is always possible to simply follow up any significant multivariate tests with

multiple univariate tests, it is not favorable as doing multiple tests would increase the chance of false positives (Gyger et al., 2021; McFarquhar et al., 2016). Linear discriminant analysis (LDA), also called canonical component analysis (CCA) is a more relevant approach for calculation of the MANOVA test statistics (Huberty and Olejnik, 2006).

In our case, when the hypothesis matrix L involves multiple dependent variables, it is of interest to extract the contribution of each dependent variable, also called canonical vector, to the test statistic Λ . This contribution corresponds to the eigenvectors of the eigen decomposition of $SSCP_E^{-1}SSCP_H$. The absolute value of these eigenvectors (canonical vectors) is a measure of contribution for each dependent variate.

7.2 Appendix-B: Supplementary results - Chapter 2

Table 7-1. Pearson's correlations between different maps in AD group with age and gender.

	Pearson's r	p-value	Lower 95% CI	Upper 95% CI	Fisher's z
Left hippocampus					
MTsat – Age	-0.431	0.035	-0.711	-0.034	-0.461
MTsat - Gender	-0.258	0.224	-0.599	0.163	-0.264
R2* - Age	-0.207	0.332	-0.563	0.215	-0.210
R2* - Gender	-0.085	0.693	-0.472	0.330	-0.085
GMvol - Age	-0.173	0.418	-0.539	0.247	-0.175
GMvol - Gender	-0.591	0.002	-0.803	-0.246	-0.679
Vt -Age	-0.253	0.233	-0.596	0.167	-0.259
Vt - Gender	-0.253	0.232	-0.596	0.167	-0.259
Right hippocampus					
MTsat – Age	-0.399	0.053	-0.691	0.005	-0.422
MTsat - Gender	-0.445	0.029	-0.719	-0.051	-0.479
R2* - Age	-0.166	0.439	-0.534	0.255	-0.167
R2* - Gender	-0.127	0.553	-0.505	0.291	-0.128
GMvol - Age	-0.132	0.540	-0.508	0.287	-0.132
GMvol - Gender	-0.385	0.064	-0.682	0.022	-0.405
Vt -Age	-0.298	0.157	-0.626	0.120	-0.307
Vt - Gender	-0.136	0.526	-0.511	0.283	-0.137
Right para hippocampal cortex					
MTsat – Age	-0.283	0.180	-0.616	0.136	-0.291
MTsat - Gender	-0.394	0.057	-0.688	0.012	-0.416
R2* - Age	0.139	0.517	-0.280	0.514	0.140
R2* - Gender	0.376	0.070	-0.032	0.677	0.396
GMvol - Age	-0.416	0.043	-0.702	-0.015	-0.443
GMvol - Gender	-0.537	0.007	-0.773	-0.171	-0.600
Vt -Age	-0.139	0.517	-0.514	0.280	-0.140
Vt - Gender	-0.122	0.570	-0.501	0.296	-0.123
Left fusiform					
MTsat – Age	-0.352	0.091	-0.662	0.060	-0.368
MTsat - Gender	-0.503	0.012	-0.753	-0.125	-0.553
R2* - Age	0.032	0.883	-0.377	0.430	0.032
R2* - Gender	0.406	0.049	0.004	0.696	0.431
GMvol - Age	-0.207	0.333	-0.563	0.215	-0.210
GMvol - Gender	-0.559	0.004	-0.786	-0.202	-0.632
Vt -Age	-0.139	0.516	-0.514	0.280	-0.140
Vt - Gender	-0.428	0.037	-0.709	-0.029	-0.457
Left temporal					

MTsat – Age	-0.631	< .001	-0.824	-0.305	-0.742
MTsat - Gender	-0.395	0.056	-0.689	0.010	-0.418
R2* - Age	-0.070	0.744	-0.461	0.343	-0.070
R2* - Gender	0.189	0.376	-0.232	0.551	0.192
GMvol - Age	-0.343	0.101	-0.656	0.070	-0.357
GMvol - Gender	-0.239	0.261	-0.586	0.182	-0.244
Vt -Age	-0.448	0.028	-0.721	-0.055	-0.482
Vt - Gender	-0.125	0.562	-0.503	0.294	-0.125

Key: CI, confidence interval; MTsat, magnetization transfer saturation; Vt, total volume distribution; R2, effective transverse relaxation rate; GMvol, gray matter volume*

Table 7-2. Pearson's correlations between different maps in the HC group with age and gender.

	Pearson's r	p-value	Lower 95% CI	Upper 95% CI	Fisher's z
Left hippocampus					
MTsat – Age	-0.663	0.002	-0.859	-0.299	-0.798
MTsat - Gender	0.014	0.954	-0.443	0.466	0.014
R2* - Age	-0.266	0.271	-0.643	0.214	-0.273
R2* - Gender	-0.224	0.356	-0.616	0.256	-0.228
GMvol - Age	-0.378	0.111	-0.710	0.092	-0.397
GMvol - Gender	-0.646	0.003	-0.851	-0.272	-0.769
Vt -Age	-0.114	0.642	-0.540	0.359	-0.115
Vt - Gender	0.101	0.680	-0.370	0.531	0.102
Right hippocampus					
MTsat – Age	-0.574	0.010	-0.816	-0.162	-0.654
MTsat - Gender	0.019	0.938	-0.439	0.469	0.019
R2* - Age	-0.243	0.317	-0.628	0.238	-0.248
R2* - Gender	-0.547	0.015	-0.802	-0.124	-0.614
GMvol - Age	-0.709	< .001	-0.880	-0.376	-0.885
GMvol - Gender	-0.401	0.088	-0.724	0.065	-0.425
Vt -Age	-0.163	0.504	-0.575	0.314	-0.165
Vt - Gender	0.055	0.822	-0.409	0.497	0.055
Right para hippocampal cortex					
MTsat – Age	-0.176	0.470	-0.584	0.302	-0.178
MTsat - Gender	-0.168	0.493	-0.578	0.310	-0.169
R2* - Age	-0.207	0.396	-0.604	0.273	-0.210
R2* - Gender	-0.572	0.011	-0.814	-0.159	-0.650
GMvol - Age	-0.530	0.020	-0.793	-0.100	-0.590
GMvol - Gender	-0.501	0.029	-0.778	-0.061	-0.551
Vt -Age	0.013	0.959	-0.444	0.464	0.013
Vt - Gender	0.075	0.760	-0.393	0.512	0.075
Left fusiform					
MTsat – Age	0.094	0.702	-0.376	0.526	0.094
MTsat - Gender	-0.318	0.184	-0.675	0.159	-0.330
R2* - Age	0.117	0.633	-0.356	0.542	0.118
R2* - Gender	-0.540	0.017	-0.798	-0.114	-0.604
GMvol - Age	-0.668	0.002	-0.861	-0.306	-0.806
GMvol - Gender	-0.377	0.112	-0.710	0.094	-0.396
Vt -Age	-0.267	0.269	-0.643	0.213	-0.274
Vt - Gender	0.021	0.933	-0.438	0.470	0.021
Left temporal					
MTsat – Age	-0.352	0.091	-0.662	0.060	-0.368
MTsat - Gender	-0.503	0.012	-0.753	-0.125	-0.553
R2* - Age	0.032	0.883	-0.377	0.430	0.032

R2* - Gender	0.406	0.049	0.004	0.696	0.431
GMvol - Age	-0.207	0.333	-0.563	0.215	-0.210
GMvol - Gender	-0.559	0.004	-0.786	-0.202	-0.632
Vt -Age	-0.139	0.516	-0.514	0.280	-0.140
Vt - Gender	-0.428	0.037	-0.709	-0.029	-0.457

Key: CI, confidence interval; MTsat, magnetization transfer saturation; Vt, total volume distribution; R2*, effective transverse relaxation rate; GMvol, gray matter volume

Table 7-3. Pearson's correlations between different maps in HC group.

	Pearson's r	p-value	Lower 95% CI	Upper 95% CI	Fisher's z	VIF
Left hippocampus						
MTsat – R2*	-0.031	0.899	-0.479	0.429	-0.031	0.999
MTsat - GMvol	-0.082	0.738	-0.517	0.386	-0.082	0.993
MTsat - Vt	0.183	0.453	-0.296	0.588	0.185	1.035
R2* - GMvol	0.538	0.018	0.110	0.797	0.601	1.407
R2* - Vt	0.253	0.297	-0.228	0.634	0.258	1.068
GMvol - Vt	-0.135	0.582	-0.555	0.340	-0.136	0.982
Right hippocampus						
MTsat – R2*	0.144	0.556	-0.332	0.562	0.145	0.979
MTsat - GMvol	0.284	0.238	-0.195	0.654	0.292	0.919
MTsat - Vt	0.300	0.213	-0.179	0.664	0.309	0.910
R2* - GMvol	0.193	0.427	-0.286	0.595	0.196	0.963
R2* - Vt	0.250	0.302	-0.231	0.632	0.255	0.937
GMvol - Vt	-0.022	0.929	-0.472	0.437	-0.022	0.999
Right para hippocampal cortex						
MTsat – R2*	0.324	0.175	-0.152	0.679	0.337	0.895
MTsat - GMvol	0.070	0.775	-0.397	0.508	0.070	0.995
MTsat - Vt	0.170	0.486	-0.308	0.580	0.172	0.971
R2* - GMvol	0.383	0.106	-0.086	0.713	0.404	0.853
R2* - Vt	0.029	0.907	-0.431	0.477	0.029	0.999
GMvol - Vt	0.128	0.601	-0.346	0.550	0.129	0.984
Left fusiform						
MTsat – R2*	0.471	0.042	0.022	0.762	0.512	0.778
MTsat - GMvol	-0.180	0.462	-0.586	0.299	-0.182	0.968
MTsat - Vt	-0.243	0.317	-0.628	0.238	-0.247	0.941
R2* - GMvol	-0.190	0.436	-0.593	0.289	-0.192	0.964
R2* - Vt	-0.215	0.376	-0.610	0.265	-0.219	0.954
GMvol - Vt	0.429	0.067	-0.031	0.739	0.459	0.816
Left temporal						
MTsat – R2*	0.361	0.129	-0.111	0.700	0.378	0.870
MTsat - GMvol	0.144	0.557	-0.332	0.561	0.145	0.979
MTsat - Vt	-0.032	0.895	-0.480	0.428	-0.032	0.999
R2* - GMvol	0.752***	< .001	0.453	0.899	0.978	0.434
R2* - Vt	0.307	0.201	-0.171	0.668	0.317	0.906
GMvol - Vt	0.151	0.536	-0.325	0.567	0.152	0.977

Key: CI, confidence interval; MTsat, magnetization transfer saturation; Vt, total volume distribution; R2*, effective transverse relaxation rate, GMvol, gray matter volume.

Table 7-4. Fisher z-transformation test for correlation coefficients between the HC and AD groups. There is no significant correlation between the coefficients of the groups, and therefore the homogeneity assumption holds for the multivariate model.

	Group AD		Group HC		Fisher's z diff.	p-value of diff.
	Pearson's r	Fisher's z	Pearson's r	Fisher's z		
Left hippocampus						
MTsat – Age	-0.431	-0.461	-0.663	-0.798	0.337	0.736
MTsat - Gender	-0.258	-0.264	0.014	0.014	-0.278	0.781
R2* - Age	-0.207	-0.210	-0.266	-0.273	0.063	0.95
R2* - Gender	-0.085	-0.085	-0.224	-0.228	0.143	0.886
GMvol - Age	-0.173	-0.175	-0.378	-0.397	0.222	0.824
GMvol - Gender	-0.591	-0.679	-0.646	-0.769	0.09	0.929
Vt -Age	-0.253	-0.259	-0.114	-0.115	-0.144	0.885
Vt - Gender	-0.253	-0.259	0.101	0.102	-0.36	0.719
Right hippocampus						
MTsat – Age	-0.399	-0.422	-0.574	-0.654	0.231	0.817
MTsat - Gender	-0.445	-0.479	0.019	0.019	-0.498	0.618
R2* - Age	-0.166	-0.167	-0.243	-0.248	0.08	0.936
R2* - Gender	-0.127	-0.128	-0.547	-0.614	0.486	0.627
GMvol - Age	-0.132	-0.132	-0.709	-0.885	0.752	0.452
GMvol - Gender	-0.385	-0.405	-0.401	-0.425	0.02	0.984
Vt -Age	-0.298	-0.307	-0.163	-0.165	-0.143	0.886
Vt - Gender	-0.136	-0.137	0.055	0.055	-0.192	0.847
Right para hippocampal cortex						
MTsat – Age	-0.283	-0.291	-0.176	-0.178	-0.113	0.91
MTsat - Gender	-0.394	-0.416	-0.168	-0.169	-0.247	0.805
R2* - Age	0.139	0.140	-0.207	-0.210	0.349	0.727
R2* - Gender	0.376	0.396	-0.572	-0.650	1.046	0.296
GMvol - Age	-0.416	-0.443	-0.530	-0.590	0.147	0.883
GMvol - Gender	-0.537	-0.600	-0.501	-0.551	-0.049	0.961
Vt -Age	-0.139	-0.140	0.013	0.013	-0.153	0.879
Vt - Gender	-0.122	-0.123	0.075	0.075	-0.198	0.843
Left fusiform						
MTsat – Age	-0.352	-0.368	0.094	0.094	-0.462	0.644
MTsat - Gender	-0.503	-0.553	-0.318	-0.330	-0.223	0.823
R2* - Age	0.032	0.032	0.117	0.118	-0.086	0.931

R2* - Gender	0.406	0.431	-0.540	-0.604	1.036	0.300
GMvol - Age	-0.207	-0.210	-0.668	-0.806	0.597	0.551
GMvol - Gender	-0.559	-0.632	-0.377	-0.396	-0.236	0.814
Vt -Age	-0.139	-0.140	-0.267	-0.274	0.133	0.894
Vt - Gender	-0.428	-0.457	0.021	0.021	-0.478	0.633

Left temporal

MTsat – Age	-0.631	-0.742	-0.352	-0.368	-0.142	0.887
MTsat - Gender	-0.395	-0.418	-0.503	-0.553	-0.198	0.843
R2* - Age	-0.070	-0.070	0.032	0.032	0.255	0.799
R2* - Gender	0.189	0.192	0.406	0.431	0.366	0.714
GMvol - Age	-0.343	-0.357	-0.207	-0.210	0.121	0.904
GMvol - Gender	-0.239	-0.244	-0.559	-0.632	-0.003	0.998
Vt -Age	-0.448	-0.482	-0.139	-0.140	-0.338	0.735
Vt - Gender	-0.125	-0.125	-0.428	-0.457	-0.35	0.726

Key: MTsat, magnetization transfer saturation; Vt, total volume distribution; R2*, effective transverse relaxation rate; GMvol, gray matter volume; diff, the difference between the Fisher's z of group HC and AD.

7.3 Appendix-C: Supplementary results - Chapter 3

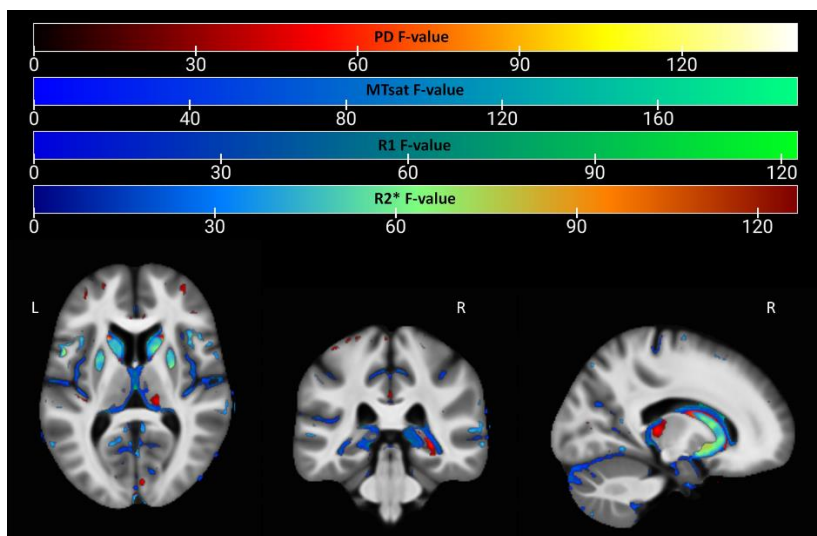


Figure 7-1. Statistical parametric maps for the uGLMs at a corrected threshold of $p < 0.05$ FWER in the GM; showing all the voxels with significant correlation with age, as detected by uGLMs for PD, MTsat, R1, and R2* maps. The F-tests were thresholded at $p < 0.05$ FWER corrected at voxel-level. The SPMs were overlaid on the mean MTsat map for the cohort in the MNI space. Abbreviation: GLM, general linear model; uGLM, univariate GLM; GM, gray matter; FWER, family-wise error rate; SPM, statistical parametric map. These results are previously published in (Callaghan et al., 2014).

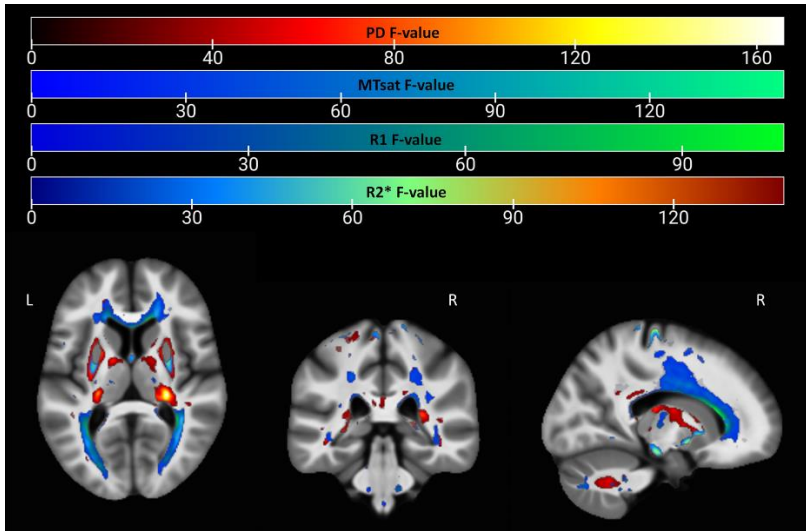


Figure 7-2. Statistical parametric maps for the uGLMs at a corrected threshold of $p < 0.05$ FWER in the WM; showing all the voxels with significant correlation with age, as detected by uGLMs for PD, MTsat, R1, and R2* maps. The F-tests were thresholded at $p < 0.05$ FWER corrected at voxel-level. The SPMs were overlaid on the mean MTsat map for the cohort in the MNI space. Abbreviation: GLM, general linear model, uGLM, univariate GLM, mGLM, multivariate GLM, WM, white matter, FWER, family-wise error, SPM, statistical parametric map. These results are previously published in (Callaghan et al., 2014).

Table 7-5. Canonical vector sizes for different modalities from the mGLM model, representing the contribution of each modality in each voxel. The coordinates correspond to the peak voxels at the selected ROIs.

Left					
ROI name	Peak Coordinate (mm)	PD	MTsat	R1	R2*
Putamen	(-24 5 5)	0.75	-0.39	-0.042	0.5352
Thalamus	(-11 -23 14)	0.981	-0.18	0.067	-0.021
Hippocampus	(-23 -10 -10)	0.985	-0.004	0.048	0.165
Mid-Frontal g	(-6 45 -10)	0.949	0.201	0.236	-0.055
Precentral	(-31 -24 60)	0.834	-0.525	-0.07	0.128
Heschl g	(-35 -26 16)	0.975	0.222	-0.015	-0.005
Supp-motor	(-5 -2 63)	0.668	-0.147	-0.328	0.651
Caudate	(-15 12 8)	0.932	0.202	-0.064	-0.294
Pallidum	(-13 7 -5)	0.953	-0.263	0.148	-0.017
Right					
Putamen	(27 8 2)	0.272	0.515	0.034	-0.814
Thalamus	(09 -19 15)	0.996	0.081	-0.024	0.004
Hippocampus	(31 -35 0)	0.998	0.062	-0.005	-0.006
Mid-Frontal g	(33 1 59)	0.69	-0.196	-0.38	0.583
Precentral	(26 -22 67)	0.734	-0.61	-0.192	0.229
Heschl g	(39 -22 12)	0.983	0.164	-0.078	0.002
Supp-motor	(7 -2 64)	0.584	-0.021	-0.502	0.637
Caudate	(13 09 12)	0.976	-0.019	-0.164	-0.137
Pallidum	(19 5 -5)	0.945	-0.214	-0.044	-0.243

Key: MTsat, magnetization transfer saturation; PD, proton density; R2*, effective transverse relaxation rate; R1, longitudinal relaxation rate.

7.4 Appendix-D: UCB-H PET Automated Pipeline Validation

Apart from the studies presented in this thesis, we have also worked on automatization and validation of a pipeline for processing the SV2-A PET images with $[F^{18}]$ UCB-H radiotracer. A preprint of our work will be available soon. Here you can find the abstract of our presentation at INCF 2023 assembly.

Abstract

Arterial sampling input function (AIF) is the gold standard for quantitative analysis of PET data of the brain. However, the invasive character of arterial sampling limits its widespread use in clinical applications. In the absence of ideal reference region, image-derived input function (IDIF) from carotid arteries appears to be a best non-invasive alternative to the AIF. Earlier, IDIF was demonstrated suitable for $[F^{18}]$ UCB-H kinetic analysis with limited sample size. Therefore, the aims of this study were (1) to validate a fully automated pipeline for the IDIF; (2) to compare the accuracy of measures obtained with AIF to those obtained with IDIF; and (3) to evaluate the use of IDIF for $[18F]$ UCB-H quantification on a larger data set.

Ten healthy subjects underwent a dynamic $[F^{18}]$ UCB-H PET and MRI scans and both (invasive) AIF and (non-invasive) IDIF were obtained.

Successful automatic detection of carotid arteries was performed in 100% of our subjects. The IDIF data showed a significantly larger area under the curve (10%) compared to AIF. Additionally, the total distribution volume maps estimated with IDIF and AIF show no significant difference. Thus, our findings showed that automation of image processing is efficient with increased reproducibility and reliability.

References

- Acosta-Cabronero, J., Betts, M.J., Cardenas-Blanco, A., Yang, S., Nestor, P.J., 2016. *In Vivo* MRI Mapping of Brain Iron Deposition across the Adult Lifespan. *J. Neurosci.* 36, 364–374. <https://doi.org/10.1523/JNEUROSCI.1907-15.2016>
- Acosta-Cabronero, J., Williams, G.B., Cardenas-Blanco, A., Arnold, R.J., Lupson, V., Nestor, P.J., 2013. *In Vivo* Quantitative Susceptibility Mapping (QSM) in Alzheimer's Disease. *PLoS ONE* 8, e81093. <https://doi.org/10.1371/journal.pone.0081093>
- Adam, S., Van der Linden, M., Ivanoiu, A., Juillerat, A.-C., Bechet, S., Salmon, E., 2007. Optimization of encoding specificity for the diagnosis of early AD: the RI-48 task. *J Clin Exp Neuropsychol* 29, 477–487. <https://doi.org/10.1080/13803390600775339>
- Albert, M.S., DeKosky, S.T., Dickson, D., Dubois, B., Feldman, H.H., Fox, N.C., Gamst, A., Holtzman, D.M., Jagust, W.J., Petersen, R.C., Snyder, P.J., Carrillo, M.C., Thies, B., Phelps, C.H., 2011. The diagnosis of mild cognitive impairment due to Alzheimer's disease: recommendations from the National Institute on Aging-Alzheimer's Association workgroups on diagnostic guidelines for Alzheimer's disease. *Alzheimers Dement* 7, 270–279. <https://doi.org/10.1016/j.jalz.2011.03.008>
- Almeida, J., Martins, A.R., Amaral, L., Valério, D., Bukhari, Q., Schu, G., Nogueira, J., Spínola, M., Soleimani, G., Fernandes, F., Silva, A.R., Fregni, F., Simis, M., Simões, M., Peres, A., 2023. The cerebellum is causally involved in episodic memory under aging. *GeroScience*. <https://doi.org/10.1007/s11357-023-00738-0>
- Anand, K.S., Dhikav, V., 2012. Hippocampus in health and disease: An overview. *Ann Indian Acad Neurol* 15, 239–246. <https://doi.org/10.4103/0972-2327.104323>
- Apps, M.A.J., Rushworth, M.F.S., Chang, S.W.C., 2016. The Anterior Cingulate Gyrus and Social Cognition: Tracking the Motivation of Others. *Neuron* 90, 692–707. <https://doi.org/10.1016/j.neuron.2016.04.018>
- Ashburner, J., 2007. A fast diffeomorphic image registration algorithm. *NeuroImage* 38, 95–113. <https://doi.org/10.1016/j.neuroimage.2007.07.007>
- Ashburner, J., Friston, K.J., 2005. Unified segmentation. *NeuroImage* 26, 839–851. <https://doi.org/10.1016/j.neuroimage.2005.02.018>

- Attems, J., Walker, L., Jellinger, K.A., 2015. Olfaction and Aging: A Mini-Review. *Gerontology* 61, 485–490. <https://doi.org/10.1159/000381619>
- Avants, B.B., Libon, D.J., Rascovsky, K., Boller, A., McMillan, C.T., Massimo, L., Coslett, H.B., Chatterjee, A., Gross, R.G., Grossman, M., 2014. Sparse canonical correlation analysis relates network-level atrophy to multivariate cognitive measures in a neurodegenerative population. *Neuroimage* 84, 698–711. <https://doi.org/10.1016/j.neuroimage.2013.09.048>
- Ayton, S., Faux, N.G., Bush, A.I., 2015. Ferritin levels in the cerebrospinal fluid predict Alzheimer's disease outcomes and are regulated by APOE. *Nat Commun* 6, 6760. <https://doi.org/10.1038/ncomms7760>
- Azam, S., Haque, M.E., Balakrishnan, R., Kim, I.-S., Choi, D.-K., 2021. The Ageing Brain: Molecular and Cellular Basis of Neurodegeneration. *Front Cell Dev Biol* 9, 683459. <https://doi.org/10.3389/fcell.2021.683459>
- Bäckman, L., Small, B.J., Fratiglioni, L., 2001. Stability of the preclinical episodic memory deficit in Alzheimer's disease. *Brain* 124, 96–102. <https://doi.org/10.1093/brain/124.1.96>
- Bahri, M.A., Plenevaux, A., Aerts, J., Bastin, C., Becker, G., Mercier, J., Valade, A., Buchanan, T., Mestdagh, N., Ledoux, D., Seret, A., Luxen, A., Salmon, E., 2017. Measuring brain synaptic vesicle protein 2A with positron emission tomography and [18F]UCB-H. *Alzheimer's & Dementia: Translational Research & Clinical Interventions* 3, 481–486. <https://doi.org/10.1016/j.trci.2017.08.004>
- Bajjalieh, S., Frantz, G., Weimann, J., McConnell, S., Scheller, R., 1994. Differential expression of synaptic vesicle protein 2 (SV2) isoforms. *J Neurosci* 14, 5223–5235. <https://doi.org/10.1523/JNEUROSCI.14-09-05223.1994>
- Baker, J.E., Lim, Y.Y., Pietrzak, R.H., Hassenstab, J., Snyder, P.J., Masters, C.L., Maruff, P., 2017. Cognitive impairment and decline in cognitively normal older adults with high amyloid- β : A meta-analysis. *Alzheimers Dement* (Amst) 6, 108–121. <https://doi.org/10.1016/j.dadm.2016.09.002>
- Bakker, R., Tiesinga, P., Kötter, R., 2015. The Scalable Brain Atlas: Instant Web-Based Access to Public Brain Atlases and Related Content. *Neuroinform* 13, 353–366. <https://doi.org/10.1007/s12021-014-9258-x>
- Bartzokis, G., 2011. Alzheimer's disease as homeostatic responses to age-related myelin breakdown. *Neurobiology of Aging* 32, 1341–1371. <https://doi.org/10.1016/j.neurobiolaging.2009.08.007>
- Bartzokis, G., 2004a. Age-related myelin breakdown: a developmental model of cognitive decline and Alzheimer's disease. *Neurobiology of Aging* 25, 5–18. <https://doi.org/10.1016/j.neurobiolaging.2003.03.001>

- Bartzokis, G., 2004b. Quadratic trajectories of brain myelin content: unifying construct for neuropsychiatric disorders. *Neurobiology of Aging* 25, 49–62. <https://doi.org/10.1016/j.neurobiolaging.2003.08.001>
- Bartzokis, G., Sultzer, D., Cummings, J., Holt, L.E., Hance, D.B., Henderson, V.W., Mintz, J., 2000. In Vivo Evaluation of Brain Iron in Alzheimer Disease Using Magnetic Resonance Imaging. *Arch Gen Psychiatry* 57, 47. <https://doi.org/10.1001/archpsyc.57.1.47>
- Bastin, C., Bahri, M.A., Meyer, F., Manard, M., Delhaye, E., Plenevaux, A., Becker, G., Seret, A., Mella, C., Giacomelli, F., Degueldre, C., Baiteau, E., Luxen, A., Salmon, E., 2020. In vivo imaging of synaptic loss in Alzheimer's disease with [18F]UCB-H positron emission tomography. *Eur J Nucl Med Mol Imaging* 47, 390–402. <https://doi.org/10.1007/s00259-019-04461-x>
- Beard, J.R., Officer, A., de Carvalho, I.A., Sadana, R., Pot, A.M., Michel, J.-P., Lloyd-Sherlock, P., Epping-Jordan, J.E., Peeters, G.M.E.E. (Geeske), Mahanani, W.R., Thiyagarajan, J.A., Chatterji, S., 2016. The World report on ageing and health: a policy framework for healthy ageing. *Lancet* 387, 2145–2154. [https://doi.org/10.1016/S0140-6736\(15\)00516-4](https://doi.org/10.1016/S0140-6736(15)00516-4)
- Benes, F.M., Turtle, M., Khan, Y., Farol, P., 1994. Myelination of a Key Relay Zone in the Hippocampal Formation Occurs in the Human Brain During Childhood, Adolescence, and Adulthood. *Archives of General Psychiatry* 51, 477–484. <https://doi.org/10.1001/archpsyc.1994.03950060041004>
- Bettens, K., Sleegers, K., Van Broeckhoven, C., 2013. Genetic insights in Alzheimer's disease. *The Lancet Neurology* 12, 92–104. [https://doi.org/10.1016/S1474-4422\(12\)70259-4](https://doi.org/10.1016/S1474-4422(12)70259-4)
- Beuriat, P.-A., Cohen-Zimmerman, S., Smith, G.N.L., Krueger, F., Gordon, B., Grafman, J., 2020. A New Insight on the Role of the Cerebellum for Executive Functions and Emotion Processing in Adults. *Front Neurol* 11, 593490. <https://doi.org/10.3389/fneur.2020.593490>
- Beuriat, P.-A., Cristofori, I., Gordon, B., Grafman, J., 2022. The shifting role of the cerebellum in executive, emotional and social processing across the lifespan. *Behavioral and Brain Functions* 18, 6. <https://doi.org/10.1186/s12993-022-00193-5>
- Biel, D., Steiger, T.K., Bunzeck, N., 2021. Age-related iron accumulation and demyelination in the basal ganglia are closely related to verbal memory and executive functioning. *Sci Rep* 11, 9438. <https://doi.org/10.1038/s41598-021-88840-1>
- Bilgel, M., An, Y., Helphrey, J., Elkins, W., Gomez, G., Wong, D.F., Davatzikos, C., Ferrucci, L., Resnick, S.M., 2018. Effects of amyloid pathology and

- neurodegeneration on cognitive change in cognitively normal adults. *Brain* 141, 2475–2485. <https://doi.org/10.1093/brain/awy150>
- Bjarnason, T. a., Vavasour, I. m., Chia, C. I. I., MacKay, A. I., 2005. Characterization of the NMR behavior of white matter in bovine brain. *Magnetic Resonance in Medicine* 54, 1072–1081. <https://doi.org/10.1002/mrm.20680>
- Bobinski, M., de Leon, M.J., Wegiel, J., DeSanti, S., Convit, A., Saint Louis, L.A., Rusinek, H., Wisniewski, H.M., 1999. The histological validation of post mortem magnetic resonance imaging-determined hippocampal volume in Alzheimer's disease. *Neuroscience* 95, 721–725. [https://doi.org/10.1016/S0306-4522\(99\)00476-5](https://doi.org/10.1016/S0306-4522(99)00476-5)
- Braak, E., Griffing, K., Arai, K., Bohl, J., Bratzke, H., Braak, H., 1999. Neuropathology of Alzheimer's disease: what is new since A. Alzheimer? *European Archives of Psychiatry and Clinical Neurosciences* 249, S14–S22. <https://doi.org/10.1007/PL00014168>
- Braak, H., Braak, E., 1999. Temporal Sequence of Alzheimer's Disease-Related Pathology, in: Peters, A., Morrison, J.H. (Eds.), *Cerebral Cortex: Neurodegenerative and Age-Related Changes in Structure and Function of Cerebral Cortex*, Cerebral Cortex. Springer US, Boston, MA, pp. 475–512. https://doi.org/10.1007/978-1-4615-4885-0_14
- Braak, H., Braak, E., 1991. Neuropathological staging of Alzheimer-related changes. *Acta Neuropathol* 82, 239–259. <https://doi.org/10.1007/BF00308809>
- Braskie, M.N., Medina, L.D., Rodriguez-Agudelo, Y., Geschwind, D.H., Macias-Islas, M.A., Cummings, J.L., Bookheimer, S.Y., Ringman, J.M., 2012. Increased fMRI signal with age in familial Alzheimer's disease mutation carriers. *Neurobiology of aging* 33, 424.e11. <https://doi.org/10.1016/j.neurobiolaging.2010.09.028>
- Braskie, M.N., Medina, L.D., Rodriguez-Agudelo, Y., Geschwind, D.H., Macias-Islas, M.A., Thompson, P.M., Cummings, J.L., Bookheimer, S.Y., Ringman, J.M., 2013. Memory performance and fMRI signal in presymptomatic familial Alzheimer's disease. *Hum Brain Mapp* 34, 3308–3319. <https://doi.org/10.1002/hbm.22141>
- Bretin, F., Warnock, G., Bahri, M.A., Aerts, J., Mestdagh, N., Buchanan, T., Valade, A., Mievis, F., Giacomelli, F., Lemaire, C., Luxen, A., Salmon, E., Seret, A., Plenevaux, A., 2013. Preclinical radiation dosimetry for the novel SV2A radiotracer [18F]UCB-H. *EJNMMI Res* 3, 35. <https://doi.org/10.1186/2191-219X-3-35>

- Bryan, J., Luszcz, M.A., 2000. Measures of fluency as predictors of incidental memory among older adults. *Psychology and Aging* 15, 483–489. <https://doi.org/10.1037/0882-7974.15.3.483>
- Buckner, R.L., Snyder, A.Z., Shannon, B.J., LaRossa, G., Sachs, R., Fotenos, A.F., Sheline, Y.I., Klunk, W.E., Mathis, C.A., Morris, J.C., Mintun, M.A., 2005. Molecular, Structural, and Functional Characterization of Alzheimer's Disease: Evidence for a Relationship between Default Activity, Amyloid, and Memory. *J Neurosci* 25, 7709–7717. <https://doi.org/10.1523/JNEUROSCI.2177-05.2005>
- Bulk, M., Abdelmoula, W.M., Nabuurs, R.J.A., van der Graaf, L.M., Mulders, C.W.H., Mulder, A.A., Jost, C.R., Koster, A.J., van Buchem, M.A., Natté, R., Dijkstra, J., van der Weerd, L., 2018. Postmortem MRI and histology demonstrate differential iron accumulation and cortical myelin organization in early- and late-onset Alzheimer's disease. *Neurobiology of Aging* 62, 231–242. <https://doi.org/10.1016/j.neurobiolaging.2017.10.017>
- Calabrò, M., Rinaldi, C., Santoro, G., Crisafulli, C., 2020. The biological pathways of Alzheimer disease: a review. *AIMS Neurosci* 8, 86–132. <https://doi.org/10.3934/Neuroscience.2021005>
- Calabrò, M., Rinaldi, C., Santoro, G., Crisafulli, C., Department of Biomedical and Dental Sciences and Morphofunctional Imaging, University of Messina, Italy, 2021. The biological pathways of Alzheimer disease: a review. *AIMS Neuroscience* 8, 86–132. <https://doi.org/10.3934/Neuroscience.2021005>
- Callaghan, M.F., Freund, P., Draganski, B., Anderson, E., Cappelletti, M., Chowdhury, R., Diedrichsen, J., FitzGerald, T.H.B., Smittenaar, P., Helms, G., Lutti, A., Weiskopf, N., 2014. Widespread age-related differences in the human brain microstructure revealed by quantitative magnetic resonance imaging. *Neurobiology of Aging* 35, 1862–1872. <https://doi.org/10.1016/j.neurobiolaging.2014.02.008>
- Castello, M.A., Soriano, S., 2014. On the origin of Alzheimer's disease. *Trials and tribulations of the amyloid hypothesis. Ageing Research Reviews* 13, 10–12. <https://doi.org/10.1016/j.arr.2013.10.001>
- Cavanna, A.E., Trimble, M.R., 2006. The precuneus: a review of its functional anatomy and behavioural correlates. *Brain* 129, 564–583. <https://doi.org/10.1093/brain/awl004>
- Cercignani, M., Dowell, N.G., Tofts, P.S., 2021. *Quantitative MRI of the Brain: Principles of Physical Measurement*, Second edition [WWW Document]. Routledge & CRC Press. URL <https://www.routledge.com/Quantitative-MRI-of-the-Brain-Principles-of-Physical-Measurement-Second/Cercignani-Dowell-Tofts/p/book/9780367781538> (accessed 6.8.23).

- Chen, G., Adleman, N.E., Saad, Z.S., Leibenluft, E., Cox, R.W., 2014. Applications of multivariate modeling to neuroimaging group analysis: A comprehensive alternative to univariate general linear model. *NeuroImage* 99, 571–588. <https://doi.org/10.1016/j.neuroimage.2014.06.027>
- Chen, J.-F., 2021. Enhancing myelin renewal reverses cognitive dysfunction in a murine model of Alzheimer's disease. *Neuron*.
- Chen, L., Soldan, A., Oishi, K., Faria, A., Zhu, Y., Albert, M., van Zijl, P.C.M., Li, X., 2021. Quantitative Susceptibility Mapping of Brain Iron and β -Amyloid in MRI and PET Relating to Cognitive Performance in Cognitively Normal Older Adults. *Radiology* 298, 353–362. <https://doi.org/10.1148/radiol.2020201603>
- Chen, M.-K., Mecca, A.P., Naganawa, M., Finnema, S.J., Toyonaga, T., Lin, S., Najafzadeh, S., Ropchan, J., Lu, Y., McDonald, J.W., Michalak, H.R., Nabulsi, N.B., Arnsten, A.F.T., Huang, Y., Carson, R.E., van Dyck, C.H., 2018. Assessing Synaptic Density in Alzheimer Disease With Synaptic Vesicle Glycoprotein 2A Positron Emission Tomographic Imaging. *JAMA Neurol* 75, 1215. <https://doi.org/10.1001/jamaneurol.2018.1836>
- Chen, M.-K., Mecca, A.P., Naganawa, M., Gallezot, J.-D., Toyonaga, T., Mondal, J., Finnema, S.J., Lin, S.-F., O'Dell, R.S., McDonald, J.W., Michalak, H.R., Vander Wyk, B., Nabulsi, N.B., Huang, Y., Arnsten, A.F., van Dyck, C.H., Carson, R.E., 2021. Comparison of [11C]UCB-J and [18F]FDG PET in Alzheimer's disease: A tracer kinetic modeling study. *J Cereb Blood Flow Metab* 41, 2395–2409. <https://doi.org/10.1177/0271678X211004312>
- Cheng, C., Yang, C., Jia, C., Wang, Q., 2023. The Role of Cerebellum in Alzheimer's Disease: A Forgotten Research Corner. *JAD* 95, 75–78. <https://doi.org/10.3233/JAD-230381>
- Chiao, P., Bedell, B.J., Avants, B., Zijdenbos, A.P., Grand'Maison, M., O'Neill, P., O'Gorman, J., Chen, T., Koeppe, R., 2019. Impact of Reference and Target Region Selection on Amyloid PET SUV Ratios in the Phase 1b PRIME Study of Aducanumab. *Journal of Nuclear Medicine* 60, 100–106. <https://doi.org/10.2967/jnumed.118.209130>
- Christensen, H., Mackinnon, A.J., Korten, A.E., Jorm, A.F., Henderson, A.S., Jacomb, P., Rodgers, B., 1999. An Analysis of Diversity in the Cognitive Performance of Elderly Community Dwellers: Individual Differences in Change Scores as a Function of Age. *Psychology and Aging* 14, 365–376.
- Christensen, R., 2020. *Plane Answers to Complex Questions, The Theory of Linear Models*, 5th edition. ed. Springer.
- Chylinski, D., Van Egroo, M., Narbutas, J., Muto, V., Bahri, M.A., Berthomier, C., Salmon, E., Bastin, C., Phillips, C., Collette, F., Maquet, P., Carrier, J., Lina, J.-

- M., Vandewalle, G., 2022. Timely coupling of sleep spindles and slow waves linked to early amyloid- β burden and predicts memory decline. *eLife* 11, e78191. <https://doi.org/10.7554/eLife.78191>
- Corey-Bloom, J., 2002. The ABC of Alzheimer's disease: cognitive changes and their management in Alzheimer's disease and related dementias. *Int Psychogeriatr* 14 Suppl 1, 51–75. <https://doi.org/10.1017/s1041610203008664>
- Correia, S., Ahern, D.C., Rabinowitz, A.R., Farrer, T.J., Smith Watts, A.K., Salloway, S., Malloy, P.F., Deoni, S.C.L., 2015. Lowering the Floor on Trail Making Test Part B: Psychometric Evidence for a New Scoring Metric. *Archives of Clinical Neuropsychology* 30, 643–656. <https://doi.org/10.1093/arclin/acv040>
- Corrigan, N.M., Yarnykh, V.L., Hippe, D.S., Owen, J.P., Huber, E., Zhao, T.C., Kuhl, P.K., 2021. Myelin development in cerebral gray and white matter during adolescence and late childhood. *Neuroimage* 227, 117678. <https://doi.org/10.1016/j.neuroimage.2020.117678>
- Cristóvão, J.S., Santos, R., Gomes, C.M., 2016. Metals and Neuronal Metal Binding Proteins Implicated in Alzheimer's Disease. *Oxid Med Cell Longev* 2016, 9812178. <https://doi.org/10.1155/2016/9812178>
- Darnai, G., Nagy, S.A., Horváth, R., Ács, P., Perlaki, G., Orsi, G., Kovács, N., Altbäcker, A., Plózer, E., Tényi, D., Weintraut, R., Schwarcz, A., John, F., Varga, E., Bereczkei, T., Clemens, Z., Komoly, S., Janszky, J., 2017. Iron Concentration in Deep Gray Matter Structures is Associated with Worse Visual Memory Performance in Healthy Young Adults. *JAD* 59, 675–681. <https://doi.org/10.3233/JAD-170118>
- Davis, C.S., 2002. *Statistical Methods for the Analysis of Repeated Measurements*. Springer New York.
- de los Monteros, A.E., Korsak, R.A., Tran, T., Vu, D., de Vellis, J., Edmond, J., 2000. Dietary iron and the integrity of the developing rat brain: a study with the artificially-reared rat pup. *Cell Mol Biol (Noisy-le-grand)* 46, 501–515.
- Dean, D.C., Hurley, S.A., Kecskemeti, S.R., O'Grady, J.P., Canda, C., Davenport-Sis, N.J., Carlsson, C.M., Zetterberg, H., Blennow, K., Asthana, S., Sager, M.A., Johnson, S.C., Alexander, A.L., Bendlin, B.B., 2017. Association of Amyloid Pathology With Myelin Alteration in Preclinical Alzheimer Disease. *JAMA Neurol* 74, 41–49. <https://doi.org/10.1001/jamaneurol.2016.3232>
- DeKosky, S.T., Scheff, S.W., 1990. Synapse loss in frontal cortex biopsies in Alzheimer's disease: correlation with cognitive severity. *Ann Neurol* 27, 457–464. <https://doi.org/10.1002/ana.410270502>

- Dhakar, S., Macreadie, I., 2020. Protein Homeostasis Networks and the Use of Yeast to Guide Interventions in Alzheimer's Disease. *Int J Mol Sci* 21, 8014. <https://doi.org/10.3390/ijms21218014>
- Dintica, C.S., Marseglia, A., Rizzuto, D., Wang, R., Seubert, J., Arfanakis, K., Bennett, D.A., Xu, W., 2019. Impaired olfaction is associated with cognitive decline and neurodegeneration in the brain. *Neurology* 92, e700–e709. <https://doi.org/10.1212/WNL.0000000000006919>
- Donohue, M.C., Sperling, R.A., Salmon, D.P., Rentz, D.M., Raman, R., Thomas, R.G., Weiner, M., Aisen, P.S., 2014. The Preclinical Alzheimer Cognitive Composite: Measuring Amyloid-Related Decline. *JAMA Neurol* 71, 961. <https://doi.org/10.1001/jamaneurol.2014.803>
- Drachman, D.A., 2014. The amyloid hypothesis, time to move on: Amyloid is the downstream result, not cause, of Alzheimer's disease. *Alzheimer's & Dementia* 10, 372–380. <https://doi.org/10.1016/j.jalz.2013.11.003>
- Draganski, B., Ashburner, J., Hutton, C., Kherif, F., Frackowiak, R.S.J., Helms, G., Weiskopf, N., 2011. Regional specificity of MRI contrast parameter changes in normal ageing revealed by voxel-based quantification (VBQ). *NeuroImage* 55, 1423–1434. <https://doi.org/10.1016/j.neuroimage.2011.01.052>
- Dubois, B., Feldman, H.H., Jacova, C., DeKosky, S.T., Barberger-Gateau, P., Cummings, J., Delacourte, A., Galasko, D., Gauthier, S., Jicha, G., Meguro, K., O'Brien, J., Pasquier, F., Robert, P., Rossor, M., Salloway, S., Stern, Y., Visser, P.J., Scheltens, P., 2007. Research criteria for the diagnosis of Alzheimer's disease: revising the NINCDS–ADRDA criteria. *The Lancet Neurology* 6, 734–746. [https://doi.org/10.1016/S1474-4422\(07\)70178-3](https://doi.org/10.1016/S1474-4422(07)70178-3)
- Dubois, B., Feldman, H.H., Jacova, C., Hampel, H., Molinuevo, J.L., Blennow, K., DeKosky, S.T., Gauthier, S., Selkoe, D., Bateman, R., Cappa, S., Crutch, S., Engelborghs, S., Frisoni, G.B., Fox, N.C., Galasko, D., Habert, M.-O., Jicha, G.A., Nordberg, A., Pasquier, F., Rabinovici, G., Robert, P., Rowe, C., Salloway, S., Sarazin, M., Epelbaum, S., de Souza, L.C., Vellas, B., Visser, P.J., Schneider, L., Stern, Y., Scheltens, P., Cummings, J.L., 2014. Advancing research diagnostic criteria for Alzheimer's disease: the IWG-2 criteria. *Lancet Neurol* 13, 614–629. [https://doi.org/10.1016/S1474-4422\(14\)70090-0](https://doi.org/10.1016/S1474-4422(14)70090-0)
- Duijn, S.V., 2017. Cortical Iron Reflects Severity of Alzheimer's Disease. *J. Alzheimers Dis.*
- Duong, S., Patel, T., Chang, F., 2017. Dementia. *Can Pharm J (Ott)* 150, 118–129. <https://doi.org/10.1177/1715163517690745>

- Dyrba, M., Grothe, M.J., Mohammadi, A., Binder, H., Kirste, T., Teipel, S.J., 2018. Comparison of Different Hypotheses Regarding the Spread of Alzheimer's Disease Using Markov Random Fields and Multimodal Imaging. *JAD* 65, 731–746. <https://doi.org/10.3233/JAD-161197>
- Elobeid, A., Libard, S., Leino, M., Popova, S.N., Alafuzoff, I., 2016. Altered Proteins in the Aging Brain. *J Neuropathol Exp Neurol* 75, 316–325. <https://doi.org/10.1093/jnen/nlw002>
- Erb, G.L., Osterbur, D.L., LeVine, S.M., 1996. The distribution of iron in the brain: a phylogenetic analysis using iron histochemistry. *Brain Res Dev Brain Res* 93, 120–128. [https://doi.org/10.1016/0165-3806\(96\)00020-x](https://doi.org/10.1016/0165-3806(96)00020-x)
- Estrada, S., Lubberink, M., Thibblin, A., Sprycha, M., Buchanan, T., Mestdagh, N., Kenda, B., Mercier, J., Provins, L., Gillard, M., Tytgat, D., Antoni, G., 2016. [11C]UCB-A, a novel PET tracer for synaptic vesicle protein 2A. *Nuclear Medicine and Biology* 43, 325–332. <https://doi.org/10.1016/j.nucmedbio.2016.03.004>
- Falahati, F., Ferreira, D., Muehlboeck, J.-S., Eriksdotter, M., Simmons, A., Wahlund, L.-O., Westman, E., 2017. Monitoring disease progression in mild cognitive impairment: Associations between atrophy patterns, cognition, APOE and amyloid. *NeuroImage: Clinical* 16, 418–428. <https://doi.org/10.1016/j.nicl.2017.08.014>
- Fandakova, Y., Sander, M.C., Werkle-Bergner, M., Shing, Y.L., 2014. Age differences in short-term memory binding are related to working memory performance across the lifespan. *Psychology and Aging* 29, 140–149. <https://doi.org/10.1037/a0035347>
- Ficiarà, E., Stura, I., Guiot, C., 2022. Iron Deposition in Brain: Does Aging Matter? *International Journal of Molecular Sciences* 23, 10018. <https://doi.org/10.3390/ijms231710018>
- Fields, R.D., 2008. White matter in learning, cognition and psychiatric disorders. *Trends Neurosci* 31, 361–370. <https://doi.org/10.1016/j.tins.2008.04.001>
- Fliessbach, K., Trautner, P., Quesada, C.M., Elger, C.E., Weber, B., 2007. Cerebellar contributions to episodic memory encoding as revealed by fMRI. *NeuroImage* 35, 1330–1337. <https://doi.org/10.1016/j.neuroimage.2007.02.004>
- Fox, J., Fox, J., 2016. Applied regression analysis and generalized linear models, Third Edition. ed. SAGE, Los Angeles.
- Gamblin, T.C., King, M.E., Kuret, J., Berry, R.W., Binder, L.I., 2000. Oxidative Regulation of Fatty Acid-Induced Tau Polymerization. *Biochemistry* 39, 14203–14210. <https://doi.org/10.1021/bi001876l>

- Gelman, N., Ewing, J.R., Gorell, J.M., Spickler, E.M., Solomon, E.G., 2001. Interregional variation of longitudinal relaxation rates in human brain at 3.0 T: Relation to estimated iron and water contents. *Magnetic Resonance in Medicine* 45, 71–79. [https://doi.org/10.1002/1522-2594\(200101\)45:1<71::AID-MRM1011>3.0.CO;2-2](https://doi.org/10.1002/1522-2594(200101)45:1<71::AID-MRM1011>3.0.CO;2-2)
- Goedert, M., Spillantini, M.G., Jakes, R., Rutherford, D., Crowther, R.A., 1989. Multiple isoforms of human microtubule-associated protein tau: sequences and localization in neurofibrillary tangles of Alzheimer's disease. *Neuron* 3, 519–526. [https://doi.org/10.1016/0896-6273\(89\)90210-9](https://doi.org/10.1016/0896-6273(89)90210-9)
- Gogolla, N., 2017. The insular cortex. *Current Biology* 27, R580–R586. <https://doi.org/10.1016/j.cub.2017.05.010>
- Gonneaud, J., Chételat, G., 2018. Which is to blame for cognitive decline in ageing: amyloid deposition, neurodegeneration or both? *Brain* 141, 2237–2241. <https://doi.org/10.1093/brain/awy174>
- Good, C.D., Johnsrude, I.S., Ashburner, J., Henson, R.N.A., Friston, K.J., Frackowiak, R.S.J., 2001. A Voxel-Based Morphometric Study of Ageing in 465 Normal Adult Human Brains. *NeuroImage* 14, 21–36. <https://doi.org/10.1006/nimg.2001.0786>
- Gorgolewski, K.J., Auer, T., Calhoun, V.D., Craddock, R.C., Das, S., Duff, E.P., Flandin, G., Ghosh, S.S., Glatard, T., Halchenko, Y.O., Handwerker, D.A., Hanke, M., Keator, D., Li, X., Michael, Z., Maumet, C., Nichols, B.N., Nichols, T.E., Pellman, J., Poline, J.-B., Rokem, A., Schaefer, G., Sochat, V., Triplett, W., Turner, J.A., Varoquaux, G., Poldrack, R.A., 2016. The brain imaging data structure, a format for organizing and describing outputs of neuroimaging experiments. *Sci Data* 3, 160044. <https://doi.org/10.1038/sdata.2016.44>
- Gracien, R.-M., Maiworm, M., Brüche, N., Shrestha, M., Nöth, U., Hattingen, E., Wagner, M., Deichmann, R., 2020. How stable is quantitative MRI? – Assessment of intra- and inter-scanner-model reproducibility using identical acquisition sequences and data analysis programs. *NeuroImage* 207, 116364. <https://doi.org/10.1016/j.neuroimage.2019.116364>
- Grober, E., Ocepek-Welickson, K., Teresi, J., 2009. The Free and Cued Selective Reminding Test: evidence of psychometric adequacy. *Psychology Science Quarterly* 51.
- Gronwall, D.M.A., Sampson, H., 1974. The psychological effects of concussion. Auckland University Press ; Oxford University Press, Auckland, N.Z.], [Wellington, N.Z.
- Grothe, M.J., Heinsen, H., Amaro, E., Grinberg, L.T., Teipel, S.J., 2016. Cognitive Correlates of Basal Forebrain Atrophy and Associated Cortical

- Hypometabolism in Mild Cognitive Impairment. *Cereb Cortex* 26, 2411–2426. <https://doi.org/10.1093/cercor/bhv062>
- Gulisano, W., Maugeri, D., Baltrons, M.A., Fà, M., Amato, A., Palmeri, A., D’Adamio, L., Grassi, C., Devanand, D.P., Honig, L.S., Puzzo, D., Arancio, O., 2018. Role of Amyloid- β and Tau Proteins in Alzheimer’s Disease: Confuting the Amyloid Cascade. *JAD* 64, S611–S631. <https://doi.org/10.3233/JAD-179935>
- Gyger, L., Ramponi, C., Mall, J.F., Swierkosz-Lenart, K., Stoyanov, D., Lutti, A., von Gunten, A., Kherif, F., Draganski, B., 2021. Temporal trajectory of brain tissue property changes induced by electroconvulsive therapy. *NeuroImage* 232, 117895. <https://doi.org/10.1016/j.neuroimage.2021.117895>
- Hagiwara, A., Fujimoto, K., Kamagata, K., Murata, S., Irie, R., Kaga, H., Someya, Y., Andica, C., Fujita, S., Kato, S., Fukunaga, I., Wada, A., Hori, M., Tamura, Y., Kawamori, R., Watada, H., Aoki, S., 2021. Age-Related Changes in Relaxation Times, Proton Density, Myelin, and Tissue Volumes in Adult Brain Analyzed by 2-Dimensional Quantitative Synthetic Magnetic Resonance Imaging. *Invest Radiol* 56, 163–172. <https://doi.org/10.1097/RLI.0000000000000720>
- Hallbeck, Ma., 2013. Neuron-to-Neuron Transmission of Neurodegenerative Pathology [WWW Document]. URL https://journals.sagepub.com/doi/10.1177/1073858413494270?url_ver=Z39.88-2003&rfr_id=ori:rid:crossref.org&rfr_dat=cr_pub%20%200pubmed (accessed 8.30.23).
- Hallgren, B., Sourander, P., 1958. THE EFFECT OF AGE ON THE NON-HAEMIN IRON IN THE HUMAN BRAIN. *J Neurochem* 3, 41–51. <https://doi.org/10.1111/j.1471-4159.1958.tb12607.x>
- Hardy, J., Allsop, D., 1991. Amyloid deposition as the central event in the aetiology of Alzheimer’s disease. *Trends in Pharmacological Sciences* 12, 383–388. [https://doi.org/10.1016/0165-6147\(91\)90609-V](https://doi.org/10.1016/0165-6147(91)90609-V)
- Hardy, J.A., Higgins, G.A., 1992. Alzheimer’s Disease: The Amyloid Cascade Hypothesis. *Science* 256, 184–185. <https://doi.org/10.1126/science.1566067>
- Hayes, S.M., Ryan, L., Schnyer, D.M., Nadel, L., 2004. An fMRI Study of Episodic Memory: Retrieval of Object, Spatial, and Temporal Information. *Behav Neurosci* 118, 885–896. <https://doi.org/10.1037/0735-7044.118.5.885>
- Helms, G., Dathe, H., Dechent, P., 2010. Modeling the influence of TR and excitation flip angle on the magnetization transfer ratio (MTR) in human brain obtained from 3D spoiled gradient echo MRI. *Magnetic Resonance in Medicine* 64, 177–185. <https://doi.org/10.1002/mrm.22379>

- Helms, G., Dechent, P., 2009. Increased SNR and reduced distortions by averaging multiple gradient echo signals in 3D FLASH imaging of the human brain at 3T. *J Magn Reson Imaging* 29, 198–204. <https://doi.org/10.1002/jmri.21629>
- Helms, G., Draganski, B., Frackowiak, R., Ashburner, J., Weiskopf, N., 2009. Improved segmentation of deep brain grey matter structures using magnetization transfer (MT) parameter maps. *NeuroImage* 47, 194–198. <https://doi.org/10.1016/j.neuroimage.2009.03.053>
- Henkelman, R.M., Stanisz, G.J., Graham, S.J., 2001. Magnetization transfer in MRI: a review. *NMR Biomed.* 14, 57–64. <https://doi.org/10.1002/nbm.683>
- Hotelling, H., 1951. A generalized T test and measure of multivariate dispersion. *Proceedings of the Second Berkeley Symposium on Mathematical Statistics and Probability* 23–41.
- Hou, Y., Dan, X., Babbar, M., Wei, Y., Hasselbalch, S.G., Croteau, D.L., Bohr, V.A., 2019. Ageing as a risk factor for neurodegenerative disease. *Nat Rev Neurol* 15, 565–581. <https://doi.org/10.1038/s41582-019-0244-7>
- House, M.J., St. Pierre, T.G., McLean, C., 2008. 1.4T study of proton magnetic relaxation rates, iron concentrations, and plaque burden in Alzheimer’s disease and control postmortem brain tissue: Proton Magnetic Relaxation Rates in AD. *Magn. Reson. Med.* 60, 41–52. <https://doi.org/10.1002/mrm.21586>
- Huberty, C.J., Olejnik, S., 2006. *Applied MANOVA and Discriminant Analysis*. John Wiley & Sons.
- Jack, C.R., Bennett, D.A., Blennow, K., Carrillo, M.C., Dunn, B., Haeberlein, S.B., Holtzman, D.M., Jagust, W., Jessen, F., Karlawish, J., Liu, E., Molinuevo, J.L., Montine, T., Phelps, C., Rankin, K.P., Rowe, C.C., Scheltens, P., Siemers, E., Snyder, H.M., Sperling, R., Contributors, Elliott, C., Masliah, E., Ryan, L., Silverberg, N., 2018. NIA-AA Research Framework: Toward a biological definition of Alzheimer’s disease. *Alzheimer’s & Dementia* 14, 535–562. <https://doi.org/10.1016/j.jalz.2018.02.018>
- Jack, C.R., Dickson, D.W., Parisi, J.E., Xu, Y.C., Cha, R.H., O’Brien, P.C., Edland, S.D., Smith, G.E., Boeve, B.F., Tangalos, E.G., Kokmen, E., Petersen, R.C., 2002. Antemortem MRI Findings Correlate with Hippocampal Neuropathology in Typical Aging and Dementia. *Neurology* 58, 750–757.
- Jack, Clifford R, Knopman, D.S., Jagust, W.J., Petersen, R.C., Weiner, M.W., Aisen, P.S., Shaw, L.M., Vemuri, P., Wiste, H.J., Weigand, S.D., Lesnick, T.G., Pankratz, V.S., Donohue, M.C., Trojanowski, J.Q., 2013. Tracking pathophysiological processes in Alzheimer’s disease: an updated

- hypothetical model of dynamic biomarkers. *The Lancet Neurology* 12, 207–216. [https://doi.org/10.1016/S1474-4422\(12\)70291-0](https://doi.org/10.1016/S1474-4422(12)70291-0)
- Jack, Clifford R., Knopman, D.S., Jagust, W.J., Petersen, R.C., Weiner, M.W., Aisen, P.S., Shaw, L.M., Vemuri, P., Wiste, H.J., Weigand, S.D., Lesnick, T.G., Pankratz, V.S., Donohue, M.C., Trojanowski, J.Q., 2013. Tracking pathophysiological processes in Alzheimer's disease: an updated hypothetical model of dynamic biomarkers. *Lancet Neurol* 12, 207–216. [https://doi.org/10.1016/S1474-4422\(12\)70291-0](https://doi.org/10.1016/S1474-4422(12)70291-0)
- Jack, C.R., Knopman, D.S., Jagust, W.J., Shaw, L.M., Aisen, P.S., Weiner, M.W., Petersen, R.C., Trojanowski, J.Q., 2010. Hypothetical model of dynamic biomarkers of the Alzheimer's pathological cascade. *The Lancet Neurology* 9, 119–128. [https://doi.org/10.1016/S1474-4422\(09\)70299-6](https://doi.org/10.1016/S1474-4422(09)70299-6)
- Jack, C.R., Wiste, H.J., Knopman, D.S., Vemuri, P., Mielke, M.M., Weigand, S.D., Senjem, M.L., Gunter, J.L., Lowe, V., Gregg, B.E., Pankratz, V.S., Petersen, R.C., 2014. Rates of β -amyloid accumulation are independent of hippocampal neurodegeneration. *Neurology* 82, 1605–1612. <https://doi.org/10.1212/WNL.0000000000000386>
- Jack, C.R., Wiste, H.J., Weigand, S.D., Therneau, T.M., Lowe, V.J., Knopman, D.S., Gunter, J.L., Senjem, M.L., Jones, D.T., Kantarci, K., Machulda, M.M., Mielke, M.M., Roberts, R.O., Vemuri, P., Reyes, D.A., Petersen, R.C., 2017. Defining imaging biomarker cut points for brain aging and Alzheimer's disease. *Alzheimer's & Dementia* 13, 205–216. <https://doi.org/10.1016/j.jalz.2016.08.005>
- Jacobs, H.I.L., Hopkins, D.A., Mayrhofer, H.C., Bruner, E., van Leeuwen, F.W., Raaijmakers, W., Schmahmann, J.D., 2018. The cerebellum in Alzheimer's disease: evaluating its role in cognitive decline. *Brain* 141, 37–47. <https://doi.org/10.1093/brain/awx194>
- Jeremic, D., Jiménez-Díaz, L., Navarro-López, J.D., 2021. Past, present and future of therapeutic strategies against amyloid- β peptides in Alzheimer's disease: a systematic review. *Ageing Res Rev* 72, 101496. <https://doi.org/10.1016/j.arr.2021.101496>
- Jernigan, T.L., Archibald, S.L., Fennema-Notestine, C., Gamst, A.C., Stout, J.C., Bonner, J., Hesselink, J.R., 2001. Effects of age on tissues and regions of the cerebrum and cerebellum. *Neurobiology of Aging* 22, 581–594. [https://doi.org/10.1016/S0197-4580\(01\)00217-2](https://doi.org/10.1016/S0197-4580(01)00217-2)
- Josephs, K.A., Whitwell, J.L., Ahmed, Z., Shiung, M.M., Weigand, S.D., Knopman, D.S., Boeve, B.F., Parisi, J.E., Petersen, R.C., Dickson, D.W., Jack, C.R., 2008. Beta-amyloid burden is not associated with rates of brain atrophy. *Ann Neurol* 63, 204–212. <https://doi.org/10.1002/ana.21223>

- Kalpouzos, G., Garzón, B., Sitnikov, R., Heiland, C., Salami, A., Persson, J., Bäckman, L., 2017. Higher Striatal Iron Concentration is Linked to Frontostriatal Underactivation and Poorer Memory in Normal Aging. *Cerebral Cortex* 27, 3427–3436. <https://doi.org/10.1093/cercor/bhx045>
- Kalpouzos, G., Mangialasche, F., Falahati, F., Laukka, E.J., Papenberg, G., 2021. Contributions of HFE polymorphisms to brain and blood iron load, and their links to cognitive and motor function in healthy adults. *Neuropsychopharmacology Reports* 41, 393–404. <https://doi.org/10.1002/npr2.12197>
- Karakuzu, A., Appelhoff, S., Auer, T., Boudreau, M., Feingold, F., Khan, A.R., Lazari, A., Markiewicz, C., Mulder, M., Phillips, C., Salo, T., Stikov, N., Whitaker, K., de Hollander, G., 2022. qMRI-BIDS: An extension to the brain imaging data structure for quantitative magnetic resonance imaging data. *Sci Data* 9, 517. <https://doi.org/10.1038/s41597-022-01571-4>
- Khattar, N., Triebswetter, C., Kiely, M., Ferrucci, L., Resnick, S.M., Spencer, R.G., Bouhrara, M., 2021. Investigation of the association between cerebral iron content and myelin content in normative aging using quantitative magnetic resonance neuroimaging. *NeuroImage* 239, 118267. <https://doi.org/10.1016/j.neuroimage.2021.118267>
- Knudsen, G.M., Ganz, M., Appelhoff, S., Boellaard, R., Bormans, G., Carson, R.E., Catana, C., Doudet, D., Gee, A.D., Greve, D.N., Gunn, R.N., Halldin, C., Herscovitch, P., Huang, H., Keller, S.H., Lammertsma, A.A., Lanzenberger, R., Liow, J.-S., Lohith, T.G., Lubberink, M., Lyoo, C.H., Mann, J.J., Matheson, G.J., Nichols, T.E., Nørgaard, M., Ogden, T., Parsey, R., Pike, V.W., Price, J., Rizzo, G., Rosa-Neto, P., Schain, M., Scott, P.J., Searle, G., Slifstein, M., Suhara, T., Talbot, P.S., Thomas, A., Veronese, M., Wong, D.F., Yaqub, M., Zanderigo, F., Zoghbi, S., Innis, R.B., 2020. Guidelines for the content and format of PET brain data in publications and archives: A consensus paper. *J Cereb Blood Flow Metab* 40, 1576–1585. <https://doi.org/10.1177/0271678X20905433>
- Krause, D.L., Müller, N., 2010. Neuroinflammation, Microglia and Implications for Anti-Inflammatory Treatment in Alzheimer's Disease. *Int J Alzheimers Dis* 2010, 732806. <https://doi.org/10.4061/2010/732806>
- Lawley, D.N., 1938. A GENERALIZATION OF FISHER'S z TEST. *Biometrika* 30, 180–187. <https://doi.org/10.1093/biomet/30.1-2.180>
- Lema, A., Bishop, C., Malik, O., Mattoscio, M., Ali, R., Nicholas, R., Muraro, P.A., Matthews, P.M., Waldman, A.D., Newbould, R.D., 2017. A Comparison of Magnetization Transfer Methods to Assess Brain and Cervical Cord

- Microstructure in Multiple Sclerosis. *Journal of Neuroimaging* 27, 221–226.
<https://doi.org/10.1111/jon.12377>
- Li, Y., Sethi, S.K., Zhang, C., Miao, Y., Yerramsetty, K.K., Palutla, V.K., Gharabaghi, S., Wang, C., He, N., Cheng, J., Yan, F., Haacke, E.M., 2021. Iron Content in Deep Gray Matter as a Function of Age Using Quantitative Susceptibility Mapping: A Multicenter Study. *Frontiers in Neuroscience* 14.
- Liu, C.-C., Kanekiyo, T., Xu, H., Bu, G., 2013. Apolipoprotein E and Alzheimer disease: risk, mechanisms, and therapy. *Nat Rev Neurol* 9, 106–118.
<https://doi.org/10.1038/nrneurol.2012.263>
- Llanos-González, E., Henares-Chavarino, Á.A., Pedrero-Prieto, C.M., García-Carpintero, S., Frontiñán-Rubio, J., Sancho-Bielsa, F.J., Alcain, F.J., Peinado, J.R., Rabanal-Ruíz, Y., Durán-Prado, M., 2020. Interplay Between Mitochondrial Oxidative Disorders and Proteostasis in Alzheimer's Disease. *Frontiers in Neuroscience* 13.
- Lorio, S., Lutti, A., Kherif, F., Ruef, A., Dukart, J., Chowdhury, R., Frackowiak, R.S., Ashburner, J., Helms, G., Weiskopf, N., Draganski, B., 2014. Disentangling in vivo the effects of iron content and atrophy on the ageing human brain. *NeuroImage* 103, 280–289.
<https://doi.org/10.1016/j.neuroimage.2014.09.044>
- Lutti, A., Dick, F., Sereno, M.I., Weiskopf, N., 2014. Using high-resolution quantitative mapping of R1 as an index of cortical myelination. *NeuroImage, In-vivo Brodmann Mapping of the Human Brain* 93, 176–188.
<https://doi.org/10.1016/j.neuroimage.2013.06.005>
- Lutti, A., Hutton, C., Finsterbusch, J., Helms, G., Weiskopf, N., 2010. Optimization and validation of methods for mapping of the radiofrequency transmit field at 3T. *Magnetic Resonance in Medicine* 64, 229–238.
<https://doi.org/10.1002/mrm.22421>
- Mattis, S., 1988. *Dementia Rating Scale. Professional Manual.*
- Mawuenyega, K.G., Sigurdson, W., Ovod, V., Munsell, L., Kasten, T., Morris, J.C., Yarasheski, K.E., Bateman, R.J., 2010. Decreased Clearance of CNS β -Amyloid in Alzheimer's Disease. *Science* 330, 1774–1774.
<https://doi.org/10.1126/science.1197623>
- Mc Donald, J.M., Savva, G.M., Brayne, C., Welzel, A.T., Forster, G., Shankar, G.M., Selkoe, D.J., Ince, P.G., Walsh, D.M., 2010. The presence of sodium dodecyl sulphate-stable A β dimers is strongly associated with Alzheimer-type dementia. *Brain* 133, 1328–1341.
<https://doi.org/10.1093/brain/awq065>
- McFarquhar, M., McKie, S., Emsley, R., Suckling, J., Elliott, R., Williams, S., 2016. Multivariate and repeated measures (MRM): A new toolbox for dependent

- and multimodal group-level neuroimaging data. *NeuroImage* 132, 373–389. <https://doi.org/10.1016/j.neuroimage.2016.02.053>
- McKhann, G.M., Knopman, D.S., Chertkow, H., Hyman, B.T., Jack, C.R., Kawas, C.H., Klunk, W.E., Koroshetz, W.J., Manly, J.J., Mayeux, R., Mohs, R.C., Morris, J.C., Rossor, M.N., Scheltens, P., Carrillo, M.C., Thies, B., Weintraub, S., Phelps, C.H., 2011. The diagnosis of dementia due to Alzheimer’s disease: recommendations from the National Institute on Aging-Alzheimer’s Association workgroups on diagnostic guidelines for Alzheimer’s disease. *Alzheimers Dement* 7, 263–269. <https://doi.org/10.1016/j.jalz.2011.03.005>
- Mercier, J., Archen, L., Bollu, V., Carré, S., Evrard, Y., Jnoff, E., Kenda, B., Lallemand, B., Michel, P., Montel, F., Moureau, F., Price, N., Quesnel, Y., Sauvage, X., Valade, A., Provins, L., 2014. Discovery of Heterocyclic Nonacetamide Synaptic Vesicle Protein 2A (SV2A) Ligands with Single-Digit Nanomolar Potency: Opening Avenues towards the First SV2A Positron Emission Tomography (PET) Ligands. *ChemMedChem* 9, 693–698. <https://doi.org/10.1002/cmdc.201300482>
- Mercier, J., Provins, L., Valade, A., 2017. Discovery and development of SV2A PET tracers: Potential for imaging synaptic density and clinical applications. *Drug Discovery Today: Technologies, Imaging Technologies in Drug Discovery* 25, 45–52. <https://doi.org/10.1016/j.ddtec.2017.11.003>
- Moallemian, S., Bastin, C., Callaghan, M.F., Phillips, C., 2023a. Multivariate Age-related analysis of variance in quantitative MRI maps: Widespread age-related differences revisited. <https://doi.org/10.1101/2023.10.19.23297253>
- Moallemian, S., Salmon, E., Bahri, M.A., Beliy, N., Delhayé, E., Balteau, E., Degueldre, C., Phillips, C., Bastin, C., 2023b. Multimodal imaging of microstructural cerebral alterations and loss of synaptic density in Alzheimer’s disease. *Neurobiology of Aging* 132, 24–35. <https://doi.org/10.1016/j.neurobiolaging.2023.08.001>
- Mungas, D., Harvey, D., Reed, B.R., Jagust, W.J., DeCarli, C., Beckett, L., Mack, W.J., Kramer, J.H., Weiner, M.W., Schuff, N., Chui, H.C., 2005. Longitudinal volumetric MRI change and rate of cognitive decline. *Neurology* 65, 565–571. <https://doi.org/10.1212/01.wnl.0000172913.88973.0d>
- Munsch, F., Varma, G., Taso, M., Girard, O., Guidon, A., Duhamel, G., Alsop, D.C., 2021. Characterization of the cortical myeloarchitecture with inhomogeneous magnetization transfer imaging (ihMT). *NeuroImage* 225, 117442. <https://doi.org/10.1016/j.neuroimage.2020.117442>

- Murman, D.L., 2015. The Impact of Age on Cognition. *Semin Hear* 36, 111–121. <https://doi.org/10.1055/s-0035-1555115>
- Musiek, E.S., Holtzman, D.M., 2015. Three dimensions of the amyloid hypothesis: time, space and “wingmen.” *Nat Neurosci* 18, 800–806. <https://doi.org/10.1038/nn.4018>
- Namkung, H., Kim, S.-H., Sawa, A., 2017. The insula: an underestimated brain area in clinical neuroscience, psychiatry, and neurology. *Trends Neurosci* 40, 200–207. <https://doi.org/10.1016/j.tins.2017.02.002>
- Narbutas, J., Egroo, M.V., Chylinski, D., González, P.V., Jimenez, C.G., Besson, G., Ghaemmaghami, P., Hammad, G., Muto, V., Schmidt, C., Luxen, A., Salmon, E., Maquet, P., Bastin, C., Vandewalle, G., Collette, F., 2019. Cognitive efficiency in late midlife is linked to lifestyle characteristics and allostatic load. *Aging (Albany NY)* 11, 7169–7186. <https://doi.org/10.18632/aging.102243>
- Nasrabad, S.E., Rizvi, B., Goldman, J.E., Brickman, A.M., 2018. White matter changes in Alzheimer’s disease: a focus on myelin and oligodendrocytes. *Acta Neuropathol Commun* 6, 22. <https://doi.org/10.1186/s40478-018-0515-3>
- Naveh-Benjamin, M., Guez, J., Kilb, A., Reedy, S., 2004. The Associative Memory Deficit of Older Adults: Further Support Using Face-Name Associations. *Psychology and Aging* 19, 541–546. <https://doi.org/10.1037/0882-7974.19.3.541>
- Nimon, K.F., Oswald, F.L., 2013. Understanding the Results of Multiple Linear Regression: Beyond Standardized Regression Coefficients 16, 650–674. <https://doi.org/10.1177/1094428113493929>
- O’Brien, J.T., Firbank, M.J., Ritchie, K., Wells, K., Williams, G.B., Ritchie, C.W., Su, L., 2020. Association between midlife dementia risk factors and longitudinal brain atrophy: the PREVENT-Dementia study. *J Neurol Neurosurg Psychiatry* 91, 158–161. <https://doi.org/10.1136/jnnp-2019-321652>
- Papp, K.V., Rentz, D.M., Orlovsky, I., Sperling, R.A., Mormino, E.C., 2017. Optimizing the preclinical Alzheimer’s cognitive composite with semantic processing: The PACC5. *Alzheimer’s & Dementia: Translational Research & Clinical Interventions* 3, 668–677. <https://doi.org/10.1016/j.trci.2017.10.004>
- Pardo, J.V., Lee, J.T., Sheikh, S.A., Surerus-Johnson, C., Shah, H., Munch, K.R., Carlis, J.V., Lewis, S.M., Kuskowski, M.A., Dysken, M.W., 2007. Where the Brain Grows Old: Decline in Anterior Cingulate and Medial Prefrontal Function with Normal Aging. *Neuroimage* 35, 1231–1237. <https://doi.org/10.1016/j.neuroimage.2006.12.044>

- Patterson, J., 2011. F-A-S Test, in: Kreutzer, J.S., DeLuca, J., Caplan, B. (Eds.), *Encyclopedia of Clinical Neuropsychology*. Springer, New York, NY, pp. 1024–1026. https://doi.org/10.1007/978-0-387-79948-3_886
- Peng, Y., Chang, X., Lang, M., 2021. Iron Homeostasis Disorder and Alzheimer’s Disease. *Int J Mol Sci* 22, 12442. <https://doi.org/10.3390/ijms222212442>
- Perl, D.P., 2010. Neuropathology of Alzheimer’s Disease. *Mt Sinai J Med* 77, 32–42. <https://doi.org/10.1002/msj.20157>
- Peters, A., 2002. The effects of normal aging on myelin and nerve fibers: A review. *Journal of Neurocytology* 31, 581–593. <https://doi.org/10.1023/a:1025731309829>
- Peters, A., Moss, M.B., Sethares, C., 2000. Effects of aging on myelinated nerve fibers in monkey primary visual cortex. *Journal of Comparative Neurology* 419, 364–376. [https://doi.org/10.1002/\(SICI\)1096-9861\(20000410\)419:3<364::AID-CNE8>3.0.CO;2-R](https://doi.org/10.1002/(SICI)1096-9861(20000410)419:3<364::AID-CNE8>3.0.CO;2-R)
- Peters, A., Sethares, C., 2002. Aging and the myelinated fibers in prefrontal cortex and corpus callosum of the monkey. *Journal of Comparative Neurology* 442, 277–291. <https://doi.org/10.1002/cne.10099>
- Pillai, K.C.S., 1955. Some New Test Criteria in Multivariate Analysis. *The Annals of Mathematical Statistics* 26, 117–121. <https://doi.org/10.1214/aoms/1177728599>
- Pini, L., Pievani, M., Bocchetta, M., Altomare, D., Bosco, P., Cavado, E., Galluzzi, S., Marizzoni, M., Frisoni, G.B., 2016. Brain atrophy in Alzheimer’s Disease and aging. *Ageing Research Reviews, Brain Imaging and Aging* 30, 25–48. <https://doi.org/10.1016/j.arr.2016.01.002>
- Pîrșcoveanu, D.F.V., Pirici, I., Tudorică, V., Bălșeanu, T.A., Albu, V.C., Bondari, S., Bumbea, A.M., Pîrșcoveanu, M., 2017. Tau protein in neurodegenerative diseases - a review. *Rom J Morphol Embryol* 58, 1141–1150.
- Preibisch, C., Deichmann, R., 2009. Influence of RF spoiling on the stability and accuracy of T1 mapping based on spoiled FLASH with varying flip angles. *Magnetic Resonance in Medicine* 61, 125–135. <https://doi.org/10.1002/mrm.21776>
- Rajah, M.N., Languay, R., Grady, C.L., 2011. Age-Related Changes in Right Middle Frontal Gyrus Volume Correlate with Altered Episodic Retrieval Activity. *J Neurosci* 31, 17941–17954. <https://doi.org/10.1523/JNEUROSCI.1690-11.2011>
- Ramanoël, S., Hoyau, E., Kauffmann, L., Renard, F., Pichat, C., Boudiaf, N., Krainik, A., Jaillard, A., Baciou, M., 2018. Gray Matter Volume and Cognitive Performance During Normal Aging. A Voxel-Based Morphometry Study. *Front Aging Neurosci* 10, 235. <https://doi.org/10.3389/fnagi.2018.00235>

- Reitz, C., Mayeux, R., 2014. Alzheimer disease: Epidemiology, diagnostic criteria, risk factors and biomarkers. *Biochemical Pharmacology* 88, 640–651. <https://doi.org/10.1016/j.bcp.2013.12.024>
- Resnick, S.M., Lamar, M., Driscoll, I., 2007. Vulnerability of the orbitofrontal cortex to age-associated structural and functional brain changes. *Ann N Y Acad Sci* 1121, 562–575. <https://doi.org/10.1196/annals.1401.027>
- Rolls, E.T., 2019. The cingulate cortex and limbic systems for emotion, action, and memory. *Brain Struct Funct* 224, 3001–3018. <https://doi.org/10.1007/s00429-019-01945-2>
- Rolls, E.T., 2004. The functions of the orbitofrontal cortex. *Brain and Cognition, Development of Orbitofrontal Function* 55, 11–29. [https://doi.org/10.1016/S0278-2626\(03\)00277-X](https://doi.org/10.1016/S0278-2626(03)00277-X)
- Rolls, E.T., Huang, C.-C., Lin, C.-P., Feng, J., Joliot, M., 2020. Automated anatomical labelling atlas 3. *NeuroImage* 206, 116189. <https://doi.org/10.1016/j.neuroimage.2019.116189>
- Roy, S.N., 1945. The Individual Sampling Distribution of the Maximum, the Minimum and Any Intermediate of the p-Statistics on the Null-Hypothesis on JSTOR. *The Indian Journal of Statistics (1933-1960)* 7, 133–158.
- Rugg, M.D., Vilberg, K.L., 2013. Brain Networks Underlying Episodic Memory Retrieval. *Curr Opin Neurobiol* 23, 255–260. <https://doi.org/10.1016/j.conb.2012.11.005>
- Salthouse, T.A., Babcock, R.L., Shaw, R.J., 1991. Effects of adult age on structural and operational capacities in working memory. *Psychology and Aging* 6, 118–127. <https://doi.org/10.1037/0882-7974.6.1.118>
- Scheff, S.W., Neltner, J.H., Nelson, P.T., 2014. Is synaptic loss a unique hallmark of Alzheimer’s disease? *Biochemical Pharmacology, Alzheimer’s Disease – Amyloid, Tau and Beyond* 88, 517–528. <https://doi.org/10.1016/j.bcp.2013.12.028>
- Scheff, S.W., Price, D.A., Schmitt, F.A., Mufson, E.J., 2006. Hippocampal synaptic loss in early Alzheimer’s disease and mild cognitive impairment. *Neurobiology of Aging* 27, 1372–1384. <https://doi.org/10.1016/j.neurobiolaging.2005.09.012>
- Schöll, M., Lockhart, S.N., Schonhaut, D.R., O’Neil, J.P., Janabi, M., Ossenkuppele, R., Baker, S.L., Vogel, J.W., Faria, J., Schwimmer, H.D., Rabinovici, G.D., Jagust, W.J., 2016. PET Imaging of Tau Deposition in the Aging Human Brain. *Neuron* 89, 971–982. <https://doi.org/10.1016/j.neuron.2016.01.028>
- Selkoe, D.J., 2002. Alzheimer’s Disease Is a Synaptic Failure. *Science* 298, 789–791. <https://doi.org/10.1126/science.1074069>

- Sigalovsky, I.S., Fischl, B., Melcher, J.R., 2006. Mapping an intrinsic MR property of gray matter in auditory cortex of living humans: A possible marker for primary cortex and hemispheric differences. *NeuroImage* 32, 1524–1537. <https://doi.org/10.1016/j.neuroimage.2006.05.023>
- Sintini, I., Schwarz, C.G., Martin, P.R., Graff-Radford, J., Machulda, M.M., Senjem, M.L., Reid, R.I., Spychalla, A.J., Drubach, D.A., Lowe, V.J., Jack, C.R., Josephs, K.A., Whitwell, J.L., 2018. Regional multimodal relationships between tau, hypometabolism, atrophy, and fractional anisotropy in atypical Alzheimer’s disease. *Hum Brain Mapp* hbm.24473. <https://doi.org/10.1002/hbm.24473>
- Snaidero, N., Simons, M., 2014. Myelination at a glance. *J Cell Sci* 127, 2999–3004. <https://doi.org/10.1242/jcs.151043>
- Soria Lopez, J.A., González, H.M., Léger, G.C., 2019. Chapter 13 - Alzheimer’s disease, in: Dekosky, S.T., Asthana, S. (Eds.), *Handbook of Clinical Neurology, Geriatric Neurology*. Elsevier, pp. 231–255. <https://doi.org/10.1016/B978-0-12-804766-8.00013-3>
- Sperling, R.A., Aisen, P.S., Beckett, L.A., Bennett, D.A., Craft, S., Fagan, A.M., Iwatsubo, T., Jack, C.R., Kaye, J., Montine, T.J., Park, D.C., Reiman, E.M., Rowe, C.C., Siemers, E., Stern, Y., Yaffe, K., Carrillo, M.C., Thies, B., Morrison-Bogorad, M., Wagster, M.V., Phelps, C.H., 2011a. Toward defining the preclinical stages of Alzheimer’s disease: Recommendations from the National Institute on Aging-Alzheimer’s Association workgroups on diagnostic guidelines for Alzheimer’s disease. *Alzheimers Dement* 7, 280–292. <https://doi.org/10.1016/j.jalz.2011.03.003>
- Sperling, R.A., Jack, C.R., Aisen, P.S., 2011b. Testing the Right Target and Right Drug at the Right Stage. *Science Translational Medicine* 3, 111cm33–111cm33. <https://doi.org/10.1126/scitranslmed.3002609>
- Sperling, R.A., Rentz, D.M., Johnson, K.A., Karlawish, J., Donohue, M., Salmon, D.P., Aisen, P., 2014. The A4 Study: Stopping AD Before Symptoms Begin? *Sci. Transl. Med.* 6. <https://doi.org/10.1126/scitranslmed.3007941>
- Spillantini, M.G., Goedert, M., 2013. Tau pathology and neurodegeneration. *The Lancet Neurology* 12, 609–622. [https://doi.org/10.1016/S1474-4422\(13\)70090-5](https://doi.org/10.1016/S1474-4422(13)70090-5)
- Sprinz, C., Altmayer, S., Zanon, M., Watte, G., Irion, K., Marchiori, E., Hochegger, B., 2018. Effects of blood glucose level on 18F-FDG uptake for PET/CT in normal organs: A systematic review. *PLoS One* 13, e0193140. <https://doi.org/10.1371/journal.pone.0193140>

- St Clair-Thompson, H.L., 2010. Backwards digit recall: A measure of short-term memory or working memory? *European Journal of Cognitive Psychology* 22, 286–296. <https://doi.org/10.1080/09541440902771299>
- Stanisz, G. j., Kecojevic, A., Bronskill, M. j., Henkelman, R. m., 1999. Characterizing white matter with magnetization transfer and T2. *Magnetic Resonance in Medicine* 42, 1128–1136. [https://doi.org/10.1002/\(SICI\)1522-2594\(199912\)42:6<1128::AID-MRM18>3.0.CO;2-9](https://doi.org/10.1002/(SICI)1522-2594(199912)42:6<1128::AID-MRM18>3.0.CO;2-9)
- Stark, S.M., Kirwan, C.B., Stark, C.E.L., 2019. Mnemonic Similarity Task: A Tool for Assessing Hippocampal Integrity. *Trends Cogn Sci* 23, 938–951. <https://doi.org/10.1016/j.tics.2019.08.003>
- Steiger, T.K., Weiskopf, N., Bunzeck, N., 2016. Iron Level and Myelin Content in the Ventral Striatum Predict Memory Performance in the Aging Brain. *Journal of Neuroscience* 36, 3552–3558. <https://doi.org/10.1523/JNEUROSCI.3617-15.2016>
- Stroop, J.R., 1935. Studies of interference in serial verbal reactions. *Journal of Experimental Psychology* 18, 643–662. <https://doi.org/10.1037/h0054651>
- Stüber, C., Morawski, M., Schäfer, A., Labadie, C., Wähnert, M., Leuze, C., Streicher, M., Barapatre, N., Reimann, K., Geyer, S., Spemann, D., Turner, R., 2014. Myelin and iron concentration in the human brain: A quantitative study of MRI contrast. *NeuroImage* 93, 95–106. <https://doi.org/10.1016/j.neuroimage.2014.02.026>
- Su, L., M. Blamire, A., Watson, R., He, J., Aribisala, B., T. O128;™Brien, J., 2016. Cortical and Subcortical Changes in Alzheimer’s Disease: A Longitudinal and Quantitative MRI Study. *Current Alzheimer Research* 13, 534–544.
- Tabachnick, B.G., Fidell, L.S., 2007. Using multivariate statistics, 5th ed. ed. Pearson/Allyn & Bacon, Boston.
- Tabelow, K., Balteau, E., Ashburner, J., Callaghan, M.F., Draganski, B., Helms, G., Kherif, F., Leutritz, T., Lutti, A., Phillips, C., Reimer, E., Ruthotto, L., Seif, M., Weiskopf, N., Ziegler, G., Mohammadi, S., 2019. hMRI – A toolbox for quantitative MRI in neuroscience and clinical research. *NeuroImage* 194, 191–210. <https://doi.org/10.1016/j.neuroimage.2019.01.029>
- Tan, C.-C., Yu, J.-T., Tan, L., 2014. Biomarkers for Preclinical Alzheimer’s Disease. *JAD* 42, 1051–1069. <https://doi.org/10.3233/JAD-140843>
- Tanzi, R.E., 2012. The genetics of Alzheimer disease. *Cold Spring Harb Perspect Med* 2, a006296. <https://doi.org/10.1101/cshperspect.a006296>
- Tatulian, S.A., 2022. Challenges and hopes for Alzheimer’s disease. *Drug Discovery Today* 27, 1027–1043. <https://doi.org/10.1016/j.drudis.2022.01.016>

- Taubert, M., Roggenhofer, E., Melie-Garcia, L., Muller, S., Lehmann, N., Preisig, M., Vollenweider, P., Marques-Vidal, P., Lutti, A., Kherif, F., Draganski, B., 2020. Converging patterns of aging-associated brain volume loss and tissue microstructure differences. *Neurobiology of Aging* 88, 108–118. <https://doi.org/10.1016/j.neurobiolaging.2020.01.006>
- Terry, R.D., Masliah, E., Salmon, D.P., Butters, N., DeTeresa, R., Hill, R., Hansen, L.A., Katzman, R., 1991. Physical basis of cognitive alterations in alzheimer's disease: Synapse loss is the major correlate of cognitive impairment. *Ann Neurol* 30, 572–580. <https://doi.org/10.1002/ana.410300410>
- Thomas, B.A., Cuplov, V., Bousse, A., Mendes, A., Thielemans, K., Hutton, B.F., Erlandsson, K., 2016. PETPVC: a toolbox for performing partial volume correction techniques in positron emission tomography. *Phys. Med. Biol.* 61, 7975–7993. <https://doi.org/10.1088/0031-9155/61/22/7975>
- Tian, Yao, Tian, Yuanliangzi, Yuan, Z., Zeng, Y., Wang, S., Fan, X., Yang, D., Yang, M., 2022. Iron Metabolism in Aging and Age-Related Diseases. *Int J Mol Sci* 23, 3612. <https://doi.org/10.3390/ijms23073612>
- Timmler, S., Simons, M., 2019. Grey matter myelination. *Glia* 67, 2063–2070. <https://doi.org/10.1002/glia.23614>
- Troyer, A.K., Moscovitch, M., Winocur, G., 1997. Clustering and switching as two components of verbal fluency: Evidence from younger and older healthy adults. *Neuropsychology* 11, 138–146. <https://doi.org/10.1037/0894-4105.11.1.138>
- Tzioras, M., McGeachan, R.I., Durrant, C.S., Spires-Jones, T.L., 2023. Synaptic degeneration in Alzheimer disease. *Nat Rev Neurol* 19, 19–38. <https://doi.org/10.1038/s41582-022-00749-z>
- Upright, N.A., Baxter, M.G., 2021. Prefrontal cortex and cognitive aging in macaque monkeys. *American Journal of Primatology* 83, e23250. <https://doi.org/10.1002/ajp.23250>
- van Bergen, J.M.G., Li, X., Hua, J., Schreiner, S.J., Steininger, S.C., Quevenco, F.C., Wyss, M., Gietl, A.F., Treyer, V., Leh, S.E., Buck, F., Nitsch, R.M., Pruessmann, K.P., van Zijl, P.C.M., Hock, C., Unschuld, P.G., 2016. Colocalization of cerebral iron with Amyloid beta in Mild Cognitive Impairment. *Sci Rep* 6, 35514. <https://doi.org/10.1038/srep35514>
- Van Duijn, S., Bulk, M., Van Duinen, S.G., Nabuurs, R.J.A., Van Buchem, M.A., Van Der Weerd, L., Natté, R., 2017. Cortical Iron Reflects Severity of Alzheimer's Disease. *JAD* 60, 1533–1545. <https://doi.org/10.3233/JAD-161143>
- Van Egroo, M., Narbutas, J., Chylinski, D., Villar González, P., Ghaemmaghami, P., Muto, V., Schmidt, C., Gaggioni, G., Besson, G., Pépin, X., Tezel, E.,

- Marzoli, D., Le Goff, C., Cavalier, E., Luxen, A., Salmon, E., Maquet, P., Bahri, M.A., Phillips, C., Bastin, C., Collette, F., Vandewalle, G., 2019. Preserved wake-dependent cortical excitability dynamics predict cognitive fitness beyond age-related brain alterations. *Commun Biol* 2, 449. <https://doi.org/10.1038/s42003-019-0693-y>
- Varma, G., Munsch, F., Burns, B., Duhamel, G., Girard, O.M., Guidon, A., Lebel, R.M., Alsop, D.C., 2020. Three-dimensional inhomogeneous magnetization transfer with rapid gradient-echo (3D ihMTRAGE) imaging. *Magnetic Resonance in Medicine* 84, 2964–2980. <https://doi.org/10.1002/mrm.28324>
- Villain, N., Fouquet, M., Baron, J.-C., Mézange, F., Landeau, B., De La Sayette, V., Viader, F., Eustache, F., Desgranges, B., Chételat, G., 2010. Sequential relationships between grey matter and white matter atrophy and brain metabolic abnormalities in early Alzheimer’s disease. *Brain* 133, 3301–3314. <https://doi.org/10.1093/brain/awq203>
- Villemagne, V.L., Pike, K.E., Chételat, G., Ellis, K.A., Mulligan, R.S., Bourgeat, P., Ackermann, U., Jones, G., Szoek, C., Salvado, O., Martins, R., O’Keefe, G., Mathis, C.A., Klunk, W.E., Ames, D., Masters, C.L., Rowe, C.C., 2011. Longitudinal assessment of A β and cognition in aging and Alzheimer disease. *Annals of Neurology* 69, 181–192. <https://doi.org/10.1002/ana.22248>
- Wang, F., Ren, S.-Y., Chen, J.-F., Liu, K., Li, R.-X., Li, Z.-F., Hu, B., Niu, J.-Q., Xiao, L., Chan, J.R., Mei, F., 2020. Myelin degeneration and diminished myelin renewal contribute to age-related deficits in memory. *Nat Neurosci* 23, 481–486. <https://doi.org/10.1038/s41593-020-0588-8>
- Wang, S.-S., Zhang, Z., Zhu, T.-B., Chu, S.-F., He, W.-B., Chen, N.-H., 2018. Myelin injury in the central nervous system and Alzheimer’s disease. *Brain Research Bulletin* 140, 162–168. <https://doi.org/10.1016/j.brainresbull.2018.05.003>
- Warnock, G.I., Aerts, J., Bahri, M.A., Bretin, F., Lemaire, C., Giacomelli, F., Mievis, F., Mestdagh, N., Buchanan, T., Valade, A., Mercier, J., Wood, M., Gillard, M., Seret, A., Luxen, A., Salmon, E., Plenevaux, A., 2014. Evaluation of 18F-UCB-H as a Novel PET Tracer for Synaptic Vesicle Protein 2A in the Brain. *Journal of Nuclear Medicine* 55, 1336–1341. <https://doi.org/10.2967/jnumed.113.136143>
- Wechsler, D., 1997. Wechsler Adult Intelligence Scale, 3rd ed. The Psychological Corporation, San Antonio.
- Weiskopf, N., Callaghan, M.F., Josephs, O., Lutti, A., Mohammadi, S., 2014. Estimating the apparent transverse relaxation time (R2*) from images with

- different contrasts (ESTATICS) reduces motion artifacts. *Front Neurosci* 8:278, 1–10. <https://doi.org/10.3389/fnins.2014.00278>
- Weiskopf, N., Edwards, L.J., Helms, G., Mohammadi, S., Kirilina, E., 2021. Quantitative magnetic resonance imaging of brain anatomy and in vivo histology. *Nat Rev Phys* 3, 570–588. <https://doi.org/10.1038/s42254-021-00326-1>
- Weiskopf, N., Lutti, A., Helms, G., Novak, M., Ashburner, J., Hutton, C., 2011. Unified segmentation based correction of R1 brain maps for RF transmit field inhomogeneities (UNICORT). *NeuroImage* 54, 2116–2124. <https://doi.org/10.1016/j.neuroimage.2010.10.023>
- Weiskopf, N., Mohammadi, S., Lutti, A., Callaghan, M.F., 2015. Advances in MRI-based computational neuroanatomy: from morphometry to in-vivo histology. *Current Opinion in Neurology* 28, 313. <https://doi.org/10.1097/WCO.0000000000000222>
- Weiskopf, N., Suckling, J., Williams, G., Correia, M.M., Inkster, B., Tait, R., Ooi, C., Bullmore, E.T., Lutti, A., 2013. Quantitative multi-parameter mapping of R1, PD*, MT, and R2* at 3T: a multi-center validation. *Front. Neurosci.* 7:95, 1–11. <https://doi.org/10.3389/fnins.2013.00095>
- Weller, R.O., Djuanda, E., Yow, H.-Y., Carare, R.O., 2009. Lymphatic drainage of the brain and the pathophysiology of neurological disease. *Acta Neuropathol* 117, 1–14. <https://doi.org/10.1007/s00401-008-0457-0>
- Whitwell, J.L., Graff-Radford, J., Tosakulwong, N., Weigand, S.D., Machulda, M., Senjem, M.L., Spychalla, A.J., Vemuri, P., Jones, D.T., Drubach, D.A., Knopman, D.S., Boeve, B.F., Ertekin-Taner, N., Petersen, R.C., Lowe, V.J., Jack, C.R., Josephs, K.A., 2018. Imaging correlations of tau, amyloid, metabolism and atrophy in typical & atypical AD. *Alzheimers Dement* 14, 1005–1014. <https://doi.org/10.1016/j.jalz.2018.02.020>
- Whitwell, J.L., Josephs, K.A., Murray, M.E., Kantarci, K., Przybelski, S.A., Weigand, S.D., Vemuri, P., Senjem, M.L., Parisi, J.E., Knopman, D.S., Boeve, B.F., Petersen, R.C., Dickson, D.W., Jack, C.R., 2008. MRI correlates of neurofibrillary tangle pathology at autopsy: A voxel-based morphometry study. *Neurology* 71, 743–749. <https://doi.org/10.1212/01.wnl.0000324924.91351.7d>
- Wilks, S.S., 1932. Certain Generalizations in the Analysis of Variance. *Biometrika* 24, 471–494. <https://doi.org/10.2307/2331979>
- Wimo, A., Ali, G.-C., Guerchet, M., Prince, M., Prina, M., Wu, Y.-T., 2015. World Alzheimer Report 2015: The global impact of dementia: An analysis of prevalence, incidence, cost and trends. *Alzheimer's Disease International*.

- Winkler, A.M., Ridgway, G.R., Webster, M.A., Smith, S.M., Nichols, T.E., 2014. Permutation inference for the general linear model. *NeuroImage* 92, 381–397. <https://doi.org/10.1016/j.neuroimage.2014.01.060>
- Winkler, A.M., Webster, M.A., Brooks, J.C., Tracey, I., Smith, S.M., Nichols, T.E., 2016. Non-parametric combination and related permutation tests for neuroimaging. *Human Brain Mapping* 37, 1486–1511. <https://doi.org/10.1002/hbm.23115>
- Wirth, M., Bejanin, A., La Joie, R., Arenaza-Urquijo, E.M., Gonneaud, J., Landeau, B., Perrotin, A., Mézence, F., de La Sayette, V., Desgranges, B., Chételat, G., 2018. Regional patterns of gray matter volume, hypometabolism, and beta-amyloid in groups at risk of Alzheimer’s disease. *Neurobiology of Aging* 63, 140–151. <https://doi.org/10.1016/j.neurobiolaging.2017.10.023>
- Wyss-Coray, T., 2016. Ageing, neurodegeneration and brain rejuvenation. *Nature* 539, 180–186. <https://doi.org/10.1038/nature20411>
- Xiaomin, Y., Chenhao, Z., Zheng, Z., Yanyan, Q., Junze, B., Wie, Q., 2021. The Role of Amyloid-Beta and Tau in the Early Pathogenesis of Alzheimer’s Disease. *Med Sci Monit* 27, e933084-1-e933084-7. <https://doi.org/10.12659/MSM.933084>
- Yang, Y., Wang, D., Hou, W., Li, H., 2023. Cognitive Decline Associated with Aging, in: Zhang, Z. (Ed.), *Cognitive Aging and Brain Health, Advances in Experimental Medicine and Biology*. Springer Nature, Singapore, pp. 25–46. https://doi.org/10.1007/978-981-99-1627-6_3
- Yin, X., W Qian, Y Qiu, C Zhao, Z Zhou, J Bao, 2021. The Role of Amyloid-Beta and Tau in the Early Pathogenesis of Alzheimer’s Disease. *Med. Sci. Monit. Int. Med. J. Exp. Clin. Res.*
- Yoon, S., Baik, B., Park, T., Nam, D., 2021. Powerful p-value combination methods to detect incomplete association. *Sci Rep* 11, 6980. <https://doi.org/10.1038/s41598-021-86465-y>
- Young, P.N.E., Estarellas, M., Coomans, E., Srikrishna, M., Beaumont, H., Maass, A., Venkataraman, A.V., Lissaman, R., Jiménez, D., Betts, M.J., McGlinchey, E., Berron, D., O’Connor, A., Fox, N.C., Pereira, J.B., Jagust, W., Carter, S.F., Paterson, R.W., Schöll, M., 2020. Imaging biomarkers in neurodegeneration: current and future practices. *Alz Res Therapy* 12, 49. <https://doi.org/10.1186/s13195-020-00612-7>
- Zarow, C., Vinters, H.V., Ellis, W.G., Weiner, M.W., Mungas, D., White, L., Chui, H.C., 2005. Correlates of Hippocampal Neuron Number in Alzheimer’s Disease and Ischemic Vascular Dementia. *Ann Neurol* 57, 896–903. <https://doi.org/10.1002/ana.20503>

- Zecca, L., Youdim, M.B.H., Riederer, P., Connor, J.R., Crichton, R.R., 2004. Iron, brain ageing and neurodegenerative disorders. *Nat Rev Neurosci* 5, 863–873. <https://doi.org/10.1038/nrn1537>
- Zeineh, M.M., Chen, Y., Kitzler, H.H., Hammond, R., Vogel, H., Rutt, B.K., 2015. Activated iron-containing microglia in the human hippocampus identified by magnetic resonance imaging in Alzheimer disease. *Neurobiology of Aging* 36, 2483–2500. <https://doi.org/10.1016/j.neurobiolaging.2015.05.022>
- Zhang, H., Schneider, T., Wheeler-Kingshott, C.A., Alexander, D.C., 2012. NODDI: Practical in vivo neurite orientation dispersion and density imaging of the human brain. *NeuroImage* 61, 1000–1016. <https://doi.org/10.1016/j.neuroimage.2012.03.072>
- Zhong, S., Lou, J., Ma, K., Shu, Z., Chen, L., Li, C., Ye, Q., Zhou, L., Shen, Y., Ye, X., Zhang, J., 2023. Disentangling in-vivo microstructural changes of white and gray matter in mild cognitive impairment and Alzheimer’s disease: a systematic review and meta-analysis. *Brain Imaging and Behavior*. <https://doi.org/10.1007/s11682-023-00805-2>
- Zimmermann, P., Fimm, B., 1994. Test d’Évaluation de l’Attention (TEA). Version 1.02. Psychologisches Institut der Universität Freiburg, Freiburg.